Chem Soc Rev

REVIEW ARTICLE

View Article Online
View Journal | View Issue

Cite this: *Chem. Soc. Rev.*, 2014, 43, 7746

Oxygen electrocatalysts in metal–air batteries: from aqueous to nonaqueous electrolytes

Zhong-Li Wang, Dan Xu, Ji-Jing Xu and Xin-Bo Zhang*

With the development of renewable energy and electrified transportation, electrochemical energy storage will be more important in the future than it has ever been in the past. Although lithium-ion batteries (LIBs) are traditionally considered to be the most likeliest candidate thanks to their relatively long cycle life and high energy efficiency, their limited energy density as well as cost are still causing a bottleneck for their long-term application. Alternatively, metal–air batteries have been proposed as a very promising large-scale electricity storage technology with the replacement of the intercalation reaction mechanism by the catalytic redox reaction of a light weight metal–oxygen couple. Generally, based on the electrolyte, these metal–air batteries can be divided into aqueous and nonaqueous systems, corresponding to two typical batteries of Zn–air and Li–air, respectively. The prominent feature of both batteries are their extremely high theoretical energy density, especially for nonaqueous Li–air batteries, which far exceeds the best that can be achieved with LIBs. In this review, we focus on the major obstacle of sluggish kinetics of the cathode in both batteries, and summarize the fundamentals and recent advances related to the oxygen catalyst materials. According to the electrolyte, the aqueous and nonaqueous electrocatalytic mechanisms of the oxygen reduction and evolution reactions are discussed. Subsequently, seven groups of oxygen catalysts, which have played catalytic roles in both systems, are selectively reviewed, including transition metal oxides (single-metal oxides and mixed-metal oxides), functional carbon materials (nanostructured carbons and doped carbons), metal oxide–nanocarbon hybrid materials, metal–nitrogen complexes (non-pyrolyzed and pyrolyzed), transition metal nitrides, conductive polymers, and precious metals (alloys). Nonaqueous systems have the advantages of energy density and rechargeability over aqueous systems and have gradually become the research focus of metal–air batteries. However, there are considerable challenges beyond catalysts from aqueous to nonaqueous electrolytes, which are also discussed in this review. Finally, several future research directions are proposed based on the results achieved in this field, with emphasis on nonaqueous Li–air batteries.

Received 10th July 2013

DOI: 10.1039/c3cs60248f

www.rsc.org/csr

1 Introduction

Energy and the environment are among the most important issues of the twenty-first century. The global demand for energy has been increasing rapidly and continuously.[1–3] It is projected that the primary energy demand will easily double within the next 15 years.[4] However, until now a significant portion (over 80%) of the total energy supply comes from fossil fuels, such as coal, oil, and natural gas, causing a dramatic build-up of greenhouse gases in the atmosphere, and even more seriously, it is unsustainable there are finite reserves.[5] In response, energy conversion from renewable sources has been considered as a promising solution to significantly reduce the dependence on fossil fuels that cause large amount of carbon dioxide. However, the so-called renewable and "green" electricity generated from natural sources, such as solar or wind, is intrinsically fluctuant and intermittent because of the variety of weather conditions, which thus essentially requires large-scale energy storage devices to counterbalance its variability.[6] Among the various electrical storage technologies, secondary electrochemical batteries are one of the most efficient, simplest and reliable systems, which could convert electrical energy directly into chemical energy or *vice versa* by reversible electrochemical oxidation–reduction reactions.[7]

Rechargeable lithium-ion batteries are traditionally considered as the most promising storage technology due to their relatively long-cycling life (>5000 cycles) and high-energy efficiency (>90%). On charging, lithium ions are deintercalated from the layered $LiCoO_2$ intercalation host, passed across the electrolyte, and are intercalated between the graphite layers in the anode. Discharge reverses this process. There is little side reactions occurring during the charge–discharge process. However, the insufficient energy density of lithium ion batteries (theoretical value is

State Key Laboratory of Rare Earth Resource Utilization, Changchun Institute of Applied Chemistry, Chinese Academy of Sciences, Changchun, 130022, P. R. China. E-mail: xbzhang@ciac.ac.cn

$\sim$400 W h kg^{-1}) limits their long-term applications.[8–10] Moreover, even with optimization of this technology, using currently available materials, it is still hard to meet the high energy demands of large-scale electricity storage for renewable energy and electric automotive vehicles.[11] The conventional intercalation reaction mechanism almost limits the energy density of LIBs. In this context, the exploitation of high-energy density storage technologies is urgently required. Fortunately, an alternative approach in battery technology, is the replacement of the intercalation material at the cathode with a catalytically active oxygen reduction reaction (ORR) and an oxygen evolution reaction (OER) electrode. These batteries, named as metal–air batteries, such as Zn–air batteries and Li–air batteries, have attracted much attention due to their extremely high energy density, low cost, and environmentally friendly operation. Metal–air batteries generate electricity through a redox reaction between the metal and the oxygen in air. They are featured with an open cell structure, which admits the supply of the cathode active material (oxygen) continuously and almost infinitely from an external source (air). Due to the fact that the cathode oxygen is from air and not stored in the cell, the metal–air family has a notably higher theoretical energy density, compared with other traditional batteries such as the primary Zn–MnO_2 (Zn–Mn), rechargeable lead-acid, nickel–metal hydride (Ni–MH) and LIBs.[12] Among metal–air batteries, Zn–air batteries have been studied for many years and the theoretical specific energy density of Zn–air batteries can reach 1084 W h kg^{-1}.[13] They have many advantages such as a flat discharge voltage plateau, high safety, low cost, and long shelf life.[14–16] Recently, many efforts have been devoted to Li–air battery research. Due to the nonaqueous reaction mechanism and the lightest metal element of lithium, its theoretical energy density is approximately 11 680 W h kg^{-1}, nearly equivalent to gasoline.[17] Undoubtedly, Li–air batteries are potential next-generation energy storage devices.

Zhong-Li Wang

Dr Zhongli Wang received his Bachelor's degree in chemistry from Qingdao University of Science & Technology in 2005. He then became a graduate student in Professor Jian Meng's group at the Changchun Institute of Applied Chemistry (CIAC), Chinese Academy of Sciences (CAS), and received a PhD degree in 2010. After graduation, he joined the group of Professor Xin-Bo Zhang at CIAC. He is now working as an associate professor under the direction of Prof. Zhang at CIAC. His current research interests are advanced carbon and inorganic nanomaterials for electrochemical energy storage and conversion.

Dan Xu

Dr Dan Xu received her BS and PhD degrees in applied chemistry from Jilin University, China, in 2005 and 2010, respectively. She then went to the Changchun Institute of Applied Chemistry (CIAC), Chinese Academy of Sciences (CAS) working as a postdoctor from 2011–2013. As of 2013, she is working as an assistant professor under the direction of Prof. Xin-Bo Zhang at CIAC, CAS. Her current research interests include the characterization of electrolytes and catalysts as well as the mechanism analysis of Li–O_2 batteries via in situ methods.

Ji-Jing Xu

Dr Jijing Xu received his BS and PhD degrees in applied chemistry from Jilin University, China, in 2006 and 2011, respectively. He then went to the Changchun Institute of Applied Chemistry (CIAC), Chinese Academy of Sciences (CAS), working as a postdoctor from 2011–2013. As of 2013, he is working as an assistant professor under the direction of Prof. Xin-Bo Zhang at CIAC, CAS. His current research interests include the synthesis and characterization of efficient energy storage materials and their application in lithium–air batteries.

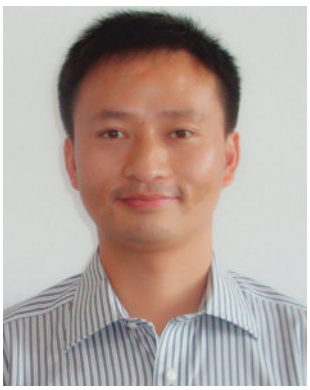

Xin-Bo Zhang

Dr Xinbo Zhang (1978) joined the Changchun Institute of Applied Chemistry (CIAC) as a professor of "Hundred Talents Program" of Chinese Academy of Sciences (CAS) in the spring of 2010. He received his PhD degree in inorganic chemistry from CIAC and was granted the CAS Presidential Scholarship Award in 2005. From 2005–2010 he worked as a JSPS and NEDO fellow at the National Institute of Advanced Industrial Science and Technology (Kansai Center), Japan. His interests mainly focus on functional inorganic materials for energy storage & conversion with fuel cells and batteries, especially lithium–air batteries.

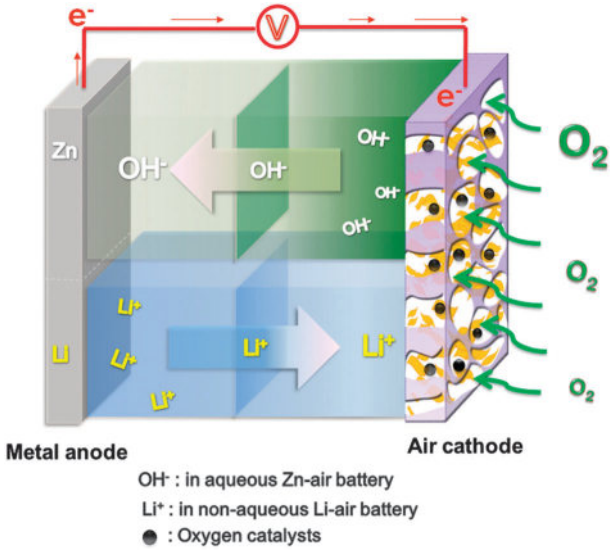

Fig. 1 Schematic structure of a metal–air battery (aqueous Zn–air and nonaqueous Li–air) composed of a metal as the anode and a porous air electrode as the cathode.

The structure of a metal–air battery is schematically shown in Fig. 1, which is composed of a metal anode, an air electrode, and a separator soaked in metal-ion conducting electrolyte. In a discharge process, the metal anode is oxidized and releases electrons to the external circuit. At the same time, oxygen accepts the electrons from the anode and is reduced to an oxygen-containing species. The oxygen-reduced species or dissociated metal ions migrate across the electrolyte and combine with the counterpart to form metal oxides. Conversely, the charge process is reversed, with metal plating at the anode and oxygen evolving at the cathode. Typically, metal–air batteries are divided into two types according to the electrolyte: one is a cell system using an aqueous electrolyte such as Zn–air and the other is a water-sensitive system using organic electrolyte such as nonaqueous Li–air.[13,18] The aqueous electrolyte configuration is widely used in Zn–air batteries and has prominent virtues of low cost, wide availability, and high ionic conductivity. However, for a light metal such as Li, the theoretical value of the Li/Li^+ couple voltage is fairly negative, leading to violent reactions between lithium and water and making metallic lithium unsafe to operate directly in an aqueous environment. As a result, the aqueous Li–air system requires a specially designed water-stable layer or membrane to protect the Li anode,[19–24] which would add to the complexity of the batteries. In contrast, the introduction of a nonaqueous electrolyte significantly suppresses the anode corrosion and also enhances the metal–air cell voltage.[25] In the nonaqueous system it has been proved that the reduction products can be reversed into the original reagents and is advantageous for the rechargeability. Moreover, the theoretical energy density of a nonaqueous Li–air battery system is higher than that of an aqueous Li–air battery system because of the water or acid being involved in the reactions in the aqueous system. To date, the nonaqueous configuration has attracted the most effort worldwide compared to other electrolyte systems in Li–air batteries.

In practice, energy conversion in an electrochemical processes is often limited by high-activation barriers, which requires extra energy to overcome them. The extent of the barrier is defined by the overpotential or faradic efficiency. A high overpotential or low faradic efficiency will lead to the waste of energy as heat. Electrocatalysts are thus always applied to modify an electrode, in order to lower the activation energy and increase the conversion rate. The performance of an electrocatalyst could limit the properties of an electrochemical system, such as energy efficiency, rate capacity, lifetime, and cost, which makes it a key component of efficient electrochemical conversion.[5] The fundamental reactions of Zn–air and Li–air batteries are as follows: $Zn + O_2 \rightarrow ZnO$ and $Li + O_2 \rightarrow Li_2O_2$, respectively. The reaction process is similar to fuel cell with H_2 oxidation at the anode. In these reactions, the common issue involves the oxygen electrochemistry. During the development of the above energy devices, it was found that the main issue is the sluggish kinetics of the oxygen electrochemical reactions, resulting in a limited practical energy density. A typical discharge–charge loop is schematically shown in Fig. 2. The overpotentials from both ORR (η discharge) and OER (η charge) significantly diminish the power output and round-trip efficiency of metal–air batteries. So the critical element in the pursuit of this quest is the discovery of efficient and cost-effective catalysts for use in electrochemical energy conversion processes, such as the ORR and OER, which are central to the efficiencies of fuel cells and metal–air batteries.[6] Due to the similarity of principle between low-temperature fuel cells and metal–air batteries, most of the catalytic materials are universal.

Great challenges still exist in oxygen electrocatalysts for metal–air batteries, as mentioned in the previous reviews.[4,12,26–31] Electrocatalysts for the oxygen reduction reaction and oxygen evolution reaction play a key role and determine the power, energy density, and energy efficiency of metal–air batteries, especially for Li–air batteries. For example, current Li–air batteries can only be discharged–charged at a current density of 0.1–0.5 mA cm^{-2} (in comparison, >10 mA cm^{-2} for a Li-ion battery, >1500 mA cm^{-2} for polymer electrolyte membrane fuel cells), and the voltage gap between the charge and discharge is

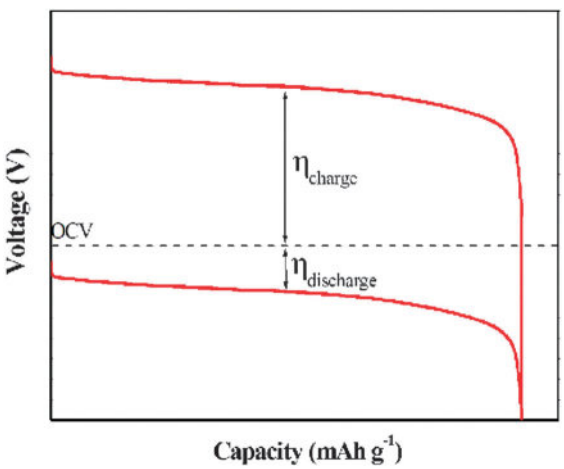

Fig. 2 A typical discharge–charge loop for a metal–air battery.

larger than 1.0 V, which results in a low voltage efficiency of $<70\%$ (in comparison with >90% for a Li-ion battery).[26] These can be largely attributed to the poor performance of the air (oxygen) electrode because of the sluggish kinetics for oxygen reduction/evolution. To achieve the rational design of efficient catalysts for the ORR and OER, it is also necessary to gain critical insights into the detailed mechanisms of the ORR and OER at air electrodes. Although the understanding of oxygen electrocatalysts in aqueous systems has been developed over the last few decades, this process is just beginning for nonaqueous Li–air cells, and the design principles for a good ORR or OER catalyst are not yet established. Recent work by Giordani *et al.* shows a strong correlation between the ability of the catalysts to decompose hydrogen peroxide and the charging potential of Li–air cells, and a relationship has been tentatively constructed among the catalytic activity of a series of materials toward aqueous oxygen electrocatalysis and nonaqueous electrocatalysis.[32,33]

In this review, we will focus on the applications of oxygen reduction and evolution electrocatalysts in metal–air batteries and summarize the development of metal–air batteries from a material chemistry point of view. Specifically, we will review the status and challenges and provide a perspective of oxygen electrocatalysts for aqueous and nonaqueous metal–air batteries. The content is organized as follows: (1) fundamental understanding of oxygen electrocatalysis in aqueous and nonaqueous electrolytes, (2) current electrocatalysts under investigation for metal–air batteries, (3) challenges from aqueous to nonaqueous electrolytes, and (4) concluding remarks. Through this review, it will be emphasized that one catalyst can simultaneously play catalytic roles in aqueous and nonaqueous systems. Previous research mainly focued on aqueous systems, such as fuel cell and Zn–air batteries, and the development of oxygen catalysts in aqueous systems has made great progress recently. However, for the nonaqueous Li–air batteries, the oxygen catalysts are still in the early stages of development. Since the fundamental features of the ORR and OER processes in aqueous and nonaqueous electrolytes share similarities, what is learnt from aqueous systems can promote the development of nonaqueous systems. The similarity in both systems will provide some guidance for the development of new electrocatalysts when we shift from aqueous to nonaqueous systems. The discussions and insights provided in this review reflect the most recent approaches and directions for oxygen electrocatalyst developments and they will be directly applicable for the understanding and improvement of other oxygen conversion systems. It should be noted that most Li–air batteries are tested in pure oxygen in order to avoid contaminants from air, so ''Li–air'' or ''Li–O_2'' are usually used without differentiation.

2 Oxygen electrochemical reactions

In this section, the basic oxygen electrochemical reactions in metal–air batteries are discussed separately on the basis of aqueous and organic electrolytes.

2.1 Oxygen electrochemistry in aqueous electrolyte

Alkaline solutions are commonly applied for aqueous metal–air batteries because metal anodes are relatively stable and materials problems are less serious. On the contrary, the acidic electrolyte is inappropriate for practical applications due to violent reactions with the metal anode, leading to severe anode corrosion. However, alkaline media also have some drawbacks when air is used as the combustant, as carbonate ions accumulate in the liquid electrolyte over time. To circumvent this drawback, it is necessary to feed purified air or to employ a selective membrane that is permeable to O_2.

In aqueous electrolyte, the electrochemical reaction kinetics of oxygen is generally rather slow, when without any catalysts. The presence of an oxygen electrocatalysts can accelerate the ORR or OER process. The ORR process in the air electrode of a metal–air battery includes several steps: oxygen diffusion from the outer atmosphere to the catalyst surface, oxygen absorption on the catalyst surface, transfer of electrons from the anode to the oxygen molecules, weakening and breaking of the oxygen bond, and the removal of the hydroxyl ion product from the catalyst surface to the electrolyte.[29] The OER in a metal–air battery during charging involves the reverse process of the ORR. However, the electrochemistry of oxygen is very complicated and difficult to describe due to its strong irreversibility, and the reaction process contains a series of complex electrochemical reactions which are involved in multi-step electron-transfer processes.[34–37] Different catalysts may correspond to different reaction mechanisms. Metals and metal oxides are two types of classical oxygen catalysts and their related mechanisms have been intensively studied. On the surface of metal catalysts, a four-electron pathway or a two-electron pathway may proceed for the ORR, depending on the adsorption type.[34,38] There are two adsorption types: bidenate O_2 adsorption (two O atoms coordination with the metal) and end-on O_2 adsorption (one O atom coordination perpendicularly to the surface), corresponding to the direct 4e pathway and the 2e pathway (with generated peroxides), respectively. For the bidentate type, the reactions are as follows:

$$O_2 + 2H_2O + 2e^- \rightarrow 2OH_{ads} + 2OH^-$$

$$2OH_{ads} + 2e^- \rightarrow 2OH^-$$

$$\text{Overall: } O_2 + 2H_2O + 4e^- \rightarrow 4OH^-$$

For the end-on manner, the reactions can be given as:

$$O_2 + H_2O + e^- \rightarrow OH_{2,ads} + OH^-$$

$$OH_{2,ads} + e^- \rightarrow OH_2^-$$

$$\text{Overall: } O_2 + H_2O + 2e^- \rightarrow OH_2^- + OH^-$$

The 2e oxygen reduction may be followed by either a further 2e reduction of peroxide or the chemical disproportionation of peroxide:

$$HO_2^- + H_2O + 2e^- \rightarrow 3OH^-$$

$$\text{or } 2HO_2^- \rightarrow 2OH^- + O_2$$

In the case of metal oxides, the ORR pathways at the surface follow the same principle, but with a different charge distribution.

The surface cations of stoichiometric oxides are not fully coordinated with oxygen atoms. In aqueous solution, anion coordination is completed by the oxygen of a water molecule. Consequently, reduction of a surface cation by an electron from the external circuit is charge-compensated by protonation of a surface oxygen ligand.[36] The corresponding pathways could be briefly given as:

$$2M^{m+}\text{–}O^{2-} + 2H_2O + 2e^- \rightarrow 2M^{(m-1)+}\text{–}OH^- + 2OH^-$$

$$O_2 + e^- \rightarrow O_{2,ads}{}^-$$

$$2M^{(m-1)+}\text{–}OH^- + O_{2,ads}{}^- + e^- \rightarrow 2M^{m+}\text{–}O^{2-} + 2OH^-$$

or more probably

$$M^{m+}\text{–}O^{2-} + H_2O + e^- \rightarrow M^{(m-1)+}\text{–}OH^- + OH^-$$

$$O_2 + e^- \rightarrow O_{2,ads}{}^-$$

$$M^{(m-1)+}\text{–}OH^- + O_{2,ads}{}^- \rightarrow M^{m+}\text{–}O\text{–}O^{2-} + OH^-$$

$$M^{m+}\text{–}O\text{–}O^{2-} + H_2O + e^- \rightarrow M^{(m-1)+}\text{–}O\text{–}OH^- + OH^-$$

$$M^{(m-1)+}\text{–}O\text{–}OH^- + e^- \rightarrow M^{m+}\text{–}O^{2-} + OH^-$$

The ORR pathways and mechanisms may vary with the catalytic materials and electronic structure. Recent findings reflect the critical influence of the σ* orbital and the metal–oxygen covalency on the competition between $O_2{}^{2-}/OH^-$ displacement and OH^- regeneration on the surface of transition-metal ions as the rate-limiting steps of the ORR, and thus highlight the importance of the electronic structure in controlling the oxide catalytic activity.[39]

The reaction pathways involved in oxygen evolution are also rather complex. Oxygen is generally evolved from an oxide phase, rather than the bare metal.[36,37] Thus, the mechanisms are also likely to change depending on the electrode materials and the site geometry of the metal cation. The changeable valance state of the metal ion is important for oxygen evolution catalysis because the catalysis reaction is induced from the interaction between metal ions and oxygen intermediates and the formation of a bond by changing the valence state. The metal cation site geometry can affect the catalysis process and it changes not only the adsorption energy of the oxygen species, but also the activation energy for the verification of the cation oxidation state and the related coordination number.[36,40–42] For a rechargeable metal–air battery, a bifunctional catalyst on the cathode is necessary and the most promising bifunctional catalysts are oxides containing surface reactions $M^{m+}\text{–}O^{2-} = M^{(m-1)+}\text{–}O^-$ biased toward the right-hand side. The oxygen evolution reaction (OER) in alkaline solution is then accessible as:

$$M^{m+}\text{–}O^{2-} + OH^- \rightarrow M^{(m-1)+}\text{–}O\text{–}OH^- + e^-$$

$$M^{(m-1)+}\text{–}O\text{–}OH^- + OH^- \rightarrow M^{m+}\text{–}O\text{–}O^{2-} + H_2O + e^-$$

$$2M^{m+}\text{–}O\text{–}O^{2-} \rightarrow 2M^{m+}\text{–}O^{2-} + O_2$$

As the typical oxygen evolution catalysts, RuO_2 and IrO_2 have very high activity benefiting from their relatively low redox potentials (*ca.* 1.39 and 1.35 V *vs.* RHE, respectively)[43] and the high conductivity of their oxide films. Nickel is also widely used as an electrocatalyst for oxygen evolution in alkaline electrolytes. However, at high potentials, lower conductivity phases involving Ni^{4+} are formed which will reduce the performance. Some transition metal oxides are other kinds of efficient catalysts for oxygen evolution. This is particularly the case in some spinel type oxides, such as $NiCo_2O_4$.[37]

For a Zn–air battery, oxygen is reduced to hydroxyl ions and zinc ions from the anode and can combine with hydroxyl ions to form zincate ions ($Zn(OH)_4{}^{2-}$), which may decompose to produce ZnO. The battery reactions can be described as follows:

$$\text{Cathode: } O_2 + 2H_2O + 4e^- \leftrightarrow 4OH^-$$

$$\text{Anode: } Zn + 4OH^- - 2e^- \leftrightarrow Zn(OH)_4{}^{2+}$$

$$\text{Overall: } 2Zn + O_2 + 2H_2O + 4OH^- \leftrightarrow 2Zn(OH)_4{}^{2-}$$

It is challenging to make an electrically rechargeable zinc–air battery because the reversibility of the zinc anode is difficult. In the charge–discharge cycling process, zinc metal undergoes shape changes, such as the formation of dendrites.[44] The stable existence of zincate ions $Zn(OH)_4{}^{2-}$(aq) in alkaline solution is a prerequisite for developing a secondary zinc electrode. However, $Zn(OH)_4{}^{2-}$(aq) will reach a saturation point in the hydroxide electrolyte during discharge. After exceeding this point, zincate ions are decomposed to ZnO, a white solid powder that acts as an insulator, making the rechargeability difficult. The reaction involved is: $Zn(OH)_4{}^{2+} \rightarrow ZnO + H_2O + 2OH^-$. To realize the rechargeability, the important issue is to understand the behavior of the zincate ion in an alkaline electrolyte and increase the solubility.[45,46]

2.2 Oxygen electrochemistry in nonaqueous electrolytes

As widely investigated in aqueous media, oxygen reduction in nonaqueous solvents has been studied for several decades.[47–51] Previous electrochemical studies on the oxygen reduction reaction (ORR) in organic solvents demonstrated that it is possible to reduce molecular oxygen to superoxide (O^{2-}) in a nonaqueous environment. Today, the ORR and OER in nonaqueous Li^+ electrolytes are receiving considerable attention because they are the reactions on which the operation of a high-energy density Li–air (O_2) battery depends.[52,53] It is crucial to understand the O_2 reaction mechanisms in nonaqueous electrolytes.

Much effort has been devoted to clarify the $Li^+\text{–}O_2$ electrochemical reactions. For example, Laoire *et al.* explored the cation effect on the ORR and OER and found that the cathode reaction proceeds through a one-electron reversible process with the $O_2/O_2{}^-$ redox couple in electrolytes with large cations, such as tetrabutylammonium (TBA^+) and tetraethylammonium (TEA^+), whereas in the Li^+-containing electrolyte, the oxygen reduction reactions proceed in a stepwise fashion to form $O_2{}^-$, $O_2{}^{2-}$ and O^{2-} as products and these reactions are kinetically irreversible or quasi-reversible processes.[54,55] Such significant changes in the ORR thermodynamics between large cations and

smaller metal cations can be rationalized using the hard soft acid base (HSAB) theory. According to HSAB, TBA^+, a soft acid, can effectively stabilize the soft base, O_2^- (due to its relatively large radius and low charge density), preventing further reactivity. However, alkali metal cations such as Li^+, which are hard acids, cannot effectively stabilize O_2^-. Therefore, disproportionation to Li_2O_2 from the unstable LiO_2 is favored in the presence of lithium ions. The strong ionic bond between Li^+ and the superoxide ion results in their precipitation on the electrode surfaces, which would passivate the electrode and shuts down the reduction, making the reaction irreversible. In contrast, the $TBAO_2$ is soluble in the electrolyte, and the redox reaction is reversible. Recently, the same group further applied HSAB to study the ORR and OER processes with a series of cations with increasing Lewis acidity (*i.e.*, cation hardness): $TBA^+ < PyR^+ < EMI^+ < K^+ < Na^+ < Li^+$ (Fig. 3).[56] It was found that the superoxide ions can be effectively stabilized by TBA^+, PyR^+, EMI^+ and K^+ cations without disproportionating to form peroxide, which enables the reversible one-electron reactions. In contrast, hard cations such as Li^+ and Na^+ promote the disproportionation of metal superoxide to form metal peroxide, yielding an irreversible two-electron (per O_2) process. Interestingly, the nonaqueous K–O_2 and Na–O_2 batteries are demonstrated to be much more reversible than Li–O_2 batteries.[57,58] A solvent effect is also observed in the nonaqueous system and the polarity of the nonaqueous solvents influences the ORR process due to the acid–base interaction.[55]

It can be found that an identified distinction between the use of nonaqueous and aqueous electrolytes is that in aqueous electrolytes the preferred reduction product is water or hydrogen peroxide, corresponding to a four- or two-electron reduction of O_2, respectively, as opposed to the formation of superoxide in organic electrolytes. The reaction process does not involve the cleavage of the O–O bond, which is a notoriously sluggish process that usually requires precious metal catalysts. Another feature is that O_2^- is a weakly adsorbed radical[59] and is highly soluble in electrolyte, and the electrode may work as only an electron transfer media; so a catalytically insensitive phenomenon in oxygen reduction is observed on Pt, Au, Hg, and carbon electrodes in nonaqueous electrolytes with large cations.[60,61] Compared with the above mentioned catalyst-indispensable cathode reactions in aqueous electrolytes, the oxygen reduction can proceed with only carbon catalysts in nonaqueous electrolytes containing Li^+. Carbon has sufficient ORR catalytic activity at low current density, and the kinetics of the ORR process is much faster than the counterpart OER process.

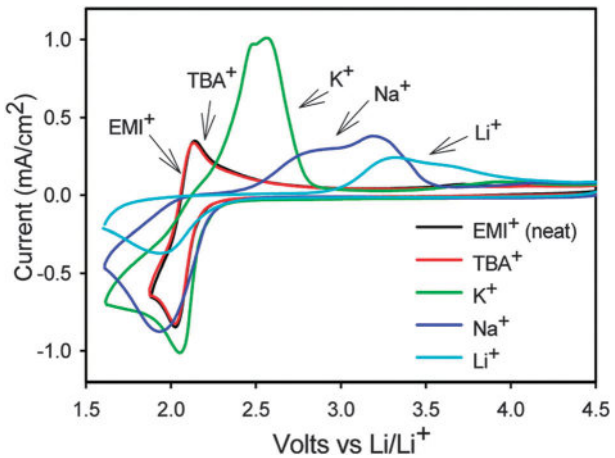

Fig. 3 Cyclic voltammogram of neat EMITFSI along with various salts at 0.025 M concentration on a GC electrode at 100 mV s^{-1}. Reprinted with permission from ref. 56. Copyright 2012, American Chemical Society.

To further illustrate the process, Bruce and co-workers studied the ORR/OER in Li^+-containing acetonitrile by using *in situ* surface-enhanced Raman spectroscopy (SERS) and provided direct evidence that LiO_2 is indeed an intermediate of O_2 reduction in nonaqueous solvent, which then disproportionates to peroxide Li_2O_2.[62] However, in the reverse charging process, LiO_2 and other intermediates are not detected from the spectroscopy data, which means that Li_2O_2 oxidation does not follow the reverse pathway to reduction and decomposes directly in a one-step reaction to evolve O_2. On the basis of the experimental observation, they concluded that the ORR and OER pathways in Li^+-containing nonaqueous electrolyte are as following:

$$\text{ORR: } O_2 + e^- \rightarrow O_2^-$$

$$O_2^- + Li^+ \rightarrow LiO_2$$

$$2LiO_2 \rightarrow Li_2O_2 + O_2$$

$$\text{OER: } Li_2O_2 \rightarrow 2Li^+ + O_2 + 2e^-$$

The thermodynamic potential (U_0) of Li–O_2 batteries with nonaqueous electrolytes can be calculated to be 2.96 V from the Nernst equation.[63,64] Generally, the Li–O_2 batteries presented a modest overpotential for discharge ($\sim$0.3 V) but much higher overpotentials ($\sim$1.0–1.5 V) for charging. This large voltage gap results in a low round-trip efficiency of $<$70%, meaning that more energy is required to charge the battery than released during discharge. This is contrast with >90% in LIBs.[31]

For the OER process in nonaqueous electrolyte, a new two-stage decomposition process of Li_2O_2 was proposed by Shao-Horn and Lu as depicted in Fig. 4.[65] The first OER stage occurs at low overpotentials ($<$400 mV) with a slopping voltage profile, whose kinetics are relatively insensitive to charge rates and catalysts. This stage could be attributed to the delithiation of the outer part of Li_2O_2, forming a LiO_2-like species ($Li_2O_2 \rightarrow LiO_2 + Li^+ + e^-$) *via* a solid-solution route, which chemically disproportionates to evolve O_2 ($LiO_2 + LiO_2 \rightarrow Li_2O_2 + O_2$), yielding an overall $2e^-/O_2$ OER process ($Li_2O_2 \rightarrow 2Li^+ + O_2 + 2e^-$). This hypothesis is supported by the work of McCloskey *et al.*, showing that molecular O_2 was evolved during the sloping charging step (with DME solvent) with an overall $2e^-/O_2$ OER process.[66,67] The second stage takes place at high overpotentials (400–1200 mV), whose kinetics are sensitive to charge rates and catalysts, which can be ascribed to the oxidation of bulk Li_2O_2 particles to form Li^+ and O_2 *via* a two-phase transition. This reaction is associated with nucleation and growth type processes and requires the overcoming of a significant reaction barrier. The dependence of charge voltage on the catalysts is in agreement

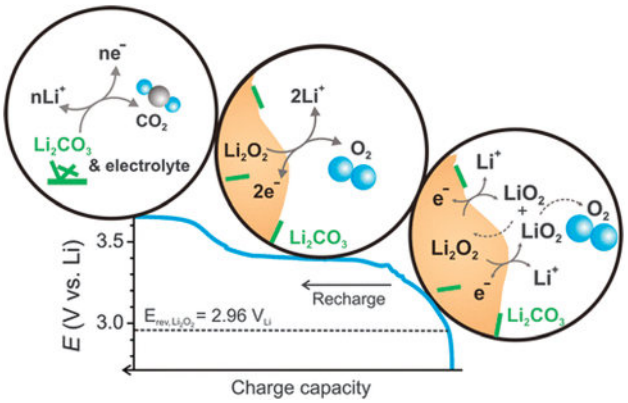

Fig. 4 Proposed reaction mechanism of the Li–O_2 recharging process. Reprinted with permission from ref. 65. Copyright 2013, American Chemical Society.

with the reported results.[68–70] Lastly, a sharply rising charge voltage was assigned to the decomposition of carbonate-type byproducts and electrolyte, possibly generated during discharge, which was predicted from the evolution of CO_2.[71,72] The proposed mechanism in Fig. 4 agrees with the insensitivity of charge overpotential to catalysts at the initial charge stage and the dependence of charge overpotential on catalysts beyond the initial stage.[31]

Oxygen electrochemistry in practical Li–air batteries is a very complicated process. The ORR and OER processes can be influenced by electrolytes, electrode materials, oxygen pressure, and even electrochemical stressing.[73–76] In addition, the intermediates generated in the cathode reactions are less dissolvable in the organic electrolyte and lead to the accumulation of solids in the cathode, which may clog the pores of the air electrode, block the catalyst surface, and electrically passivate the battery. The charge transfer and mass transport at the interface of the cathode are hence limiting factors that affect battery performance.[74] Thus, the specific capacity of a Li–air battery correlates intimately with the character of the cathode, such as porosity, conductivity, stability, catalytic activity and so on. Moreover, the intermediates in the Li–O_2 electrochemical reactions, for example, O_2^-, O_2^{2-}, and LiO_2/LiO_2^-, are very reactive.[25] They can easily decompose most organic solvents. This leads to Li–air battery discharge products of Li_2CO_3, LiOH, and lithium alkyl carbonates, instead of only the desired product (Li_2O_2), in which such side reactions make the Li–air battery unrechargeable.[78–81] Recent work has shown that the oxidation of Li_2O_2 may produce highly reactive singlet oxygen during the charging process, which is 0.98 eV higher in energy than the ground-state triplet O_2 and could also readily react with the electrolyte.[82]

3 Oxygen electrocatalysts for metal–air batteries

Oxygen electrocatalysts have been demonstrated to be crucial for improving the power density, cycling capability, and energy conversion efficiency of metal–air batteries. In recent years, great efforts have been made in the development of electrocatalysts for both primary and rechargeable metal–air batteries. Even though recent reports have questioned the true electrocatalytic effect in Li–air batteries,[67] the research results can still provide some guidance for future investigation on oxygen electrocatalysts. Furthermore, due to similar principles, most of the catalytic materials applicable to fuel cells could also serve in metal–air batteries, and so could the strategies and techniques to enhance the cathode efficiency. The electrocatalysts can be roughly classified into the following seven categories: (1) transition metal oxides, containing single-metal oxides and mixed-metal oxides; (2) functional carbon materials, including nanostructured carbons and doped carbons; (3) metal oxide–nanocarbon hybrid materials; (4) metal–nitrogen complex, including non-pyrolyzed and pyrolyzed; (5) transition metal nitrides; (6) conductive polymers; (7) noble metals, alloys and oxides, for example, Pt, Ag, PtAu, and RuO_2. We will summarize the applications of such catalysts in aqueous and nonaqueous metal–air batteries, focusing on the most recently reported progress. Through this review, it will be emphasized that one catalyst can simultaneously play catalytic roles in aqueous and nonaqueous systems, and what is learnt from aqueous systems can be used to promote the development of nonaqueous systems.

3.1 Transition metal oxides

Transition-metal oxides represent a large family of oxygen electrocatalysts, including single-metal oxides and mixed-metal oxides. As an alternative to noble metals, transition-metal oxides have many advantages such as high abundance, low-cost, easy-prepared, environmental friendliness and so on. Transition metal elements possess multiple valences, resulting in a variety of oxides with different crystal structures. In this section, we will discuss four type of oxide electrocatalysts according to their composition and structure.

3.1.1 Single-metal oxides. Manganese oxides have received intensive attention because of their variable valences and abundant structures, giving rise to rich redox electrochemistry. Manganese oxides can simultaneously serve in catalytic ORR and OER reactions, thus making them attractive as bifunctional catalysts for oxygen electrochemistry. MnO_2 was first reported in the early 1970s for the ORR,[83] since then many research efforts have been contributed to evaluate and optimize the MnO_x-based catalysts for the air cathode.[84–91] The chemical composition, texture, morphology, oxidation state, and crystalline structure have been examined as functions of the electrocatalytic properties. For example, Chen and co-workers found that the catalytic activities of MnO_2 depend strongly on the crystallographic structure, following an order of α- > β- > γ-MnO_2.[87] The change is attributed to a combined effect of their intrinsic tunnel (interspace in the stack of [MnO_6] octahedron) size and electrical conductivity. Meanwhile, the morphology is another important influential factor on the electrochemical properties. Among the same phase, α-MnO_2 nanospheres and nanowires outperform the counterpart microparticles, due to their smaller size and higher specific surface areas. Recently, the same group has

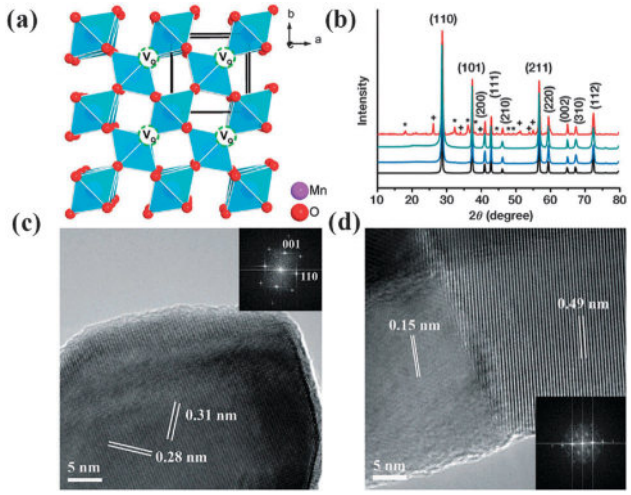

Fig. 5 (a) Structure of rutile-type MnO_2 with oxygen vacancies. (b) XRD patterns of different oxides. The symbols * and + denote Mn_3O_4 and MnOOH, respectively. From top to bottom: H_2/Ar-350-2h, Ar-350-2h, Air-350-2h, pristine. (c) and (d) HRTEM images of pristine β-MnO_2 (c) and β-MnO_2 heated in Ar (d), the insets show the FFT patterns. Reprinted with permission from ref. 91, copyright 2013, Wiley-VCH.

investigated the defect effect on the activity of rutile-type β-MnO_2 by introducing native oxygen defects without modification by foreign additives (Fig. 5a).[91] As shown in Fig. 5b, heat treatment in Ar and air leads to oxygen nonstoichiometry, which is compensated by the reduction of Mn^{4+} to Mn^{3+}. More interestingly, two domains can be observed after heat treatment in Fig. 5d, which is indicative of a typical pyrolusite lattice and a new structure that corresponds to oxygen-vacancy-induced structural variations of MnO_2. The results show that oxygen-vacancy-bearing oxide enables a more positive potential, larger current and lower peroxide yield for the ORR electrocatalysis process, and also favors OER catalysis. DFT computational studies further reveal the presence of oxygen vacancies enhances the interaction between oxygen-containing species and MnO_2 surfaces and reduces the kinetic barrier.

Doping of a low-valent element can enhance the catalytic activity of MnO_x toward the ORR. MnO_x doped with a variety of elements (*e.g.*, Ni, Mg and Ca) exhibited higher activity than non-doped materials.[92–95] The results from Roche *et al.* show doping the MnO_x/C electrocatalysts directs the ORR toward the four-electron pathway.[94] The first electrochemical step of the 4-electron ORR mechanism is probably the quasiequilibrium proton insertion process into MnO_2 leading to MnOOH, while the second electron transfer, consisting of the electrosplitting of the $O_{2,ads}$ species (yielding O_{ads} and hydroxide anions), is the rate determining step. The presence of doping metal cations may stabilize the intermediate Mn^{III}/Mn^{IV} species, which assists this second charge transfer to oxygen adatoms. As a result, the ORR rate is enhanced for doped MnO_x/C electrocatalysts. The chemical composition is also an important factor that affects the catalytic activity. Ohsaka's group found that the peak current changed greatly depending on the kind of MnO_x species incorporated into the MnO_x/Nafion modified gold electrodes, following the sequence of $Mn_5O_8 < Mn_3O_4 < Mn_2O_3 < MnOOH$.[84,85] Moreover, optimization of the composition combined with rational nanostructures will further enhance the activity. An typical example, inspired by nature's catalyst for water oxidation, Jaramillo and Gorlin developed a thin-film analogue consisting of a nanostructured Mn(III) oxide.[96] This nanostructured Mn(III) oxide demonstrates bifunctional activity and its OER activity is on par with the best reported Mn oxide OER catalyst, while its ORR activity matches or surpasses the activities of the best reported Mn oxide ORR catalysts. More importantly, its bifunctional activity is comparable to that of precious metals. Recently, *in situ* X-ray absorption spectroscopy has been applied to study the active sites of the bifunctional Mn_xO_y catalyst by the same group. It was found that a disordered $Mn_3^{II,III,III}O_4$ phase contributes to the ORR, while a mixed $Mn^{III,IV}$ oxide is pertinent to the observed OER activity.[97]

Cobalt oxide (Co_3O_4) is another kind of promising candidate of non-precious bifunctional ORR/OER catalysts in alkaline media owing to its high electrocatalytic activity and tunable composition.[98,99] Two valences of Co^{2+} and Co^{3+} ions co-existed in the Co_3O_4 crystal structure. In general, the ORR is a surface-structure sensitive reaction on electrodes and the reaction takes place at active sites associated with the cations at the oxide surface in a higher oxidation state.[100] So the exposed active sites of Co^{3+} ions on the Co_3O_4 electrocatalyst play a determinant role in the performance for the ORR, in which these cations would act as donor–acceptor reduction sites, with the donor electronic properties with respect to the species in solution and acceptor character with respect to the solid by capture of electrons.[101] To enhance the catalytic activity for the ORR, an effective approach is to increase the exposed Co^{3+} ions through nanostructures of Co_3O_4. Recently, Zhao *et al.* developed a solvent-mediated method to control the morphology of Co_3O_4 nanostructures. The rod and spherical nanostructures were produced by adjusting the mole ratio of water and dimethylformamide in the mixed solvent.[102] Interestingly, it was found that Co_3O_4 nanorods exhibited the highest catalytic activity for the ORR among all the catalyst samples prepared under different conditions and even a higher catalytic activity for the ORR than the noble palladium catalyst does, indicating that the number and activity of the surface exposed Co^{3+} ions can be tailored by the morphology of the cobalt oxides.

Besides aqueous systems, single-metal oxides such as MnO_x have also been extensively studied as oxygen electrocatalysts in nonaqueous systems. For example, using α-MnO_2 nanowires as a catalyst, Bruce *et al.* demonstrated a capacity of 3000 mA h g^{-1} (based on carbon) and 10 cycles with good capacity retention in nonaqueous Li–air batteries.[103] Similar to that in aqueous electrolyte, the morphology of MnO_x in the nonaqueous electrolyte is also an important factor that affects the catalytic activity of MnO_x in Li–air batteries and the authors found that the MnO_2 nanowire exhibited higher catalytic activity than bulk MnO_2 in both the α- and β-phase. Since the first application of MnO_2 by the Bruce group, significant efforts have been devoted to the investigation of the catalytic activity of MnO_x in nonaqueous Li–air batteries.[104–113] Suib and co-workers compared the catalytic activity of α-MnO_2 catalysts with different morphologies in

both aqueous and organic electrolytes.[109] Among various morphologies, pure nanorods prepared from a solvent-free method displayed the highest ORR catalytic activity due to the low average oxidation state of manganese, small crystallite size, high surface area, and large pore volume. It was also found that the α-MnO_2 nanorods doped with Ni showed improved catalytic activity over the undoped counterpart, despite decreased pore size and volume. Truong *et al.* reported another interesting phenomenon about the morphology controlled catalytic activity. The authors synthesized uniform δ-MnO_2 microflowers consisting of assemblies of nanosheets, α-MnO_2 nanowires, and α-MnO_2 nanotubes with open ends by a microwave-assisted hydrothermal method.[110] As an oxygen catalyst in Li–air batteries, single-crystalline α-MnO_2 nanotubes exhibited much better stability than α-MnO_2 nanowires and δ-MnO_2 nanosheet-based microflowers in both the charge and discharge processes, indicating that the morphology and crystallinity of the MnO_2 nanostructures indeed influence the performance of the Li–air batteries. Recently, our group synthesized high aspect ratio γ-MnOOH nanowires by a simple one-step hydrothermal method.[111] Due to the advantageous combination of the intrinsically high catalytic activity and unique structure, the super-long nanowires greatly improve the discharge capacity, cycle stability, and rate retention in rechargeable nonaqueous Li–air batteries.

Structural defects are demonstrated to have a major effect on the catalytic activity of materials in nonaqueous electrolyte.[114] Nazar and co-workers demonstrated the defect effect in manganese oxides by acid leaching $Na_{0.44}MnO_2$ nanowires, as shown in Fig. 6.[68] Through the interaction between A_xMnO_2 (A = alkali or alkali-earth cations) manganese oxide and acid, A ions were exchanged by acidic protons and Mn^{3+} ions was disproportioned into Mn^{4+} ions remaining in the solid material and Mn^{2+} ions dissolved into solution, leading to the formation of vacancy defects in both the A-ion and Mn–O framework sublattices. Compared to the original $Na_{0.44}MnO_2$, open-tunnel "sodium deficient" $Na_{0.44-x}H_xMnO_2$ nanowires doubled the reversible capacity and lowered the OER potential (Fig. 6c and d) due to the structural defects and vacancies formed in the material upon acid leaching. Chemical modification of the tunnel structured manganese oxides may open new horizons in the understanding and design of effective cathode systems for Li–air batteries. Similarly, Trahey *et al.* synthesized an α-MnO_2–ramsdellite-MnO_2 composite by acid treatment of Li_2MnO_3.[115] This material provided an exceptionally high reversible capacity up to 5000 mA h g^{-1} (carbon + catalyst) during the early cycles and significantly reduced polarization during the initial charge voltage profile in the first couple of cycles. The reversible insertion reactions of lithium, lithium peroxide (Li_2O_2) and lithium oxide (Li_2O) in the tunnels of α-MnO_2, and the reaction of lithium with ramsdellite-MnO_2 were investigated by first principles density functional theory calculations. From the experimental and theoretical results, it is speculated that a Li_2O-stabilized and partially-lithiated electrode component, $0.15Li_2O{\cdot}\alpha\text{-}Li_xMnO_2$, that has $Mn^{4+/3+}$ character may facilitate the Li_2O_2–Li_2O discharge–charge chemistries providing dual electrode/electrocatalyst functionality.

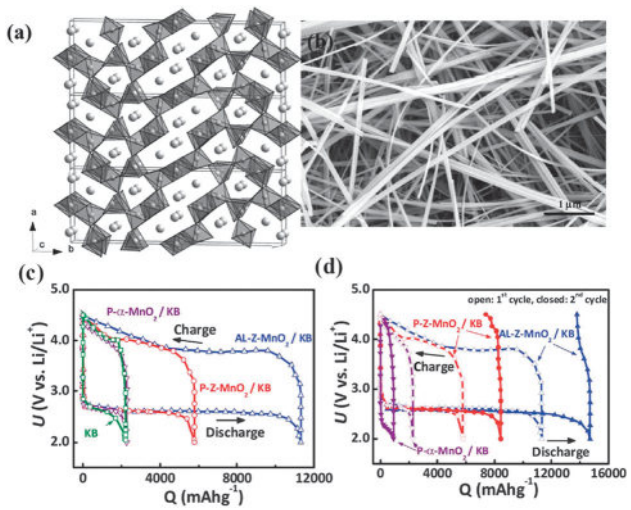

Fig. 6 (a) Crystal structure and (b) SEM images of the pristine $Na_{0.44}MnO_2$ nanowires. (c) Initial voltage profiles and (d) voltage profiles for 1st and 2nd cycles for pristine (P-Z-MnO_2/KB), acid-leached $Na_{0.44}MnO_2$ (AL-Z-MnO_2/KB), α-MnO_2 (P-α-MnO_2/KB) and carbon (KB) electrodes. Reprinted with permission from ref. 68, copyright 2012, Royal Society of Chemistry.

Besides MnO_x, other metal oxides such as Fe_xO_y, NiO, CuO and Co_3O_4 also have intrinsic activity for the electrochemical oxygen reaction and have been applied in nonaqueous systems.[116–119] For example, Wen and co-workers designed a free-standing-type cathode through chemically depositing Co_3O_4 on a Ni-foam without carbon and a binder.[117] The new air electrode delivered a high specific capacity up to (4000 mA h $g_{cathode}^{-1}$, where "cathode" means Co_3O_4 catalyst) and exhibited a small overpotential with a high discharge voltage (2.95 V) and the low charge voltage (3.44 V). The excellent performance was attributed to the abundant available catalytic sites of the particularly structured air electrode, the intimate contact of the discharge product with the catalyst, the effective suppression of the volume expansion in the electrode during subsequent deposition–decomposition of the discharge products, and the open pore system for unrestricted access of the reactant molecules. Recently, the same group synthesized another mesoporous cobalt oxide by hard-template method as a cathode with carbon in Li–O_2 batteries.[119] It was found that cobalt oxide with a large pore diameter, pore volume, and BET surface area exhibited a high round-trip efficiency of 81.4% (discharge and charge plateau is at ~2.85 and ~3.5 V, respectively) and a large specific capacity of 2250 mA h g_{carbon}^{-1}. The results further illustrate that a porous structure can contribute to fast ions or O_2 transport and increases the utilization of catalyst in nonaqueous electrolytes.

3.1.2 Mixed-metal oxides. Mixed-metal oxides on a spinel, perovskite, or pyrochlore structure are largely used for ORR and OER catalysts and their performances are discussed in this section.

3.1.2.1 Spinel-type oxides. Spinels are a group of oxides with the formula AB_2O_4, where A is a divalent metal ion (such as Mg, Fe, Co, Ni, Mn, or Zn) and B is a trivalent metal ion (such as Al, Fe, Co, Cr, or Mn). Spinel oxides with mixed valencies exhibit electrical conductivity or semiconductivity, enabling their direct use as electrode materials, and the electronic transfers take place with relatively low activation energies between the cations of

different valencies by hopping processes. Metal oxides possessing the spinel structure show good performances in oxygen evolution and reduction in alkaline solutions.[120–132] In the spinel structure, A^{2+} and B^{3+} cations occupy part or all of the tetrahedral and octahedral sites, respectively, and the content of the A^{2+} or B^{3+} cations in the formula can be varied to adjust the catalysis performance. For example, Rios *et al.* studied the change of electrocatalytic activity in $Mn_xCo_{3-x}O_4$ with Mn content x. $Mn_xCo_{3-x}O_4$ has a high electrical conductivity and ORR/OER activity.[120] It was found that $Mn_xCo_{3-x}O_4$ has the Mn^{4+}/Mn^{3+} redox couple located in the octahedral sites. Changes in the Mn^{4+}/Mn^{3+} content, as a function of x, were correlated to the activation energy of the conductance and the electrocatalytical capabilities of the ORR and OER. Interestingly, the catalysis of the ORR can be increased with the Mn content and probably more precisely with the amount of Mn^{4+}–Mn^{3+} pairs. In contrast, regarding the OER, surface Co^{3+} cations were commonly viewed as the active sites, and it appears that Mn strongly inhibits the oxidation of OH^- ions. It should be noted that Co_3O_4 belongs to the normal spinel crystal structure, based on a close-packed face centered cubic configuration of the O_2^- ions, in which Co^{2+} ions occupy one-eighth of the tetrahedral A sites, while Co^{3+} ions occupy one half of the octahedral B sites.

Besides the composition, the nanostructure of the catalyst also greatly influences the activity. Wu and co-workers reported self-standing mesoporous $Ni_xCo_{3-x}O_4$ nanowire arrays and their electrocatalytic performance in the OER.[124] The nanowire arrays were grown on Ti foils in an aqueous solution containing metal nitrate *via* ammonia-evaporation-induced growth (Fig. 7a–c). The nonuniform spatial distribution of elemental Ni is manifested by its EDX line profile across one piece of the microtomed cross-section in Fig. 7d. The mesoporous nature of the nanowires is also clearly evident in the HRTEM image as shown in Fig. 7e. There are two structural advantages of nanowire arrays grown directly on conductive substrates: firstly, the direct contact of the conductive substrate with the open space between the nanowires ensures that each nanowire participates in the reactions; secondly, the large surface areas associated with their mesoporous structures facilitates the diffusion of the active species and accelerates the surface reaction. From the electrochemical results (Fig. 7f and g), it was found that the introduction of Ni dopants modifies their physical properties, such as a larger roughness factor, better conductivity, higher active site density, and an enhanced electrochemical performance of the nanowires. For example, at the same overpotential, $NiCo_2O_4$ showed an approximately six times larger current density than pure Co_3O_4. Lin *et al.* also demonstrated that the core-ring structured $NiCo_2O_4$ nanoplatelets exhibited high electrocatalytic properties for the oxygen evolution reaction in alkaline solution, with an overpotential of 0.315 V at a current density of 100 mA cm^{-2}.[122]

The exploitation of novel synthesis technology is another important strategy for high-performance catalysts. Chen and co-workers have developed a facile and rapid room-temperature synthetic methodology for achieving highly active $Co_xMn_{3-x}O_4$ spinels.[126] The preparation is based on the reduction-recrystallization of

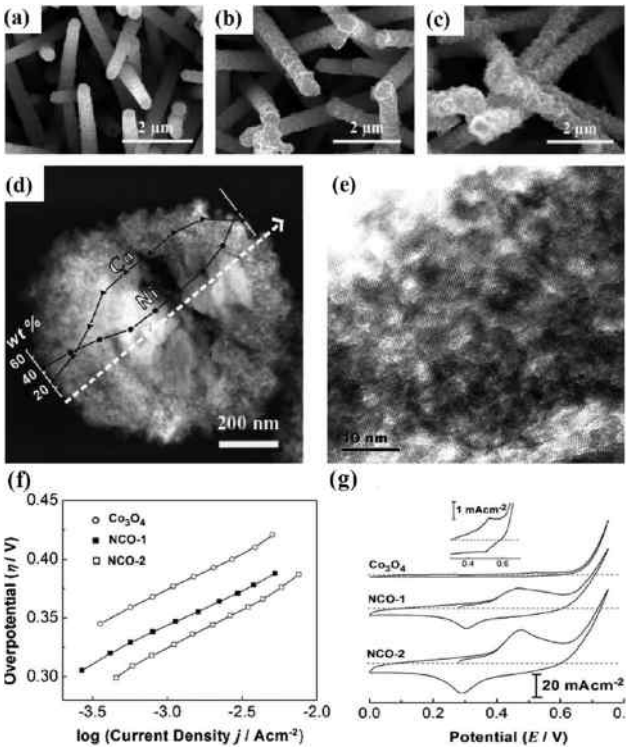

Fig. 7 SEM images of nanowire arrays grown on Ti foils: pure Co_3O_4 (a), $NiCo_2O_4$ (b, NCO-1), and $Ni_{1.5}Co_{1.5}O_4$ (c, NCO-2) with different doping levels. Nanowires became increasingly thicker and rougher with Ni doping. (d) Scanning transmission electron microscopy (STEM) image of the microtomed cross-section of $NiCo_2O_4$ with the associated EDX line profile of Co (triangles) and Ni (circles) along the dotted white line. (e) HRTEM image of $NiCo_2O_4$ showing the highly mesoporous nature. (f) Polarization curves and (g) cyclic voltammograms of pure Co_3O_4, NCO-1, and NCO-2. The insert of (g) magnifies the redox peaks of pure Co_3O_4. Polarization curves were iR compensated and the scan rate for cyclic voltammograms was 5 mV s^{-1}. Reprinted with permission from ref. 124, copyright 2010, Wiley-VCH.

amorphous MnO_2 precursors in aqueous solution containing divalent metal ions, such as Co^{2+}. Two representative nanocrystalline $Co_xMn_{3-x}O_4$ spinels, tetragonal and cubic, were synthesized using NaH_2PO_2 and $NaBH_4$ as the reductants, respectively. As shown in Fig. 8a and b, the tetragonal phase has a reticular and porous texture, while the cubic phase has a dense morphology with large particle; the difference of which may be related to their crystal structures (Fig. 8c and d). With the preserved morphology resembling the parent precursor, the prepared $Co_xMn_{3-x}O_4$ nanocrystalline spinels possess high surface areas, numerous defects and abundant vacancies, and manifest a remarkably higher activity towards the ORR/OER as compared to their counterparts synthesized at high temperature. Interestingly, it is found that the cubic spinel outperforms the tetragonal phase in intrinsic ORR catalytic activity (Fig. 8e), but the tetragonal spinel surpasses the cubic phase for the OER (Fig. 8f), due to the dissimilar binding energies of the oxygen adsorption on cobalt and manganese defect sites, as evidenced from both experimental and computational analysis. As an air electrode, the active $Co_xMn_{3-x}O_4$ spinel oxide delivered a stable

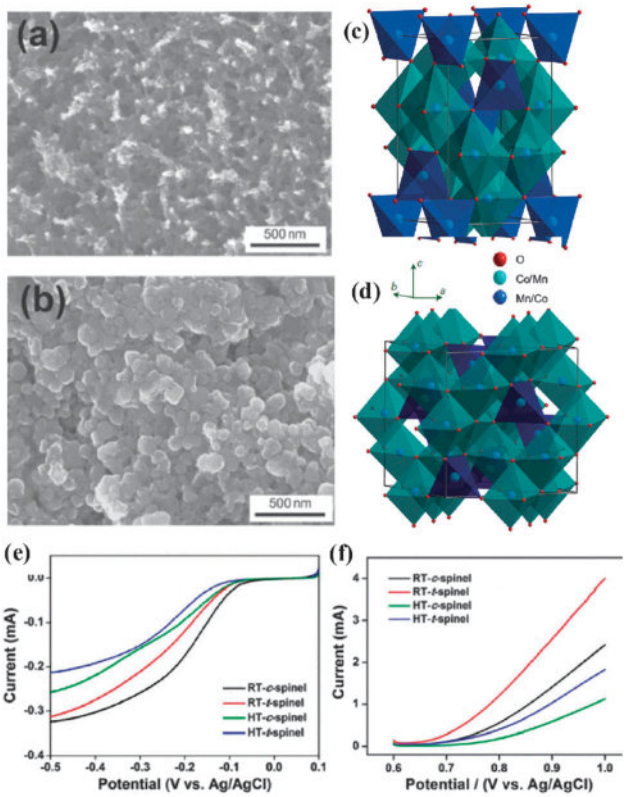

Fig. 8 SEM images and crystal structures of cobalt–manganese spinel oxides: (a) and (c) tetragonal-phase spinel nanostructures (RT-t-spinel); (b) and (d) cubic-phase spinel nanostructures (RT-c-spinel) synthesized at room temperature. Voltammograms of the (e) ORR and (f) OER recorded on different catalysts. Comparisons are also given to the counterpart cubic-phase (HT-c-spinel) and tetragonal-phase (HT-t-spinel) bulk spinels synthesized using a high-temperature ceramic method. Reprinted with permission from ref. 126. Copyright 2010, Nature Publishing Group.

galvanostatic discharge curve and considerable specific energy densities in a coin-type Zn–air battery.

The dispersion of the electrocatalyst in the polymer matrix provides a three-dimensional repartition of the electrocatalytic sites accessible to the reactant, maintaining good charge transport conditions throughout the polymer. Gautier *et al.* demonstrated the feasibility of multilayered polypyrrole (PPy)–Ox composite electrodes with the structure GC (glassy carbon)–PPy–PPy(Ox)–PPy for the ORR in neutral and acid electrolytes. Ox was a spinel oxide of $Ni_xCo_{3-x}O_4$ (x = 0.3 and 1) or $Cu_{1.4}Mn_{1.6}O_4$.[130,131] The polymer layers could stabilize the spinel catalyst in acid or alkaline electrolytes. With the assistance of PPy, the catalyst $Ni_{0.3}Co_{2.7}O_4$ shows an ORR activity of j = 1.85 mA cm^{-2} at −0.6 V (SCE) in an oxygen saturated 2.5 mM KOH + 0.8 M KCl solution at room temperature. The other spinel $Cu_{1.4}Mn_{1.6}O_4$–PPy-based composition showed good ORR activity in acidic solutions as well. Similarly, the spinel $CoFe_2O_4$–PPy showed a stable performance of j = −1.5 mA cm^{-2} at E = −0.5 V (SHE) over 8 h in an oxygen saturated 5 mM KOH + 0.5 M K_2SO_4 electrolyte at T = 25 °C.[132]

Spinel oxides have also been successfully applied in non-aqueous systems. For example, Cui's group reported mesoporous $NiCo_2O_4$ nanoflakes as electrocatalysts for rechargeable Li–O_2 batteries.[133] The as-prepared $NiCo_2O_4$ has a specific nanostructure with numerous catalytic active sites. The battery with a $NiCo_2O_4$-based cathode exhibited an improved performance, including a lower overpotential than pure carbon, reasonable specific capacity (1560 mA h g^{-1}), and enhanced cyclability with 10 stable cycles. The superior electrocatalytic behavior of $NiCo_2O_4$ towards both ORR and OER is attributed to its inherently electronic structure and favorable electronic transport capability. Moreover, the mesoporous and nanoflake structure also plays a crucial role in the electrochemical performance, which not only provides more electrocatalytic sites but also promotes mass transport (oxygen and ions) in the electrolyte, and eventually improves the capacity and cyclability.

3.1.2.2 Perovskite-type oxides. Perovskite-type oxides have the general formula ABO_3, which have been investigated extensively for their bifunctional catalytic abilities in alkaline electrolytes. Their properties can vary over a wide range by partially replacing A and B cations with other metals. The cubic perovskite crystal lattice is a rather rugged host for a variety of mixed transition metal oxides. The structure can even adapt to distortions from the basic cubic symmetry, giving rise to interesting properties. Generally speaking, A-site substitution mainly affects the ability of adsorbed oxygen, whereas B-site substitution influences the activity of the adsorbed oxygen.[134,135] Substituted perovskites can generally be described by the formula $A_{1-x}A'_xB_{1-y}B'_yO_3$, where A or A′ is a rare-earth or alkaline-earth metal and B or B′ is a transition metal. The activity of the transition metal oxide catalysts can be correlated with the ability of the cations to adopt different valency states, particularly when they form redox couples at the potential of oxygen reduction/evolution. Therefore, different perovskite type oxides with various replacements have been conducted as bifunctional catalysts.[136–138] Recently, Sunarso *et al.* investigated the oxygen reduction reaction activity of La-based perovskite oxides in alkaline medium.[139] The authors found that for $LaMO_3$ (M = Ni, Co, Fe, Mn and Cr), the ORR performance is enhanced in the order of $LaCrO_3$, $LaFeO_3$, $LaNiO_3$, $LaMnO_3$, and $LaCoO_3$, while for $LaNi_{0.5}M_{0.5}O_3$, the ORR current performance is enhanced in the order of $LaNi_{0.5}Fe_{0.5}O_3$, $LaNi_{0.5}Co_{0.5}O_3$, $LaNi_{0.5}Cr_{0.5}O_3$, and $LaNi_{0.5}Mn_{0.5}O_3$. Moreover, substituting half of the nickel with cobalt, iron, manganese, or chromium translates the ORR to a more positive onset potential, suggesting the beneficial catalytic effect of two transition metal cations.

Perovskite-type oxides of the composition $La_{1-x}Ca_xMO_3$ (M = Ni, Mn, Co) have attracted considerable attention because of their reasonable electrocatalytic activities and corrosion resistance.[140,141] Among these candidate materials, $La_{0.6}Ca_{0.4}CoO_3$ can be found in many demonstration batteries and can potentially replace noble metals in alkaline medium.[142,143] It simultaneously shows good ORR and OER catalytic activities and is considered to be the most promising bifunctional catalyst.[144–146] Interestingly, the electrocatalytic properties can be tuned by altering the oxidation state of cobalt. Narayanan *et al.* found that the binding energy of the cobalt $2p_{3/2}$ level increased with the annealing temperature in the X-ray photoelectron spectroscopy

(XPS) measurements and this observation correlated with the activity of the catalyst toward oxygen evolution.[147] The results indicate that the higher the oxidation state of a surface site, the greater its ability for oxygen catalysis. Additionally, the increase of phase purity and decrease of crystallite size also enhance the activity. Further work led to catalyst materials of the general composition $La_{1-x}A_xCo_{1-y}B_yO_3$ (A = Ca; B = Mn, Fe, Co, Ni, Cu) synthesized by the different methods.[148–156] A strong composition dependence on catalyst performance was observed for both A and B-site doping. For example, Sr-substitution showed better performance at oxygen evolution, whereas, the Ca substituted material showed slightly better performance upon oxygen reduction. As an alternative catalyst of $La_{0.6}Ca_{0.4}CoO_3$, Zhu and Velraj demonstrated that $Sm_{0.5}Sr_{0.5}CoO_{3-\delta}$ also exhibited high bifunctional catalytic activity with long cycle lifetime.[157] At the same time, Sun *et al.* applied $Sr_{0.95}Ce_{0.05}CoO_{3-\delta}$ loaded with copper nanoparticles as a bifunctional catalyst for aqueous Li–air batteries. The high round-trip efficiency and excellent long-term stability were achieved due to the synergetic effect of perovskite oxide and copper.[158] Recently, a series of calcium–manganese oxides (Ca–Mn–O) were prepared through thermal decomposition of carbonate solid-solution precursors by Chen's group and investigated as electrocatalysts for the ORR. The catalytic properties of the series of Ca–Mn–O compounds were found to be closely correlated with the surface oxidation state of Mn and the crystallographic structures, which affects the extent of O_2 activation. Among the Ca–Mn–O compounds of perovskite-type $CaMnO_3$, layered structured $Ca_2Mn_3O_8$, post-spinel $CaMn_2O_4$ and $CaMn_3O_6$, the perovskite $CaMnO_3$ with open tunnels and multi-valences exhibited the highest activities, where the current density and electron transfer number were comparable to those of the benchmark Pt/C.[159]

Identifying a catalyst design principle that links the material properties to the catalytic activity can accelerate the search for highly active and abundant transition-metal-oxide catalysts.[160–162] Based on the molecular orbital principle, Suntivich *et al.* demonstrated that the ORR activity for perovskite oxide catalysts primarily correlates to σ*-orbital (e_g) occupation (e_g-filling having a value of ~1 for maximum activity) and the extent of B-site transition-metal–oxygen covalency (Fig. 9), which serves as a secondary activity descriptor.[39] The rate-limiting O_2^{2-}/OH^- exchange and the regeneration of OH^- on the surface depend on the energy gained by transferring a single σ*-antibonding e_g electron of the B–OH^- bond to the O_2^{2-} adsorbates, thereby stabilizing the displacement. Based on these findings, the intrinsic ORR activity of perovskite oxides exhibits a volcano trend as a function of the e_g-filling of B ions. It is interesting to note that oxides such as $LaMnO_{3+\delta}$ and $LaNiO_3$ have intrinsic ORR activity comparable to state-of-the-art Pt/C.[39,163]

Soon after, the same group reported a distinct OER activity design principle established by systematic examination of more than 10 transition metal oxides.[164] The results showed that the intrinsic OER activity also exhibits a volcano-shaped dependence on the occupancy of the 3d electron with an e_g symmetry of the surface transition metal cations in an oxide and the peak OER activity was predicted to be at an e_g occupancy close to unity,

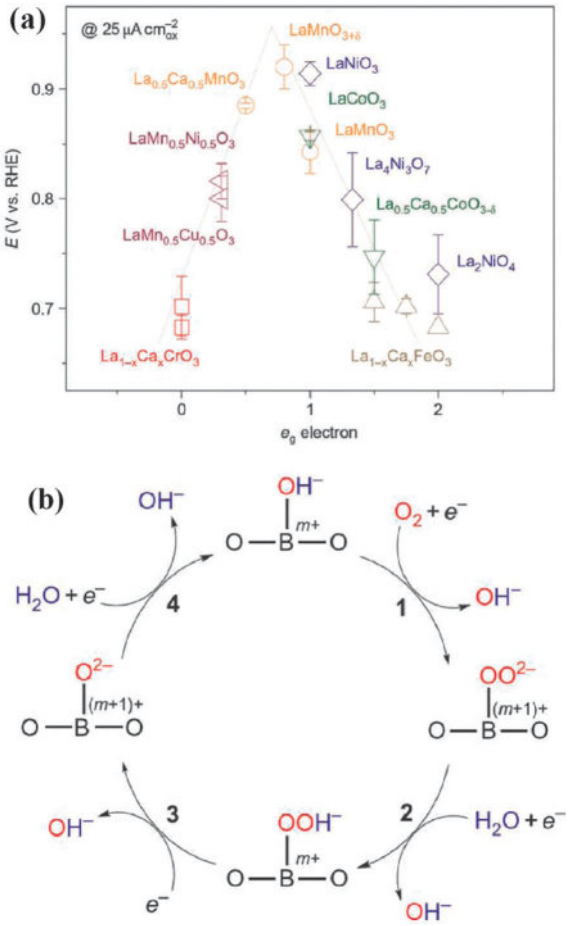

Fig. 9 (a) Volcano trend of ORR activity for perovskite-based oxides. (b) The proposed ORR mechanism on perovskite oxide catalysts. Reprinted with permission from ref. 39. Copyright 2011, Nature Publishing Group.

with high covalency of the transition metal–oxygen bonds. The high activity of $Ba_{0.5}Sr_{0.5}Co_{0.8}Fe_{0.2}O_{3-\delta}$ was predicted from the design principle and, experimentally, the OER activity is really at least an order of magnitude higher than that of the state-of-the-art iridium oxide catalyst in alkaline media. The two works provide a promising strategy for the development of highly active non-precious-metal-containing oxide catalysts for oxygen reduction by tuning the surface electronic structure features such as transition-metal e_g-filling and covalence.

For the type of perovskite, there is also a subclass of perovskite oxides with the general formula $A_2BB'O_6$ for the oxygen electrocatalysts, known as "double perovskites", where A is an alkaline-earth atom such as (Sr, Ba or Ca), and B and B′ are transition metal atoms. In the ideal crystal structure of these transition-metal oxides, there is a regular arrangement of corner-sharing BO_6 and $B'O_6$ octahedra. The properties of such perovskites as electrocatalysts are generally determined by the nature, oxidation states and relative arrangement of the B-site cations.[165,166] In a recent study, Cheriti and Kahoul investigated two double perovskite oxides, Sr_2CoMoO_6 and Sr_2FeMoO_6, supported on carbon Vulcan XC-72 and found that the former electrocatalyst exhibited a relatively higher activity for ORR than the latter.[166]

More recently, Takeguchi *et al.* reported that Ruddlesden–Popper-type layered perovskite, RP-$LaSr_3Fe_3O_{10}$ (n = 3), could function as a reversible air electrode catalyst for both the ORR and OER at an equilibrium potential of 1.23 V with almost no overpotentials.[167]

The catalytic properties of perovskite oxides have been demonstrated in Li–O_2 batteries with nonaqueous aprotic electrolytes. $La_{0.8}Sr_{0.2}MnO_3$ was firstly used by Bruce but the efficiency was not desirable.[116] Later, Yu *et al.* applied it and enhanced the capacity of the batteries.[168] Recently, Lee *et al.* reported that layered perovskite $La_{1.7}Ca_{0.3}Ni_{0.75}Cu_{0.25}O_4$ promoted the electrochemical oxidation of Li_2O_2 in a nonaqueous aprotic electrolyte.[169] The charging experiments with Li_2O_2-packed electrodes showed that the layered perovskite-containing electrode exhibits a charge potential decreased overpotential up to 400 mV compared to the catalyst-free electrode, indicating that the interlayer characteristics play a critical role in promoting the oxygen evolution. Nanostructures are always an important influencing factor for catalytic performance. For example, Mai *et al.* demonstrated that hierarchical mesoporous perovskite $La_{0.5}Sr_{0.5}CoO_{2.91}$ nanowires were high-performance catalysts for the ORR with low peak-up potential and a high limiting diffusion current.[170] The Li–air batteries based on such nanowires exhibited a high capacity, over 11 000 mA h g^{-1}, which is one order of magnitude higher than that of $La_{0.5}Sr_{0.5}CoO_{2.91}$ nanoparticles. The high specific surface area and mesoporous structure facilitate Li^+ diffusion and the formation rate of LiO_2 and Li_2O_2. More recently, our group prepared perovskite-based porous $La_{0.75}Sr_{0.25}MnO_3$ nanotubes (PNT–LSM) by combining the electrospinning technique with a heating method, as shown in Fig. 10.[171] With this novel electrocatalyst, the Li–O_2 batteries showed good roundtrip efficiencies, rate capabilities, and cycle stabilities. The charge voltage of the Li–O_2 cells with PNT–LSM/KB was found to be much lower than that of KB, by about 200 mV. Moreover, the Li–O_2 cells exhibited rather stable specific capacities above 9000–11 000 mA h g^{-1} for five cycles with the coulombic efficiency of around 100% (Fig. 10g) and could maintain 124 cycles with a capacity limit of 1000 mA h g^{-1}. The improved performance could be attributed to the synergistic effect of the high ORR and OER catalytic activity and the unique porous hollow structure of the PNT–LSM. The porous tubular structure could offer more abundant oxygen and electrolyte transportation paths in the electrode, facilitating the formation and decomposition of the discharge product and thus improving the reversibility of the O_2 electrode.

3.1.2.3 Pyrochlore-type oxides. Pyrochlore-type oxides have the general formula $A_2B_2O_6O'_{1-\delta}$, where A is Pb or Bi and B is Ru or Ir. The structure of pyrochlores can be viewed as a composite of two interwoven substructures, where corner-shared metal–oxygen octahedra (BO_6) generate a cage-like B_2O_6 framework that provides a conduction path for the electrons, resulting in metallic characteristics, while the A element is linearly connected to form A–O′–A linkages with special oxygen atoms (O′) that create corner-shared $O'A_4$ tetrahedra.[172–175] A feature of pyrochlores is their highly flexible stoichiometry and structure. The special oxygen can be partially or completely absent, resulting in up to 7% oxygen

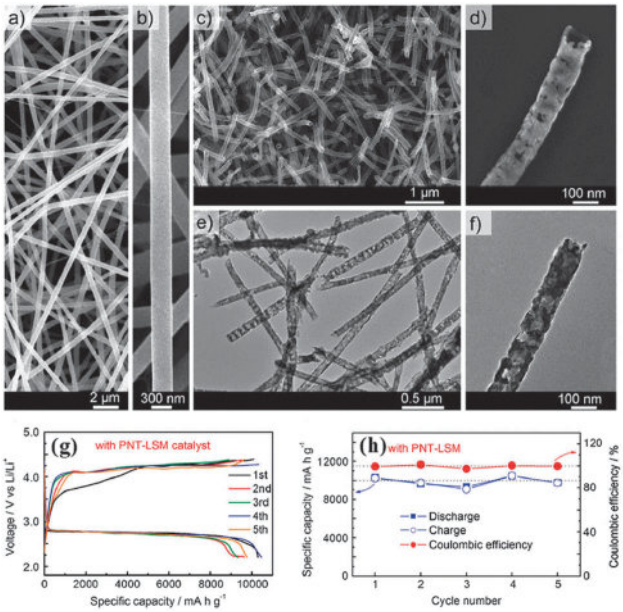

Fig. 10 SEM images at different magnifications. (a) and (b) As-electrospun composite fibers; (c) and (d) PNT–LSM after calcination at 650 °C for 3 h; (e) low- and (f) high-magnification TEM images of PNT–LSM. (g) and (h) Cyclic performance, discharge–charge specific capacity, and coulombic efficiency of Li–O_2 cells with and PNT–LSM catalyst at a current density of 0.025 mA cm^{-2}. Reprinted with permission from ref. 171, copyright 2013, Wiley-VCH.

vacancies in the lattice when δ = 0.5; or alternatively, the lattice can be filled with oxygen to give the composition $A_2B_2O_7$. For $Pb_2Ru_2O_{6.5}$, the single crystal conductivity is as high as 4.3 × 10^3 S cm^{-1} at 300 K.[170] The catalytic properties of pyrochlores can be adjusted by the choice and doping content of the A and B positions. For example, a portion of the noble metal in the B-site can be replaced by the A-site cation resulting in an expanded pyrochlore, $A_2[B_{2-x}A_x]O_{7-\delta}$ with x ranging from 0 to 1, which show good performances as bifunctional catalysts for ORR/OER in the strong alkaline media used in Zn–air cells.[77] The catalytic capability is believed to originate from the variable-valent characteristics of the B cations and the oxygen vacancies.[173]

Recently, Nazar's group developed a unique chemical approach to fabricate an expanded pyrochlore oxide with the composition of $Pb_2[Ru_{1.6}Pb_{0.44}]O_{6.5}$ into a novel metallic mesoporous framework using liquid-crystal templating and subsequent oxidation by a chemical agent (Fig. 11).[176] The high internal porosity led to a high surface area up to 155 m^2 g^{-1}, which increased the active sites. The prepared oxide showed promising catalytic activity with a lower charge potential for oxygen evolution and resulted in a cathode with a high reversible capacity of 10 000 mA h g^{-1} (~1000 mA h g^{-1} with respect to the total electrode weight including the peroxide product) in nonaqueous Li–O_2 batteries. The excellent properties could be ascribed to the high fraction of surface defect active sites in the metallic oxide, unique morphology and variable oxygen stoichiometry. This strategy, for creating porous metallic oxides, provides a promising way to new cathode architectures for Li–O_2 cells. Later, the same group synthesized nano-crystalline expanded pyrochlores

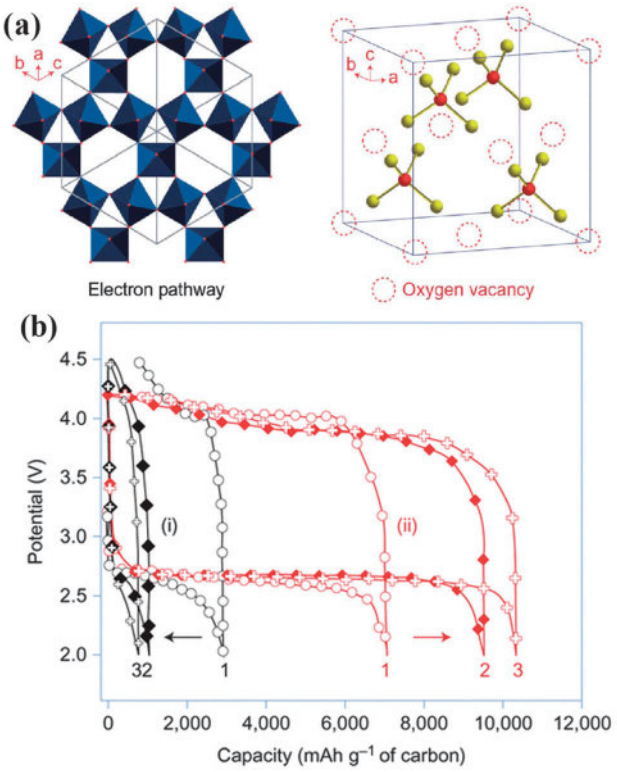

Fig. 11 (a) Structure of the defect pyrochlore $A_2B_2O_{7-\delta}$ (δ = 0.5; A = Pb, Bi; B = Ru) showing oxygen vacancies and electron conduction paths *via* BO_6 octahedra that create metallic conductivity. (b) Discharge–charge profiles of the first three cycles for carbon in $LiPF_6$–TEGDME (i, black) and mesoporous pyrochlore (ii, red), with cycle sweeps as indicated (current rate is 70 mA g^{-1} of carbon). Reprinted with permission from ref. 176, copyright 2012, Nature Publishing Group.

$Bi_2[Ru_{1.53}Bi_{0.47}]O_{7-\delta}$ (Bi/Ru = 1.61) and $Pb_2[Ru_{1.73}Pb_{0.27}]O_{6.5}$ (Pb/Ru = 1.31) by a chemical precipitation route in alkaline media.[177] High resolution TEM imaging confirmed the presence of 4–5 nm nanocrystallite domains which are coalesced into larger polycrystalline agglomerates. The high concentration of surface active sites, intrinsically variable oxidation states and good electron transport led to promising electrocatalytic properties for oxygen evolution in Li–O_2 cells, yielding rechargeable discharge capacities over 10 000 mA h g^{-1} and significantly lowered anodic overpotentials. It was noted that the amount of catalyst necessary for oxygen evolution performance is only 5 wt% by supporting on carbon. Interestingly, the discharge capacity of the Li–O_2 cell is increased further when combining pyrochlore oxide with a small amount of gold due to the increase in ORR activity.

3.2 Functional carbon materials

3.2.1 Nanostructured carbon. Pristine carbon materials usually show low catalytic activity for the ORR/OER in aqueous solutions. In contrast, as discussed in Section 2.2, carbon can provide enough catalytic activity for the oxygen reactions in nonaqueous electrolytes. So the applications of nanostructured carbon as the catalyst are mainly for the nonaqueous Li–air batteries. In this case, carbons serve as not only the catalyst support, but also as good ORR catalysts. The peculiar carbon nanostructures include one-dimensional (1D) nanotubes and nanofibers, 2D graphite and graphene nanosheets, and 3D nanoporous architectures.

In nonaqueous Li–air cells, the pore structures and the architecture of the air electrode are critical for the performance due to the insoluble discharged products of Li_2O_2, which accumulate at the active sites of the air electrode, potentially clogging the pores and thus increasing the resistance to gas transport through the pores. Accordingly, significant efforts have been devoted to optimize the microstructure of the air electrode for nonaqueous Li–air batteries. Early studies focused on the application of traditional porous carbon materials in Li–air batteries and some influencing factors were investigated.[178–184] For example, Hall and Mirzaeian reported that the cell performance depended on the morphology of the carbon, and that a combined effect of the pore volume, pore size and surface area of the carbon affected the storage capacity.[178] The authors found that the Li–O_2 cell using carbon, with a large pore volume and wide pore size, showed a high specific capacity. Yang *et al.* also demonstrated that large pore volumes and large mesoporous (with pore size of 2–50 nm) structures were crucial for the cell's performance.[179] Tran *et al.* found an almost linear relationship between the average pore diameter of the carbon catalysts and the capacity of Li–air cell.[181] Small pores, like micropores (with pore size <2 nm), played only a small role in the capacities. Including the pore structures, the modification of the carbon surface with hydrophobic molecules could also improve the performance by preventing the accumulation of Li_2O_2 on the surface of catalysts during discharge.[183]

Graphene, as a novel one-atom-thick two-dimensional carbon material, has attracted much attention for a wide range of applications due to its intrinsically superior electrical conductivity, excellent mechanical flexibility, remarkable thermal conductivity, and high surface area.[184–186] Graphene is usually prepared by a chemical method that readily produces exfoliated graphene sheets from graphite on a large-scale. The products have many edge sites and defect sites located on the surface and can act as catalysts to facilitate some chemical transformations.[187] To investigate the catalytic activity of graphene for the ORR, Li *et al.* firstly applied graphene nanosheets (GNSs) in an air electrode for nonaqueous Li–air batteries.[188] The air electrode based on GNSs delivered a high discharge capacity (8700 mA h g^{-1}) in comparison to carbon powders (1900 mA h g^{-1} for BP-2000 and 1050 mA h g^{-1} for Vulcan XC-72). Although the dominant discharge product was Li_2CO_3 and a small amount of Li_2O_2, this result indicated that the unique morphology and structure of GNSs were advantageous for Li–air batteries. At the same time, Sun *et al.* also investigated the catalytic activity of graphene in nonaqueous Li–air batteries.[189] The graphene nanosheet electrodes exhibited a much better cycling stability and lower overpotential than that of the Vulcan XC-72 carbon, further demonstrating that graphene nanosheets were an efficient catalyst for Li–air batteries. As mentioned above, the porous structure is very important for the performance of nonaqueous Li–air batteries. Based on this insight, Xiao *et al.* fabricated a novel air electrode consisting of hierarchically porous graphene.[190]

Graphene sheets that contains lattice defects and functional groups were constructed into the hierarchically porous structure by a colloidal microemulsion approach. An air electrode with this unique graphene sheets delivered an extremely high capacity ($\sim$15 000 mA h g^{-1}), which is attributed to the unique hierarchical structure consisting of microporous channels facilitating rapid O_2 diffusion and highly connected nanoscale pores for a high density of reactive sites. DFT calculations also revealed that the defects and functional groups on graphene favor the formation of isolated nanosized Li_2O_2 particles and help prevent air blocking in the air electrode.

The design of electrode structures is of great importance for improving energy transformation processes.[191–193] The previous studies are focused on the pore structure of carbon particles themselves, while the effect of their arrangement in the cathode on the performance of Li–O_2 battery is considerably ignored. Generally, the porous carbon particles are closely aggregated by a binder in the cathode and such tight aggregation unavoidably results in a low O_2 diffusion rate and limited space for Li_2O_2 deposition, which consequently makes the carbon particles have low utilization and further leads to the low-capacity and low-rate capability of the Li–O_2 battery. To solve this problem, our group proposed a novel strategy to maximize the utilization of porous carbon particles and the transport of reactants by constructing a free-standing hierarchically porous carbon (FHPC) derived from GO gel *via* a facile and effective *in situ* sol–gel method.[193] Fig. 12a shows the pristine nickel foam with macroporous skeletons. After the *in situ* synthesis, the porous carbon sheets were aligned roughly perpendicular to the skeleton surface (Fig. 12b), leaving large interconnected tunnels throughout the entire electrode depth. High-magnification observation (Fig. 12c and d) of the carbon sheets revealed that the sheets consisted of numerous small nanoscale pores. When employed as a cathode, the Li–O_2 battery simultaneously exhibited a high specific capacity and excellent rate capability. The capacity reached 11 060 mA h g^{-1} at a current density of 0.2 mA cm^{-2} (280 mA g^{-1}) and, unexpectedly, a high capacity of 2020 mA h g^{-1} could be obtained even when the current density increases ten-fold, up to 2 mA cm^{-2} (2.8 A g^{-1}) (Fig. 12e). In contrast, the capacity of the commercial KB carbon was 5180 mA h g^{-1} at a current density of 0.2 mA cm^{-2}, which is only half that of the FHPC electrode (Fig. 12f). This promising performance is attributed to the loose packing of carbon in the free-standing structure, which provides enough void volume for insoluble Li_2O_2 deposition and increases the efficient utilization of the carbon. Meanwhile, the hierarchically porous structure, including macropores from the nickel foam, and mesopores and micropores from the carbon particles, facilitates the O_2 diffusion, wetting of the electrolyte, and mass transport of all reactants.

Another new type of binder-free porous carbon electrode configuration was demonstrated by Shao-Horn's group by using a CVD method.[194] Vertically aligned arrays of hollow carbon fibers with diameters in the order of 30 nm were grown on a ceramic porous substrate, which were used as an air electrode in Li–air batteries. These all-carbon-fiber (binder-free) electrodes delivered gravimetric energy densities up to 2500 W h $kg_{discharged}^{-1}$ at power densities up to 100 W $kg_{discharged}^{-1}$, translating to an energy enhancement 4 times that of the state-of-the-art lithium intercalation compounds, such as $LiCoO_2$ (600 W h $kg_{electrode}^{-1}$). The good electrochemical performance was attributed to low carbon packing in the grown carbon-fiber electrodes and the highly efficient utilization of the available carbon mass and void volume for Li_2O_2 formation. Such a nanofiber structure allows for the clear visualization of Li_2O_2 formation and morphological evolution during discharge and its disappearance upon charge, which is a critical step toward understanding the key processes that limit the rate capability and result in the low round-trip efficiencies of Li–O_2 batteries. Recently, Kang *et al.* developed hierarchical porous electrodes comprising well-aligned CNTs fibrils.[195] The air electrode, with a controlled pore structure, was fabricated by orthogonally plying individual sheets of aligned multiwalled nanotubes without the use of any a binder or solvent, as shown in Fig. 13. The produced porous framework in these woven CNT electrodes enables the effective formation–decomposition of lithium peroxide by providing the facile accessibility of oxygen to the inner side of the air electrode and preventing the clogging of pores by the discharge product, even during the deep discharge. This unique feature led to the high cycle life and unprecedented high rate performance of the Li–O_2 cell. At 2 A g^{-1}, the battery can still maintain at least 60 cycles with a cut-off capacity of 1000 mA h g^{-1}. More interestingly, inspired by pencil-writing, Zhou and Wang reported another peculiar electrode by pencil-drawing on a ceramic state electrolyte.[196] The carbon nanosheets with a 2D structure

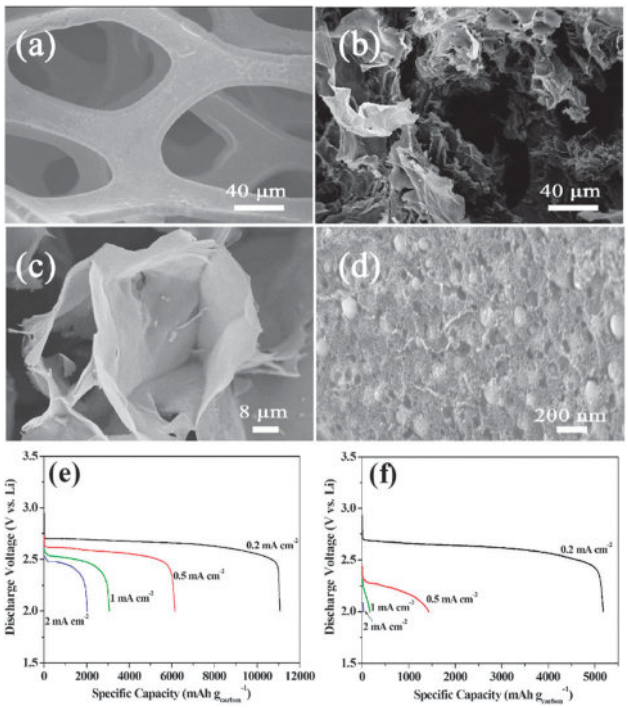

Fig. 12 SEM images of the pristine nickel foam (a) and different magnifications of the FHPC electrode (b–d). (e and f) Discharge curves at different current densities ranging from 0.2 mA cm^{-2} to 2 mA cm^{-2}: FHPC electrode (e) and commercial KB carbon electrode (f). Reprinted with permission from ref. 193, copyright 2012, Wiley-VCH.

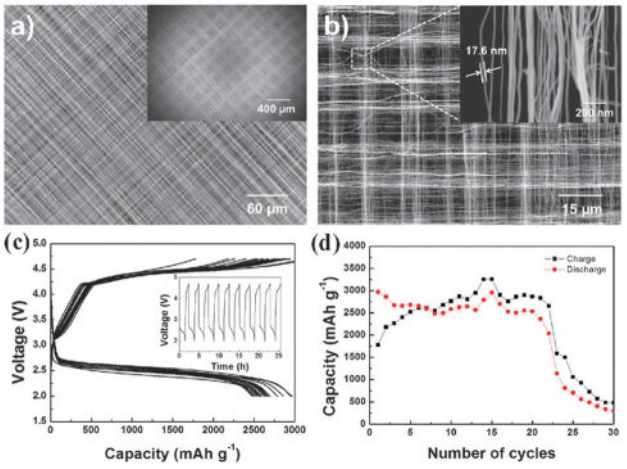

Fig. 13 SEM images of the CNT fibril at (a) low magnification (inset: large area image of the air electrode), and (b) high magnification. Discharge–charge profiles (c) and cyclabilities (d) of the Li–O_2 cells based on the air electrode of the woven CNT. Reprinted with permission from ref. 195, copyright 2013, Wiley-VCH.

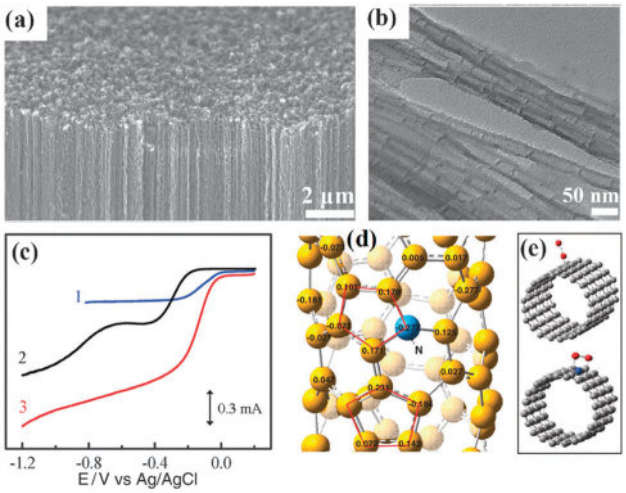

Fig. 14 (a) SEM image of the as-synthesized VA-NCNTs on a quartz substrate. (b) TEM image of the electrochemically purified VA-NCNTs. (c) RRDE voltammograms for oxygen reduction in air saturated 0.1 M KOH at the Pt–C/GC (curve 1), CNTs/GC (curve 2), and VA-NCNTs (curve 3) electrodes. (d) Calculated charge density distribution for the NCNTs. (e) Schematic representations of possible adsorption modes of an oxygen molecule at the CCNTs (top) and NCNTs (bottom). The C atoms around the pyrrolic-like nitrogen could possess much higher positive charges than do the C atoms around the pyridinic-like nitrogen. Reprinted with permission from ref. 201, copyright 2009, American Association for the Advancement of Science.

can be attached to the surface of a ceramic-state electrolyte by pencil-drawing and was directly used as the air electrode. A discharge capacity of 950 mA h g^{-1} was reached at the end voltage of 2.0 V with a current density of 0.1 A g^{-1}. Over 15 cycles, the capacity loss of the Li–air battery is not very obvious.

3.2.2 Doped carbon. As mentioned above, pristine carbon materials usually show low catalytic activity in aqueous solutions, but the activity is not negligible.[197–199] After heteroatom (such as N, B, P, and S) doping, the enhanced catalysis activity of the carbon materials are widely illustrated for oxygen reduction in aqueous electrolyte. Doping heteroatoms increase the degree of defectiveness and edge plane sites in the graphitic carbon network, which induces the active sites for the ORR. The abundant carbon nanostructures and their doping with functionalities enable researchers to tailor the catalytic properties.[197–236] To develop metal-free carbon-based catalysts, several approaches were demonstrated to synthesize nitrogen-doped carbon materials. As a typical example, Dai's group demonstrated that vertically aligned nitrogen-containing carbon nanotubes (VA-NCNTs) can act as a metal-free electrode with a much better electrocatalytic activity, long-term operation stability, and tolerance to the crossover effect of CO poisoning than platinum for oxygen reduction in alkaline fuel cells (Fig. 14).[201] The improved electrocatalytic activity can be attributed to the changes of the electronic structure during doping of the carbon nanotubes. The incorporation of electron-accepting nitrogen atoms in the conjugated nanotube carbon plane may produce a relatively high positive charge density on the adjacent carbon atoms (Fig. 14d). This synergistic effect of nitrogen-doping and the vertically aligned structure provides a super ORR performance with a four-electron pathway. In order to further illustrate the mechanisms of ORR on N-doped CNTs, Jiang's group studied the effect of different N-containing functional groups on the catalytic activity of N-doped CNTs under electrochemical conditions based on DFT.[202] They found that ORR occurs at both graphite-like N groups (NG) and pyridine-like N groups (NP) *via* both four-electron and two-electron mechanisms. At the lower potential region, both mechanisms are simultaneously responsible for the NG and NP defect sites; while at higher potentials, the four-electron mechanism becomes dominant and the ORR at the NP defect sites is more energetically favorable than that at the NG defect sites. Due to the advantage of doping, much effort has been devoted to the promising doping of carbon catalysts. N-doped carbon nanotubes, graphene sheets, ordered mesoporous graphitic arrays, and carbon nanocages were prepared *via* various methods such as chemical vapor deposition, heat-treatment with ammonia, nanocasting technology and so on.[203–218] The N-doped carbons displayed better performances with high electrocatalytic activity and durability as a metal-free electrode catalyst for the oxygen reduction in alkaline media and were successfully applied in Zn–air batteries. For example, with N-doped CNTs as the air cathode catalyst, a cell power density of ~70 mW cm^{-2} was achieved with a catalyst loading of 0.2 mg cm^{-2} and an electrolyte of 6 M KOH.[219]

Besides nitrogen-doping, other elements such as B, P, and S for doped carbon materials can also enhance the catalytic activity of carbon materials for the ORR. Using chemical vapor deposition with benzene, triphenylborane (TPB), and ferrocene as precursors and catalyst, B-doped CNTs (BCNTs) were synthesized with a tunable boron content.[220] The electrocatalytic performances are improved progressively with increasing boron content, as reflected in the increased reduction current and the positively shifted onset and peak potentials. Theoretical calculations indicate that boron-doping enhances the O_2 chemisorption on BCNTs.

The electrocatalytic ability of BCNTs for the ORR stems from the electron accumulation in the vacant $2p_z$ orbital of the boron dopant from the π^* electrons of the conjugated system; thereafter, the transfer readily occurs to the chemisorbed O_2 molecules with boron as a bridge. The transferred charge weakens the O–O bonds and facilitates the ORR on BCNTs. Yu *et al.* synthesized novel P-doped ordered mesoporous carbons (POMC) by a simple metal-free nanocasting approach.[221] The resulting POMC, with a small amount of P-doping (less than 1.5 atom%), exhibited outstanding electrocatalytic activity, long-term stability, and excellent resistance to alcohol crossover effects for the ORR in alkaline media. The P-doping induces defects in the carbon framework and increases the electron delocalization due to the good electron donating properties of P, promoting active sites for the ORR. Huang *et al.* found that when graphene was doped with the elements which have a similar electronegativity to carbon, such as sulfur and selenium, they could also exhibit better catalytic activities than the commercial Pt/C in alkaline media.[222]

Recently, co-doping has been developed into a research direction to improve the activity of carbons. It was found that co-doped nanocarbons show higher electrocatalytic activities than the corresponding single-atom-doped counterparts, due to a synergistic co-doping effect. Dai's group developed several kinds of co-doped carbons, such as B,N-co-doped CNTs, P,N-co-doped CNTs, and B,N-co-doped graphene.[223–226] Vertically aligned carbon nanotubes containing both B and N atoms (VA-BCN) were prepared by pyrolysis of melamine diborate, a single-compound source of carbon, boron, and nitrogen. The resultant VA-BCN nanotube electrode exhibited better activity for the ORR in alkaline medium than its counterparts doped with boron or nitrogen alone.[223] Subsequently, the same group developed a facile approach for the mass production of B,N-co-doped (BCN) graphene with tunable doping levels as efficient ORR electrocatalysts, simply by the thermal annealing of GO in the presence of boric acid and ammonia.[224] The resultant BCN graphene samples were demonstrated to show ORR electrocatalytic activities that were even better than that of the commercial Pt/C catalyst. In good agreement with the experimental observations, the first principles calculations revealed that the doping level affects the energy bandgap, spin density, and charge density. BCN graphene, with a modest N- and B-doping level, was demonstrated to show the best ORR electrocatalytic activity, fuel selectivity, and long-term durability, along with excellent thermal stability and porosity. Qiao *et al.* also reported the design and one-step synthesis of mesoporous N and S dual-doped graphene (N–S–G), as illustrated in Fig. 15.[227] Commercial colloidal silica was used as the structural template. Melamine and benzyl disulfide were selected as the N and S precursors, respectively, and the doping process was carried out by heating the mixture. This novel material showed excellent catalytic activity, including a highly positive onset potential and a very high kinetic limiting current, which was comparable to the commercial Pt/C catalyst. The DFT calculations revealed the redistribution of the spin and charge densities brought about by the dual doping of S and N atoms, which leads to a large number of carbon atom active sites. Recently, Asefa *et al.*

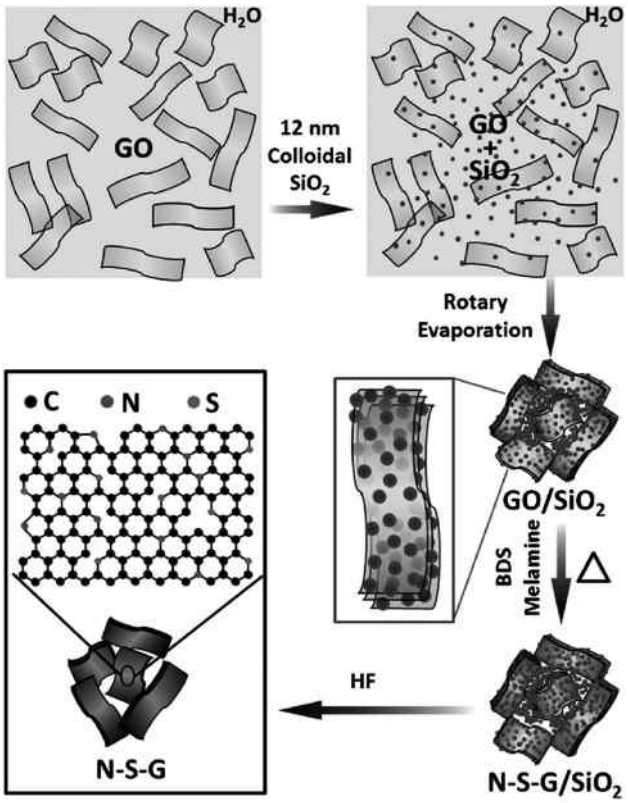

Fig. 15 Fabrication process of N and S dual-doped mesoporous graphene (N–S–G) nanosheets from graphene oxide. Reprinted with permission from ref. 227, copyright 2012, Wiley-VCH.

illustrated polyaniline-derived N and O dual-doped mesoporous carbons as efficient metal-free electrocatalysts synthesized from *in situ* polymerized mesoporous silica-supported polyaniline followed by carbonization and then etching away of the mesoporous silica template.[228] Except for binary doping, the ternary doping of carbon with B, P, N was also carried out to enhance the electrochemical oxygen reduction activity.[229] Due to the enhancement of the asymmetry atomic spin density, ternary doping showed better activity than the binary doping.

Despite tremendous progress in the synthesis of co-doped carbons, a fundamental issue has arisen about the distribution of heteroatoms in the doping process. A typical example is that when B and N coexist in sp^2 carbon, are B and N bonded together or located separately? These two cases correspond to totally different electronic structures, and therefore different conjugation effects within the carbon π system, which eventually leads to distinct ORR activities.[230] The experimental and theoretical results jointly indicate that the bonded case can produce by-products of hexagonal boron nitride (h-BN), which is chemically inert and results in the poor activity of the catalyst, while the separated case can greatly improves the ORR activity of the electrocatalysts, indicating the crucial role of the doping microstructure on the ORR performance. In order to avoid the formation of by-products, Qiao *et al.* developed a two-step doping strategy: firstly, N was incorporated by annealing with NH_3 at an intermediate temperature (*e.g.*, 500 °C), and

then B was introduced by pyrolysis of the intermediate material (N-graphene) with H_3BO_3 at a higher temperature (*e.g.*, 900 °C).[231] Through the newly developed sequential incorporation of the heteroatoms, there is no BN by-product observed. The resultant B,N-c-doped graphene exhibited a much improved electrochemical performance as compared to that of singly doped graphene and the hybrid electrodes synthesized in one step.

As expected, functionalized carbons by doping also provide advantages in the case of oxygen reduction in nonaqueous systems. Kichambare *et al.* reported that N-doped carbon, with a high surface area, was used as the cathode electrode in a solid-state Li–air battery.[237] The N-doped Ketjenblack–Calgon activated carbon cathode exhibited twice the discharge cell capacity of a cathode composed of only activated carbon without doping. Compared to pristine carbon, N-doped carbon further enhanced the discharge voltage. Later, Sun *et al.* demonstrated that N-doped CNTs exhibited a specific discharge capacity of 866 mA h g^{-1}, which was about 1.5 times that of CNTs with a specific discharge capacity of 590 mA h g^{-1}.[238] These results indicate the benefit of the doping functions in improving the capacity and oxygen reaction kinetics in Li–air batteries. Recently, Sun *et al.* also applied N-doped and S-doped graphene in nonaqueous Li–air batteries.[239,240] It was found that the discharge capacity dramatically increased resulting from the introduction of defective sites (defects or functional groups) after nitrogen-doping in graphene, while the S-doping could influence the morphology of the discharge product and therefore the charge property with significant differences from those of pristine graphene.[240] Fig. 16 schematically shows the growth mechanism of Li_2O_2 on S-doped graphene. Initially, O_2 is reduced to O_2^- and combined with Li^+ to form LiO_2. Then, elongated nanocrystallites of Li_2O_2 form on the carbon surface. Different morphologies are obtained depending on the discharge current density. In summary, the doping strategy is also effective for improving the performance of Li–air batteries, but the fundamental mechanisms require further investigation.

3.3 Metal oxide–nanocarbon hybrid materials

The inherent low conductivity and serious aggregation of nanoparticles in oxide catalysts are the important drawbacks that limit their activity for the ORR and OER. To overcome this limitation, the dispersion of the catalysts on a conductive substrate to form a composite is a common and useful strategy. As typical conducting substrates, different forms of carbons have been used for oxide catalysts. The design of an inorganic–nanocarbon hybrid simultaneously enhances the electrical conductivity and improves the distribution of active sites. The synergistic coupling effect between catalyst and substrate results in excellent catalytic performance.[241–244]

Recently, Cho *et al.* have devoted considerable efforts to improving the ORR activity of MnO_x by forming composites with nanocarbon in Zn–air batteries. Ketjenblack carbon (KB), carbon nanotubes (CNTs) and reduced graphene oxide (rGO) were selected as conductive substrates, on which the MnO_x nanostructure is deposited by different methods. For example, a composite air electrode consisting of KB carbon supported on amorphous manganese oxide (MnO_x) nanowires was synthesized *via* a simple polyol method (Fig. 17a).[245] The low-cost and highly conductive KB in this composite electrode overcomes the limitations due to the low electrical conductivity of MnO_x, while acting as a supporting matrix for the catalyst. The large surface area of the amorphous MnO_x nanowires, together with the high density of the surface defects, potentially provides more active sites for oxygen adsorption, thus, significantly enhancing the ORR activity. As a highly efficient catalyst, this composite air electrode exhibits a peak power density of ~190 mW cm^{-2} in a practical Zn–air battery, which is far superior to those based on a commercial air cathode with Mn_3O_4 catalysts and was similar to the performance of a Pt catalyst (Fig. 17b–d). A MnO_x–CNTs composite electrode was also prepared by a facile electroless deposition method. Spontaneous electroless deposition results in a good distribution and a well-bonded attachment of MnO_x on the surface of CNTs. A high peak power density (~180 mW cm^{-2}) was achieved for the Zn–air cell with the

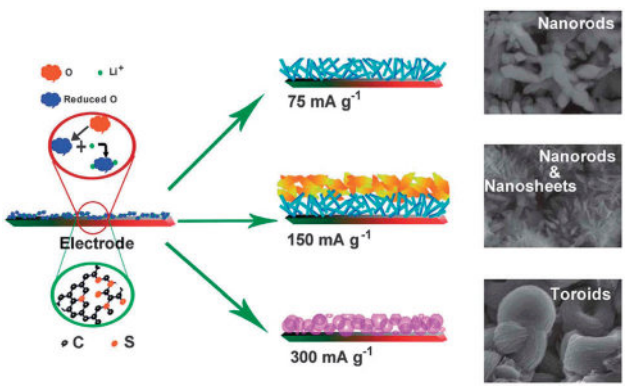

Fig. 16 Schematic of the growth of discharge product nanostructures on S-doped graphene electrodes. Reprinted with permission from ref. 240, copyright 2012, Royal Society of Chemistry.

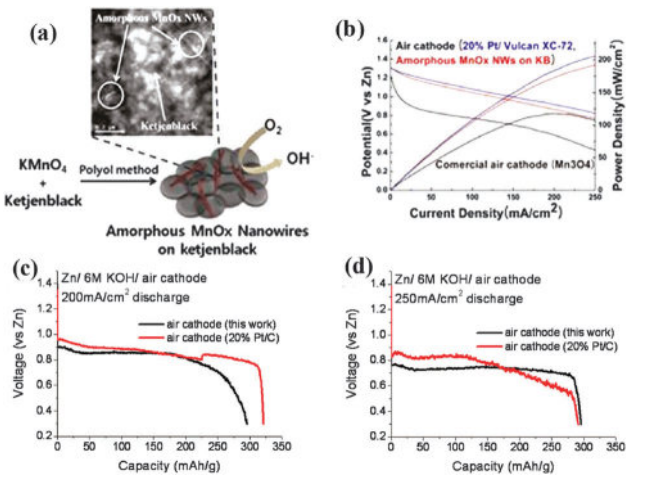

Fig. 17 (a) Schematic description of amorphous MnO_x nanowires on the Ketjenblack composite (α-MnO_x NWs on KB). (b) Polarization and (c and d) discharge curves at 200 and 250 mA cm^{-2}, respectively, of Zn–air full cells with different air electrodes: amorphous MnO_x nanowires on Ketjenblack composites and 20% Pt on Vulcan XC-72 (E-tek). A commercial air electrode (Meet) was used for comparison. Reprinted with permission from ref. 245. Copyright 2011, American Chemical Society.

composite cathode, which was comparable to the Pt catalyst ($\sim$200 mW cm^{-2}).[29] The well-bounded interface between MnO_x and CNTs for facilitating electron transfer from electrode to active sites and the birnessite crystalline structure with coexistence of Mn^{4+} and Mn^{3+} species on the surface of MnO_x particles were supposed to deliver the high catalytic activity toward the ORR. For the application of graphene, Cho *et al.* introduced an ionic liquid moiety to the reduced graphene oxide (rGO) nanosheets to increase the interaction between the graphene sheets and MnO_x nanoparticles.[246] By a facile solution-based growth method, manganese oxide (Mn_3O_4) was anchored on ionic liquid (IL)-modified reduced graphene oxide (rGO–IL) nanosheets. Based on the Koutecky–Levich plot, it was found that the ORR pathway of the hybrid rGO–IL–Mn_3O_4 composites is tunable with the relative amount of Mn_3O_4 nanoparticles supported on the graphene sheets; for example, the overloading of manganese oxide nanoparticles on this functionalized graphene sheet significantly hindered oxygen reduction and even changed the reaction mechanism from a direct four-electron pathway to an indirect two-electron pathway.

Strongly coupled inorganic–nanocarbon hybrid materials (SC-hybrids) have been gradually developed into novel catalyst materials by Dai's group.[247–252] The hybrid materials were synthesized by the direct nucleation, growth, and anchoring of inorganic nanomaterials on the functional groups of oxidized nanocarbon substrates, including graphene and carbon nanotubes. This approach affords the strong chemical attachment and electrical coupling between the electrocatalytic nanoparticles and nanocarbon, leading to nonprecious metal-based electrocatalysts with improved activity and durability for the ORR and OER. Compared to electrode materials based on physical mixtures of inorganics and nanocarbons, the SC-hybrids exhibited either a higher capacity, enhanced rate capability, higher catalytic activity, and/or improved cycling stability, leading to high performance batteries, supercapacitors, fuel cells, and water splitting electrocatalysts, and other types of energy storage and conversion materials.[5]

A represent hybrid material synthesized by Dai's group is the high-performance bi-functional catalyst Co_3O_4–N-rmGO (N-doped reduced mildly oxides graphene, Fig. 18a).[249] Usually, Co_3O_4 or graphene oxide alone has little catalytic activity, but their hybrid exhibits an unexpectedly high ORR activity that is further enhanced by the nitrogen-doping of graphene. The Co_3O_4–N-doped graphene hybrid exhibits similar catalytic activity, but superior stability compared to Pt in alkaline solutions. The same hybrid is also highly active for the OER, making it a high-performance non-precious metal-based bi-catalyst for both the ORR and OER (shown in Fig. 18c). The X-ray absorption near-edge structure (XANES) measurements were performed to determine the interactions between Co_3O_4 and GO in the hybrids. Compared to N-rmGO, the Co_3O_4–N-rmGO hybrid showed a clear increase of the carbon K-edge peak intensity at $\sim$288 eV, corresponding to carbon atoms in graphene being attached to oxygen or other species (Fig. 18d). This implied the existence of interfacial Co–O–C and Co–N–C bonds in the Co_3O_4–N-rmGO, which affected the electronic structure of Co_3O_4. Bond formation

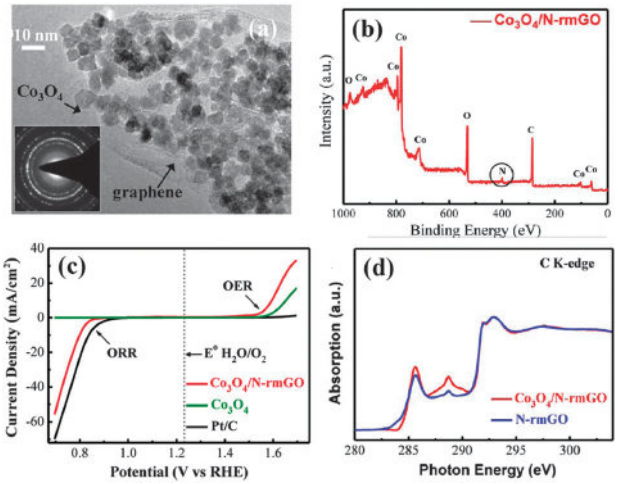

Fig. 18 (a) TEM images of the Co_3O_4–N-rmGO hybrid. The electron diffraction pattern of the Co_3O_4 nanocrystals on graphene is showed in the inset. (b) XPS spectrum of the Co_3O_4–N-rmGO hybrid. (c) Oxygen electrode activities within the ORR and OER potential window of the Co_3O_4–N-rmGO hybrid, Co_3O_4 nanocrystal, and Pt/C catalysts dispersed on carbon fiber paper in O_2-saturated 0.1 M KOH. (d) C K-edge XANES of the Co_3O_4–N-rmGO hybrid and N-rmGO. Reprinted with permission from ref. 249, copyright 2012, Nature Publishing Group.

between Co_3O_4 and N-rmGO and changes in the chemical bonding environment for C, O and Co atoms in the hybrid material resulted in the synergistic effect between catalyst and substrate. N-doping of GO could afford stronger coupling between Co and graphene in Co_3O_4–N-rmGO than in Co_3O_4–rmGO. N-groups on reduced GO serve as favourable nucleation and anchoring sites for Co_3O_4 nanocrystals, owing to coordination with Co cations. The oxidation degree of graphene oxide greatly influences the performance of the hybrids.[5] Traditional harsh oxidation of GO usually causes the imbalance of the inorganic–carbon coupling interactions and the electrical conductivity of the hybrid material. It is crucial for high ORR and OER performance to control a moderate degree of graphene oxidation to simultaneously afford sufficient functional groups and electrical conductivity.

Besides graphene, CNTs have also been used for the synthesis of SC-hybrids by Dai's group. Co_3O_4 or CoO–N-doped CNT hybrids were prepared using mild oxide CNTs.[250] Interestingly, the metal oxide–carbon nanotube hybrids were found to be advantageous over the graphene counterparts, showing higher ORR current density at medium overpotentials through a 4e reduction pathway. The Nyquist plots of the electrochemical impedance data indicated that the Co_3O_4–NCNT hybrid exhibited a smaller charge-transfer resistance for the ORR with a smaller semicircle for the Co_3O_4–NCNT hybrid than the N-rmGO hybrid at the ORR operation potential of 0.8 V. Direct electrical resistance measurement on the sample pellet showed that the Co_3O_4–NCNT hybrid had a smaller resistance ($\sim$40–60 Ω) than the Co_3O_4–N-rmGO hybrid ($\sim$200–300 Ω). These results suggested that higher electrical conductivity in the NCNT hybrid could be reached, which is of particular importance for the electrochemical characteristics of the hybrids. Of course, GO has its own advantage in providing higher surface areas for constructing hybrid materials.

To further enhance the hybrid catalyst, Dai's group developed a mixed-metal oxide $MnCo_2O_4$–N-doped graphene hybrid material for highly efficient ORR electrocatalysis under alkaline conditions.[251] By controlling the reaction ratio of $Co(OAc)_2$ and $Mn(OAc)_2$ as 2 : 1, $MnCo_2O_4$ in the cubic spinel phase grew on the graphene sheets to form a strongly coupled $MnCo_2O_4$–N-rmGO hybrid. At the same mass loading, the $MnCo_2O_4$–N-graphene hybrid can outperform Pt/C ORR current density at medium overpotentials with a stability superior to Pt/C in alkaline solutions. At a constant voltage of 0.70 V *vs.* RHE, the ORR current density produced in the hybrid catalyst decreased by only 3.5% over 20 000 s of continuous operation, while the corresponding physical mixture sample and Pt/C catalysts exhibited ~25% and 33% decreases in the current density, respectively. The nucleation and growth method results in covalent coupling with the formation of C–O–metal and C–N–metal bonds between N-doped graphene oxide and spinel oxide nanoparticles, affording a much higher activity and stronger durability than the physical mixture of nanoparticles and N-rmGO. Mn substitution increased the activity of the catalytic sites of the hybrid materials, further boosting the ORR activity compared with the pure Co_3O_4–N-rmGO hybrid.

The rational design of the structure in the hybrid materials is also crucial for oxygen electrocatalysis activity. Recently, Feng *et al.* developed three-dimensional N-doped graphene aerogel (N-GA)-supported Fe_3O_4 nanoparticles (Fe_3O_4/N-GAs) as efficient cathode catalysts for the ORR in alkaline media. The graphene hybrids exhibit an interconnected macroporous framework of graphene sheets with uniform dispersions of the Fe_3O_4 nanoparticles.[253] For the ORR, Fe_3O_4/N-GAs show a more positive onset potential, higher cathodic density, lower H_2O_2 yield, and higher electron transfer number than Fe_3O_4 particles supported on N-doped carbon black or N-doped graphene sheets, highlighting the importance of the 3D macropores and the high specific surface area of the GA support for improving the ORR performance. Chen and co-workers designed another new class of core–corona structured bifunctional catalyst (CCBC) consisting of lanthanum nickelate centers supporting nitrogen-doped carbon nanotubes (NCNT) for rechargeable metal–air batteries.[254] The nanostructured hybrid is based upon a highly ORR-active nitrogen-doped carbon nanotube (NCNTs) corona component and a highly OER-active lanthanum nickelate ($LaNiO_3$) derived core component (Fig. 19). In the structure, the NCNTs are highly graphitic, resulting in robust operational durability, and possess exemplary electronic conductivity. As a result, the CCBC coated air electrode exhibited outstanding cycling performance without degradation after 75 cycles in Zn–air batteries. Combining $LaNiO_3$ and NCNT into one entity in the CCBC increased the catalyst activity and durability as a result of the synergistic effects between the strong-connected NCNT and core material. The CCBC represented a novel class of bifunctional catalyst material that is very applicable to future generation rechargeable metal–air batteries.

Motivated by the high ORR activity and good OER activity of the $MnCo_2O_4$–N-rmGO hybrid in aqueous solution, Dai's group explored the material as a cathode catalyst for a nonaqueous Li–O_2 battery.[255] The authors found that the ORR catalytic activity of the $MnCo_2O_4$–N-rmGO hybrid in aqueous solutions could be translated to the organic electrolyte, giving a high discharging potential of the Li–O_2 cell and simultaneously decreasing the charging voltage, compared to N-doped graphene (N-rmGO), carbon black (CB), and a mixture of $MnCo_2O_4$ nanoparticles and CB. The overpotential and charging–discharging performance of $MnCo_2O_4$–N-rmGO hybrid was similar to that of the benchmark Pt/C catalyst. Moreover, the hybrid catalyst exhibited much better cycling stability of the Li–O_2 cell than Pt/C through charge and discharges with a capacity cutoff of 1000 mA h g^{-1} over 40 cycles, with little change in the discharging and charging potentials. Although side reactions could possibly be involved in the carbonate electrolyte, the substantial performance improvement in the hybrid material over the physical mixture of $MnCo_2O_4$ and graphene suggested that the strong coupling within the hybrid structure played an important role in the effective and rapid transfer charges, even in organic electrolytes.

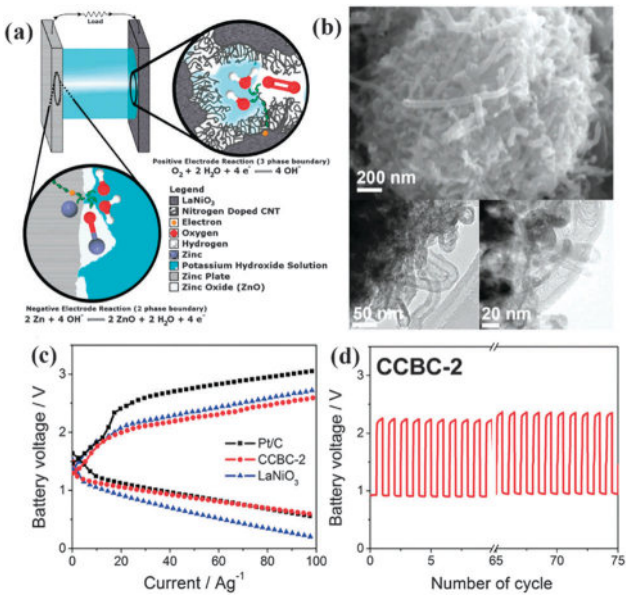

Fig. 19 (a) Schematic of the Zn–air battery and the reactions taking place on the electrodes. The CCBC catalyst is applied on the positive electrode which catalyzes the ORR and OER reactions. (b) Scanning electron micrograph and transmission electron micrograph of the CCBC illustrating the NCNT on the surface of the core particle. Zn–air battery performance: (c) discharge and charge polarization curves of Pt/C, CCBC-2, and $LaNiO_3$ and (d) cycling of CCBC-2. One discharge and charge is referred to as one cycle, and the battery was cycled 75 times. Reprinted with permission from ref. 254. Copyright 2012, American Chemical Society.

Cao *et al.* further illustrated the synergistic catalytic effect of oxide and carbon in the α-MnO_2 nanorod–graphene hybrid in nonaqueous Li–O_2 batteries through the *in situ* nucleation and growth of α-MnO_2 nanorods on graphene nanosheets (GN) (Fig. 20a and b).[256] As shown in Fig. 20c, the α-MnO_2–GN hybrid showed excellent catalytic activity for both ORR and OER processes. It delivered a high reversible capacity of 11 520 mA h g_{carbon}^{-1} at a current density of 200 mA g_{carbon}^{-1} (0.06 mA cm^{-2}). In contrast, the α-MnO_2 and GN mixture could only deliver a reversible capacity of 7200 mA h g_{carbon}^{-1}, which is about 62.5%

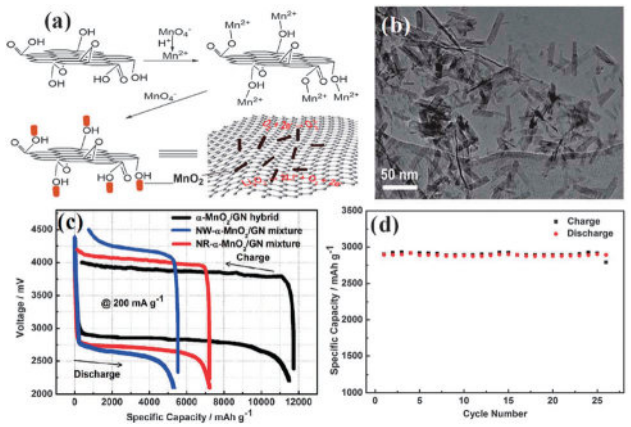

Fig. 20 (a) Schematic drawing of the growth of α-MnO_2 nanorods on graphene and the schematic structure of the α-MnO_2–graphene hybrid. (b) TEM image of the hybrid. (c) Discharging and charging profiles of Li–O_2 batteries based on three different catalysts, α-MnO_2–graphene hybrid, NW(nanowire)-α-MnO_2–graphene mixture and NR(nanorod)-α-MnO_2–graphene mixture. The current density and capacities were based on the mass of graphene. (d) Cycle performance. Reprinted with permission from ref. 256, copyright 2012, Royal Society of Chemistry.

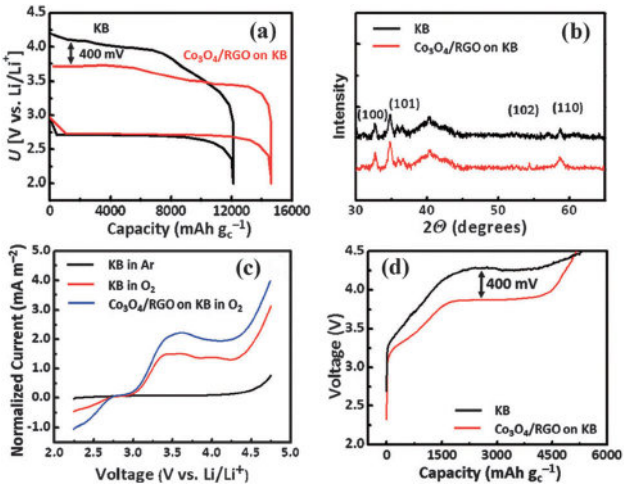

Fig. 21 (a) First discharge–charge profile for Li–O_2 cells with Ketjenblack (KB) or Co_3O_4/RGO/KB at 25 °C at a current rate of 140 mA g^{-1}. (b) XRD patterns of the cells in part (a) on the first discharge. The reflections of Li_2O_2 are marked. (c) Linear sweep voltammetry following a hold at 2.25 V for 1 h. (d) Voltage profile on charge for cells containing chemically deposited Li_2O_2 in the presence of either Co_3O_4/RGO/KB or KB. Reprinted with permission from ref. 82, copyright 2013, Wiley-VCH.

of the hybrid. The cell simultaneously showed good cycle performance over 25 cycles with stable reversible capacities and a discharging and charging voltage platform (Fig. 20d). Besides graphene, the MnO_x–CNTs or carbon nanofiber hybrids were also prepared as cathode catalysts in Li–O_2 batteries with reduced discharge–charge overpotentials and improved cycling properties.[257–264] Recently, Amine *et al.* synthesized porous carbon supported α-MnO_2 nanoparticles by a wet-chemistry approach at ambient temperature.[265] The advantage of this synthetic approach is that the porous structure and surface area of carbon can be well preserved after dispersion of MnO_2 onto the surface of the carbon support. As an electrocatalyst for rechargeable Li–O_2 cells, the as-prepared hybrid catalysts demonstrated good electrochemical behavior with a capacity of 1400 mA h g^{-1} (carbon + catalyst) at a current density of 100 mA g^{-1} (carbon + catalyst) during the initial discharge. Interestingly, the charge potential was significantly reduced, to 3.5–3.7 V, compared with most of the reported data, which are usually above 4.0 V.

Cobalt oxide–carbon hybrids have also been applied in nonaqueous systems. For example, Nazar's group showed that nanocrystalline Co_3O_4 grown on reduced graphene oxide (Co_3O_4/RGO) and employed as part of a carbon-based oxygen electrode membrane, results in the significant reduction of overpotentials for the OER (up to 350 mV, Fig. 21a), and improved cycling performance.[82] The synthesis of Co_3O_4/RGO was carried out by reduction of cobalt phthalocynanine deposited onto graphene, followed by mild oxidation. An interesting phenomenon was observed in the electrochemical test. The onset potential of the OER is similar for both Ketjenblack (KB) and Co_3O_4/RGO (just above 3.0 V), which is in sharp contrast to the OER in aqueous media, where Co_3O_4/graphene significantly lowered the onset potential (Fig. 21d). The overall results indicated that it acts as a promoter to enhance the surface transport of the Li_xO_2 species, by reducing their binding energy in both the forward and reverse electrochemical processes. However, the mechanisms of reaction still need to be analyzed by advanced technologies. At the same time, other cobalt oxide–carbon hybrids such as CoO/CMK-3 (mesoporous carbon) and Co_3O_4/CNTs catalysts were also synthesized and applied in nonaqueous systems.[266,267] The high capacity and low overvoltage indicate their promising catalytic activity.

3.4 Metal–nitrogen complex

One of the most promising non-precious metal electrocatalysts in fuel cell applications is carbon–supported transition metal/nitrogen (M–N_x/C) materials (M = Co, Fe, Ni, Mn, *etc.*, and normally x = 2 or 4), which have gained increasing attention due to their promising catalytic activity displayed towards the ORR, along with the utilization of abundant, low-cost precursor materials. According the synthesis process, the M–N_x/C catalysts can be classified into two categories: non-pyrolyzed catalysts with organic states and pyrolyzed catalysts with inorganic states. Non-pyrolyzed M–N_x/C catalyst materials maintain the well-defined structure of macrocycle complexes during simple synthesis procedures, providing favorable structural control for their activities. The pyrolyzed M–N_x/C catalysts are based on building blocks of non-pyrolzed M–N_x/C, through high-temperature treatment.

3.4.1 Non-pyrolyzed M–N_x/C materials. Since Jasinski's first report on the ORR catalytic activity of metal–N_4 (M–N_4) chelates as cobalt phthalocyanines (CoPc) in alkaline conditions,[268] transition metal porphyrins such as tetraphenyl porphyrins (TPP), tetramethoxy tetraphenyl porphyrins (TMPP), and phthalocyanines (Pc) have been thoroughly studied as attractive candidates for active and reliable catalysts for fuel cell cathodes, which opened a new direction for research in the field of ORR catalysis.[269–283] The well-defined structures of the

complexes allows for the direct correlation of the catalyst structure and the resulting ORR activity and stability. The activity of these complexes is directly related to the metal ion center and encompassing ligand structure. For example, cobalt-based complexes (*i.e.*, CoPc or Co porphyrin) exhibit a 2-electron process to produce H_2O_2 towards the reduction of oxygen, whereas Fe-based complexes show a 4-electron reduction process forming H_2O. As the proposed active site for the ORR, it was found that Fe and Co metal-ion centers display the optimal electrocatalytic properties, leading to the distinct redox properties in the macrocycle compounds. Various macrocycle structures possess significantly different chemical and electronic properties and the ORR activity is related to their ionization potentials and oxygen binding capabilities. From the theoretical and experimental results on FePc/C and CoPc/C catalysts, Wang *et al.* concluded that the lower the O_2 adsorption energy, the higher the kinetics of the ORR that can be expected.[276]

For the ligand structure, the presence of additional functional groups or substituents on the outer rings of the macrocycle compounds has been recognized to tailor the electrochemical properties and functionalities of these materials. It appears that the selectivity of metal macrocycles towards a chemical and/or electrochemical reaction is "set" by the metal centre, and the activity is then "tuned" by the peripheral substituents.[277] Chen's group indicated that functionalizing carbon supported FePc with thioether phenyl groups (Fe–SPc/C) with a structure inspired by naturally occurring ORR catalysts would lead to exemplary stability enhancements under potentiodynamic conditions in acidic electrolyte (Fig. 22).[279] Thioether functional groups are

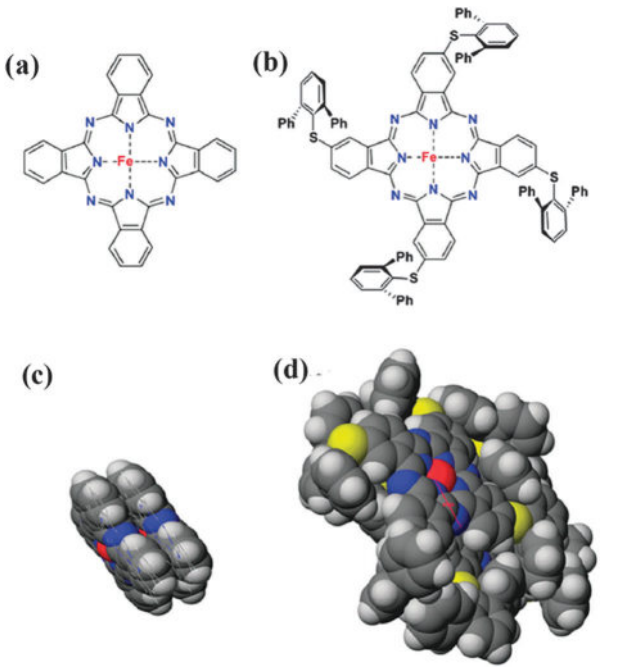

Fig. 22 Atomic structure of (a) Fe–Pc and (b) Fe–SPc and the space filling stacking model of (c) Fe–Pc (d_{Fe-Fe}: 4.119 Å) and (d) Fe–SPc (d_{Fe-Fe}: 6.945 Å); side view, same scale. Reprinted with permission from ref. 279. Copyright 2010, American Chemical Society.

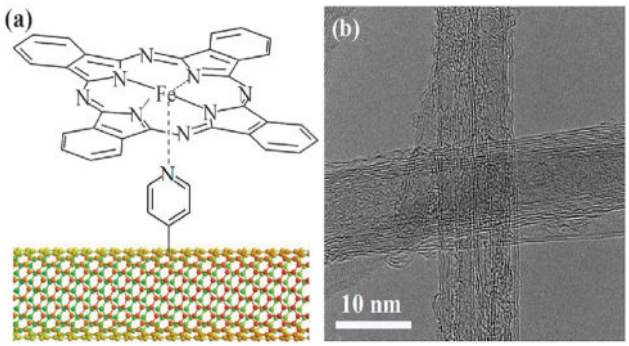

Fig. 23 (a) Schematic diagram of the structure of the FePc–Py–CNTs composite. (b) HR-TEM image of the FePc–Py–CNTs composite. Reprinted with permission from ref. 280, copyright 2013, Nature Publishing Group.

attached to phthalocyanine macrocycles to act as supplementary electron-providing sites to prevent issues arising from slow electron transfer. Meanwhile, bulky diphenyl thiophenol groups are incorporated into the structure providing a high degree of steric hindrance, maintaining the isolation of the catalytically active sites.

More interestingly, inspired by the active site in cytochrome *c* oxidase, Cho's group designed a five-coordinated structure using pyridine-functionalized carbon nanotubes (CNTs) to anchor FePc molecules and provide an axial ligand for the iron centre (Fig. 23).[280] The novel catalysts exhibited higher electrocatalytic activity for oxygen reduction than the state-of-the-art Pt/C catalyst, as well as exceptional durability during cycling in Zn–air batteries. The theoretical calculations suggested that the enhanced performance might originate from the electronic structure change of the Fe center in the five-coordinated structure, which induces the high stretching degree of the O–O bond in the FePc–Py–CNTs system and increases the binding energy between the oxygen species and catalyst. In addition, compared with the four-ligated Fe in the FePc–CNT system, the extra axial coordination bond between Fe and the Py group in the FePc–Py–CNT system reduces the probability of Fe ion dissociation and improves the durability. These results provide an indication that the careful design and modification of these complexes can improve the ORR activity and stability. Recent work further illustrated the importance of the rational structure design of macrocycle compounds. Tang *et al.* presented another novel strategy to incorporate the molecular architecture of the cobalt porphyrin multilayers onto reduced graphene oxide (rGO) sheets using the layer-by-layer (LBL) assembly technique.[283] Upon their combination, the planar benzene rings of the rGO sheets could provide possible electrostatic or coordination interactions, π–π stacking and van der Waals forces with the cobalt porphyrin catalysts. Such multiple interactions will favor the stability of the catalysts on the substrates. With respect to commercial C/Pt catalysts, the assembly of rGO/$(Co^{2+}$-THPP$)_n$ shows comparable electrocatalytic activity, but better stability and increased tolerance to the crossover effect.

3.4.2 Pyrolyzed M–N_x/C materials. Although the catalytic activity of various organic metal–N_4 complexes supported on carbon has been demonstrated in aqueous media, it was found

that the catalyst structures gradually decomposed in the presence of acid and poor stability resulted in a loss of catalytic activity.[284] A significant breakthrough was achieved when high temperature heat treatment procedures (400 to 1000 °C) were introduced to the catalyst synthesis process.[285] By this approach, the obtained inorganic M–N_x/C catalysts not only increased the concentration of available ORR active sites, but also improved the catalyst stability. Due to the decomposition of the macrocycle complexes, it was discovered that expensive transition metal macrocycle compounds were not actually required, and that catalytically active M–N_x/C moieties could be synthesized by the simple pyrolysis of transition metal, carbon and nitrogen containing precursor materials. This provided a new direction for research involving inexpensive precursor materials. In order to develop high-efficient M–N_x/C catalysts, systematic trial and error investigations have been carried out based on the optimization of the synthesis conditions, precursor materials and catalytic structures. Several factors were verified to be important for the activity and stability of the pyrolyzed M–N_x/C electrocatalysts, including transition metal type and loading, carbon support surface properties and nitrogen content, and heat treatment conditions and duration.[286–289] Recently, the distribution of metals in the carbon matrix has been found to be crucial for the stability of the catalysts. Several groups encapsulated Fe nanoparticles into the compartments of pea-pod like carbon nanotubes (CNTs).[290–292] This protection does not impede the activation of O_2 and the catalyst has a rather high activity and long-term stability. DFT calculations indicate that the catalytic activity could arise from the electron transfer from Fe particles to the CNTs leading to a decreased local work function on the carbon surface.[292] Electron transfer is very important in the catalytic activity of doped carbon materials.[293–296]

During the synthesis of such catalysts, typical metal types usually include inorganic salts and organometallic complexes. The introduction and distribution of surface nitrogen on the surface of the catalyst materials was initially deemed as the most critical step to determine the performance of the obtained materials. Different nitrogen sources usually reflect the features of synthesis. Nitrogen precursor materials are commonly classified into three categories, including: (i) gaseous precursors such as NH_3 or CH_3CN;[297] (ii) organic small molecules such as cyanamide, corrole, or ethylenediamine (EDA);[298–304] and (iii) nitrogen containing polymers such as polyaniline (PANI).[305–316] For the carbon support, the disordered carbon degree and microporosity are also influential factors.[317,318] A highly-efficient M–N_x/C catalyst is usually the result of the maximum optimization of every aspect. For example, Dodelet and co-workers reported in 2009 the best iron-based catalysts with ORR catalytic activities comparable to Pt, based on previous insights into the catalyst design.[299] Highly microporous Black Pearl 2000 was selected as the carbon support and planetary ball-milling was used to fill the support pores with pore filler (1,10-phenanthroline) and the iron precursor (ferrous acetate). The authors found that the greatest increase in site density was obtained when a mixture of carbon support, phenanthroline, and ferrous acetate was ball-milled and then pyrolyzed twice, first in argon, then in ammonia. The active sites of the microporous carbon-supported iron-based catalysts were believed to contain iron cations coordinated by pyridinic nitrogen functionalities in the interstices of graphitic sheets within the micropores. The outstanding ORR performance of the pyrolyzed FeCo–EDA catalyst was also observed and compared with the commercial Pt/C catalyst in the assembled Zn–air batteries.[300] The FeCo–EDA catalyst exhibited an almost three times higher mass activity compared to that of the commercial Pt/C catalyst after the accelerated degradation test and a higher peak power density (232 mW cm^{-2}), compared to the power density (196 mW cm^{-2}) for commercial Pt/C.

Nitrogen-containing polymers have gradually become important precursors in the synthesis of highly active M–N_x/C catalysts, which provide both carbon and nitrogen sources during high temperature pyrolysis. The use of such polymers as nitrogen precursors promises a more uniform distribution of nitrogen sites on the surface and an increase in the active-site density. The obtained catalyst materials display very promising ORR activity and stability, with results and electrocatalytic properties similar to the pyrolyzed macrocycle complex catalysts.[284] Wu *et al.* successfully used PANI as a precursor for a carbon–nitrogen template for the high-temperature synthesis of catalysts incorporating iron and cobalt.[312] PANI has a favorable combination of aromatic rings connected *via* nitrogen-containing groups. Because of the similarity between the structures of PANI and graphite, the heat treatment of PANI could facilitate the incorporation of nitrogen-containing active sites into the partially graphitized carbon matrix. Results from this study indicated that PANI-derived formulations combine high ORR activity with unique performance durability and 4e reduction selectivity. Hashimoto *et al.* applied network polymers to synthesize M–N_x/C catalysts. 2,6-Diaminopyridine was selected as a building-block monomer for the formation of a nitrogen-rich network polymer that forms self-supporting spherical backbone structures and contains a high density of metal-coordination sites.[313] The pyrolyzed Co/Fe-coordinating polymer exhibited a high specific oxygen reduction activity with onset potentials of 0.87 V *vs.* RHE in neutral media. Recently, Liu *et al.* described another approach for the preparation of highly active and support-free oxygen reduction catalysts using porous organic polymer precursors (polyporphyrin) containing densely populated nitrogen-coordinated iron macrocyclic centers uniformly decorated over the micropore surface.[316] Fig. 24 shows a simplified synthesis and the molecular and three dimensional stacking structures of the precursor. N-containing aromatic compounds provide chances for the synthesis of highly active M–N_x/C catalysts for the ORR. Metal–organic frameworks (MOFs), which represent a new frontier for materials research, are coordination polymers consisting of metal ions/clusters and organic linkers. As a subclass of MOFs, zeolitic imidazolate frameworks (ZIFs) have been demonstrated to be excellent precursors for non-precious electrocatalysts due to their structural features of uniformly distributed transition metals ligated by N-containing ligands.[319–322]

Mass transfer is also a limiting factor for the ORR performance, which becomes crucial especially in the practical cells. To dramatically enhance mass transfer through porous oxygen-breathing electrodes, Cho's group created some unique electrode

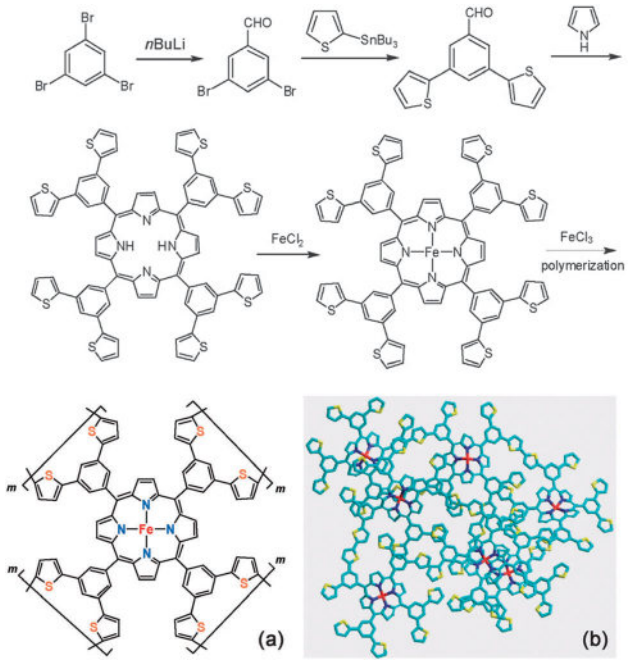

Fig. 24 Synthesis of porous organic polymer containing nitrogen-coordinated iron macrocyclic centers. (a) Molecular structure; (b) simulated 3D stacking of the precursor. Fe red, N blue, C light blue, S yellow; H has been omitted for clarity. Reprinted with permission from ref. 316, copyright 2013, Wiley-VCH.

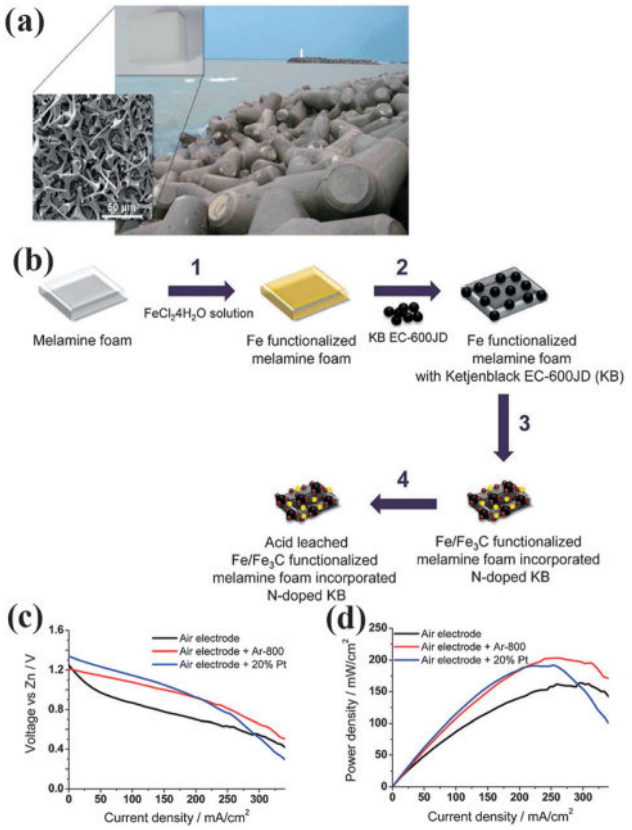

Fig. 25 (a) Architectural features of tetrapod structures, commercially available melamine foam (inset), and a cross-sectional view (SEM image) of a fractured melamine foam after pyrolysis. The interconnected large pores may facilitate fast mass transport. (b) The synthesis process of the Fe/Fe_3C functionalized melamine foam infiltrated with N-doped Ketjenblack (KB): (1) impregnation of melamine foam with $FeCl_2{\cdot}4H_2O$ solution; (2) infiltration of Ketjenblack EC-600 JD; (3) carbonization in an Ar atmosphere for 2 h at 800, 900, and 1000 °C; (4) leaching in a 2 M H_2SO_4 solution. (c) Current–voltage and (d) power–voltage curves of the Zn–air cells with Ar-800 and 20% Pt/C catalysts. A gas diffusion layer without any catalysts was used as the baseline air electrode for comparison. Reprinted with permission from ref. 315, copyright 2013, Wiley-VCH.

architectures inspired by breakwaters composed of highly porous tetrapod structures.[315] The synthesis process is shown in Fig. 25. Nanosized Ketjenblack clusters were successfully incorporated into commercially available melamine foam of a microscale porous skeleton through a simple solution based method and after pyrolysis, unique catalyst architectures were created with a large number of active sites for the ORR and a large pore volume for the fast transport of oxygen gas and aqueous electrolyte to the active sites. In the constructed Zn–air full cells, the voltage of the obtained M–N_x/C catalysts became higher than that of the cell with the Pt/C catalyst at higher current densities and the corresponding peak power density of the cell with M–N_x/C catalyst was about 200 mW cm^{-2}, which is slightly higher than about 195 mW cm^{-2} for the cell with the Pt/C catalyst, suggesting that M–N_x/C catalysts with unique porous architectures could enhance the rapid mass and charge transfer.

Another efficient pathway to improve the ORR activity is by creating abundant catalytic sites on carbon supports. Recently, Dai's group developed a new strategy through introducing abundant defects and functional groups onto the carbon nanotubes to increase the number of catalytic sites.[297] Under unique oxidation conditions, the outer walls of the few-walled carbon nanotubes are partially unzipped, producing abundant defects on the outer walls of the carbon nanotubes and forming large amounts of nanoscale graphene sheets attached to the intact inner walls of the nanotubes, as shown in Fig. 26a. The edge- and defect-rich graphene sheets facilitate the formation of catalytic sites with iron impurities for the ORR on annealing in NH_3. In acidic solutions, the catalyst exhibits high ORR activity and superior stability, and in alkaline solutions its ORR activity closely approaches that of platinum. Moreover, iron and nitrogen atoms have been imaged at the atomic scale for the first time by using annular dark-field (ADF) imaging and electron energy loss (EEL) spectrum imaging in aberration-corrected scanning transmission electron microscopy (STEM). It was found that iron atoms on the graphene sheets are often adjacent or close to nitrogen atoms (Fig. 26c–f), suggesting possible Fe–N bonding.

The active sites are very important for oxygen electrocatalysts. However, in most of the cases the actual configurations of the active sites are difficult to determine. A typical example is the pyrolyzed M–N_x/C catalysts. Many results have revealed that transition-metal ions, coordinated by pyridinic N atom functionalities, are the active sites for electrocatalysis. However, the detailed coordination structures of the active sites are yet to be identified. The current proposed active sites are edge plane M–N_2/C and M–N_4/C species, basal plane macrocyclic M–N_4/C

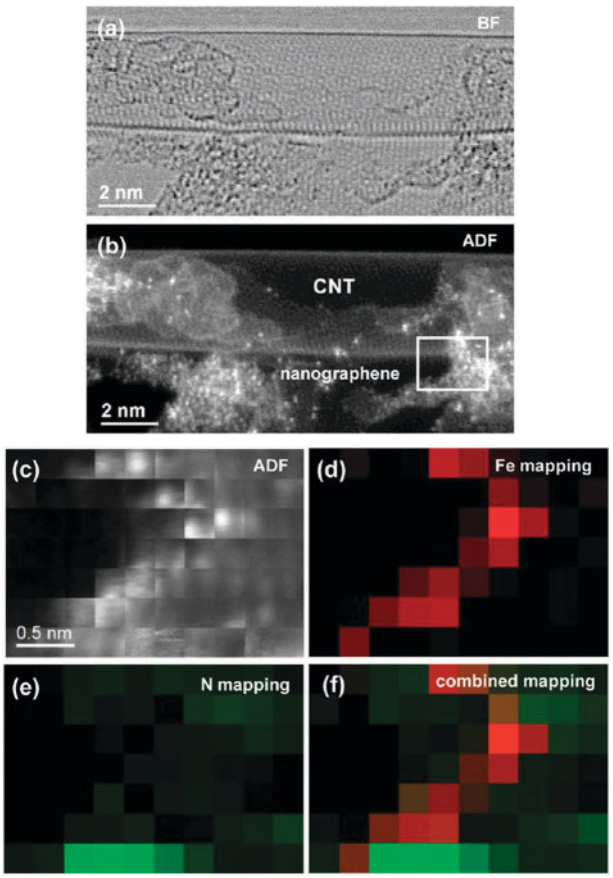

Fig. 26 (a) Bright-field and (b) simultaneously acquired annular dark-field (ADF) STEM images of a CNT partially covered with nanosized graphene pieces showing many heavy atoms in the NT-G material. The area marked by the white square in (b) is further characterized by (c) ADF intensity mapping, (d) Fe electron energy loss spectroscopy (EELS) mapping, (e) N EELS mapping, and (f) overlaid Fe and N EELS maps. The ADF and EELS maps were recorded simultaneously. Reprinted with permission from ref. 297, copyright 2012, Nature Publishing Group.

species as well as graphitic nitrogen N/C species, which are mainly speculated by data obtained from X-ray photoelectron spectroscopy (XPS), extended X-ray absorption fine structure (EXAFS), time-of-flight secondary ion mass spectroscopy (ToF-SIMS), Mössbauer spectroscopy, *etc.*[323–325] Recently, based on DFT, Fe–N_3 and Fe–N_2 have been claimed to be the possible active sites for the ORR, while Fe–N_4 may be not.[40] Unfortunately, the proposed sites can only be called "hypotheses" and many relevant fundamental aspects, such as coordination chemistry and geometric structures of the active sites, are not fully understood. Up to now, the active site structures of the pyrolyzed M–N_x/C are still a controversial subject. The difficulty in determining active site structures stems from the complexity and variety of the catalysts' surfaces.[284] To gain in-depth insights, a combination of *in situ* experimental analysis, especially atomic-scale probing, and the theoretical investigation would be valuable. It is noteworthy that theoretical contributions have been made to elucidate the electrocatalysis process on the benchmark catalyst Pt, offering a potential way to study the surface configurations of the pyrolyzed M–N_x/C under electrochemical conditions.[326]

Pyrolyzed M–N_x/C catalysts have also been successfully applied in nonaqueous Li–air batteries as early as the first report by Abraham. In that work, a pyrolyzed CoPc/carbon catalyst efficiently increased the discharge voltage by 0.35 V and decreased the charge overvoltage by 0.3 V in a polymer electrolyte-based Li–O_2 battery.[18] Later, pyrolyzed CuFePc complexes as catalysts for oxygen reduction were investigated in nonaqueous systems.[327,328]A higher discharge voltage and rate were achieved using pyrolyzed CuFePc catalyst compared to pristine carbons. Recently, great progresses have been made in the application of M–N_x/C catalysts for nonaqueous Li–air batteries. One representative catalyst is the Fe/N/C composite prepared by the pyrolysis of supported iron(II) acetate and 1,10-phenanthroline.[329] The improved performance of the rechargeable Li–O_2 battery is observed when a Fe/N/C composite is used as the cathode catalyst. It can be seen that such a catalyst could reduce the overpotentials during both discharge and charge processes compared with the metal oxide catalyst or high surface-area carbon (Fig. 27a). More importantly, only oxygen was detected during the charging step when Fe/N/C was used as the cathode catalyst, whereas CO_2 was also found in comparable cells using α-MnO_2 or carbon under the same conditions (Fig. 27b). The Li–O_2 batteries with Fe/N/C as the catalyst also exhibited high cyclability (more than 50 cycles with excellent capacity retention). The improved activity may arise from its structural advantages: Fe/N/C active sites are atomically dispersed in the carbon matrix with high surface density and such a catalyst could produce a higher interfacial boundary with the lithium oxide precipitates, lowering both electron and mass transport barriers and thereby reducing the overpotentials during charging.[329] Another successfully example is nitrogen-doped graphene-rich catalysts (Co–N-MWNTs) derived from heteroatom polymers for oxygen reduction in nonaqueous Li–O_2 battery cathodes.[330] The Co–N-MWNTs was synthesized *via* graphitization of an aromatic heteroatom polymer, polyaniline under catalysis of cobalt species supported on multi-walled carbon nanotubes (MWNTs). Compared to the reported metal-free graphene catalysts, the addition of the Co species introduces a high level of quaternary and pyridinic N in the graphene composite catalysts and significantly improves the catalytic activity for the ORR. At the same time, beneficial mass and electron transport, specific interactions between active site and MWNTs, as well as high corrosion resistance can all improve the cathode performance.

3.5 Transition metal nitrides

Due to the significanly different electronegativity between the metal and nitrogen atoms, there is charge transfer in the nitrides. This charge transfer was proved to result in the creation of base and/or acid sites, which led to various catalytic activities such as isomerization, dehydrogenation, hydrogenation and so on. In the early research, Mazza and Trassatti synthesized a TiN compound using a direct nitriding method and found that TiN exhibited activity towards the ORR with excellent electronic conductivity in alkaline solutions.[331] Later, nitride-based ORR catalysts such as Mn_4N, CrN, Fe_2N, Co_3N, and Ni_3N

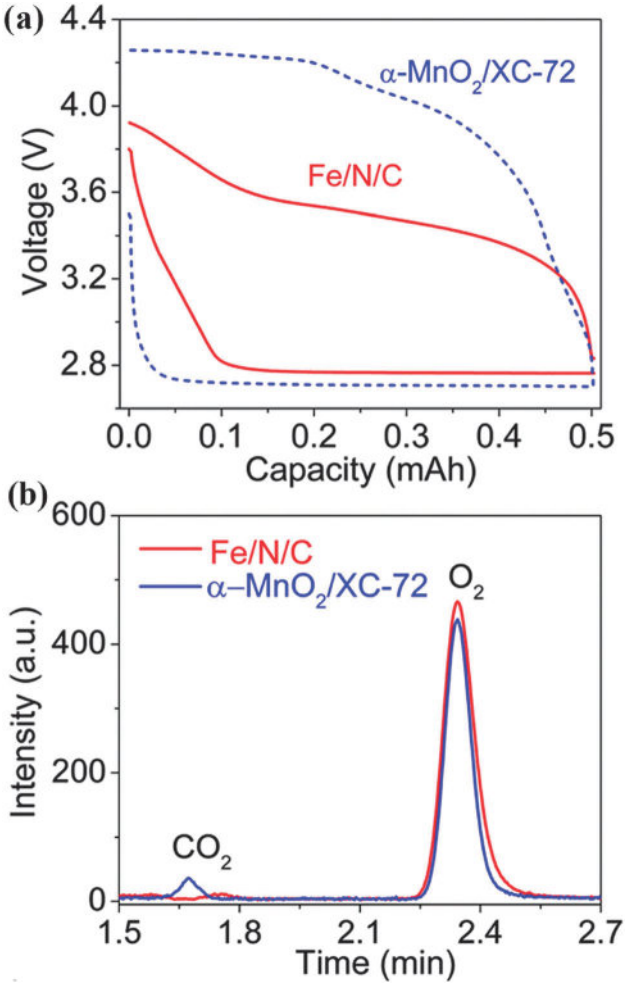

Fig. 27 (a) Discharge–charge voltage profiles of Li–O_2 cells using α-MnO_2/XC-72 and Fe/N/C as cathode catalysts. (b) Representative GC signals as a function of retention time for the gas effluents collected at the end of the charging processes of panel a. Reprinted with permission from ref. 329. Copyright 2012, American Chemical Society.

were investigated in alkaline electrolyte. It was found that the Mn_4N-based air cathode promoted the direct four-electron ORR mechanism and supplied a stable performance during a 50 h test.[77] Subsequently, carbon-supported molybdenum nitride, tungsten nitride and niobium nitride were synthesized using pyrolysis methods and explored the possibilities of these materials as fuel cell catalysts.[332–334] As ORR electrocatalyst materials, transition metal nitrides have relatively good stability under acidic conditions and high electrochemical potentials. Carbon supported Co–W treated with NH_3 at high temperatures was also found to possess some catalytic activity towards the ORR.[335] However, the catalytic ORR activity was strongly dependent on the NH_3 heat-treatment temperature, the metal composition ratio and method of preparation. The structures of metal nitrides influence their catalytic activities toward the oxygen reduction reaction. Sun's group compared two carbon-supported molybdenum nitrides, MoN/C and Mo_2N/C, prepared by varying the experimental conditions in an NH_3 atmosphere.[336] The results show that the MoN/C exhibits higher catalytic activity toward the ORR than the Mo_2N/C. From the density functional theory calculations, it was found that both the MoN and the Mo_2N facilitate the dissociation of oxygen molecules, but the suitable geometric structure of the MoN and the preferred oxygen adsorption type on it contribute to the higher activity of MoN/C toward the ORR.

Nanostructured materials have been widely proved to have additional advantages for electrocatalysis. Chen and Wu reported a facile preparation of Cu_3N nanocubes by a one-phase process.[337] The crystal size could be tuned easily by using different primary amines as the capping agents. Such nanocrystals delivered promising electrocatalytic activity towards the oxygen reduction. Domen's group reported the direct synthesis of TiN nanoparticles on carbon black supports using a mpg-C_3N_4–carbon black composite as a template, which ensured improved contact between the electrocatalyst (TiN) and carbon supports.[338] This nanocomposite can function as an efficient cathode catalyst for the ORR in polymer electrolyte fuel cells. In 2011, TiN was firstly used as an ORR catalyst in a Li–air fuel cell with a nonaqueous–acidic aqueous hybrid electrolyte by Zhou's group.[339] A high ORR cathodic current was observed at an onset potential of 3.80 V *vs.* Li/Li^+. The single cell exhibited a discharge curve with a voltage plateau of 2.85 V at the current density of 0.5 mA g^{-1}. Later, the same group studied the electrocatalytic activities of nano- and micro-sized TiN toward the oxygen reduction reaction (ORR) in an alkaline media using a thin film-rotating-disk electrode (RDE) technique, and also investigated their performances as active air electrodes on a Li–air fuel cell with a hybrid electrolyte.[340] It is interesting that the electrocatalytic activities of both nano- and micro-sized TiN exhibit different mechanisms toward the ORR in alkaline media. The ORR catalyzed by microsized TiN proceeds *via* the 2-electron pathway in a consecutive manner with the reduction of HO_2^- starting at a higher electrode potential. In contrast, the ORR catalyzed by nano-sized TiN proceeds *via* a dual-path, where the two serial "$2e^-$" steps proceed with smaller intervals and manifest an overall mixed appearance by the coexistence of the parallel and serial "$2e^-$" steps. In the assembled Li–air cells, both nano- and micro-sized TiN particles demonstrate evident electrocatalytic activities towards the ORR, with the nano-sized TiN showing much better catalytic activity, which is comparable to that of the nano-sized Mn_3O_4.

For the TiN catalyst, its successful application in aqueous systems was also extended to that in a nonaqueous system. As the cathode catalyst, TiN nanoparticles supported on Vulcan XC-72 (n-TiN/VC) exhibited an onset potential for the OER at 2.9 V, contrasting with a mixture of micro-sized TiN and VC (m-TiN–VC), and VC, both at about 3.1 V in a nonaqueous Li–O_2 battery (Fig. 28a).[341] The discharge–recharge voltage gap of n-TiN–VC was estimated to be 1.05 V, which is 390 and 450 mV smaller than that of m-TiN–VC and VC, respectively, at 50 mA g_{carbon}^{-1}, which indicates that n-TiN–VC can function as both an active ORR catalyst during discharge and an efficient OER catalyst during recharge. In Fig. 28b, n-TiN–VC also exhibited a larger capacity of 6407 mA h g_{carbon}^{-1} in comparison with m-TiN–VC and VC. The enhanced performance can be

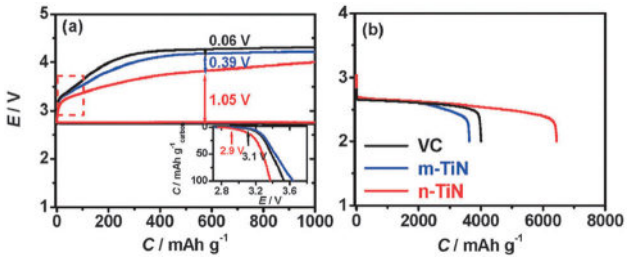

Fig. 28 (a) Discharge–recharge curves of VC (Vulcan XC-72), micro-sized m-TiN/VC, and nano-sized n-TiN/VC as cathode catalysts of Li–O_2 batteries and an enlarged section highlighted (inset) at 50 mA g_{carbon}^{-1} and (b) their discharge curves at 500 mA g_{carbon}^{-1}. Reprinted with permission from ref. 341, copyright 2013, Royal Society of Chemistry.

ascribed to the high catalytic activity of TiN nanoparticles and the intrinsic contact between them and VC. The superior catalytic activity and high conductivity of TiN will make it applicable as an alternative support to carbon in nonaqueous Li–O_2 batteries. Another successful example is a hybrid nanostructured material of molybdenum nitride–nitrogen-doped graphene nanosheets (MoN–NGS) designed by Cui's group as an O_2 cathode (Fig. 29).[342,343] MoN nanoparticles were homogeneously dispersed on N-doped graphene nanosheets. The hybrid nanocomposite exhibits a high discharge plateau at around 3.1 V and a considerable specific capacity (1490 mA h g^{-1}, based on carbon + electrocatalyst). The achieved round-trip efficiency of 77% was comparable to that of a PtAu/C cathode. Recently, the same group has also successfully prepared mesoporous cobalt molybdenum nitride (Co_3Mo_3N) with using a coprecipitation method followed by ammonia annealing treatment.[344] Many more active sites were generated by the well designed mesoporous nanostructure, and the intrinsic electronic configuration lead to an excellent bifunctional electrocatalytic performance for the ORR/OER in nonaqueous Li–O_2 cells,

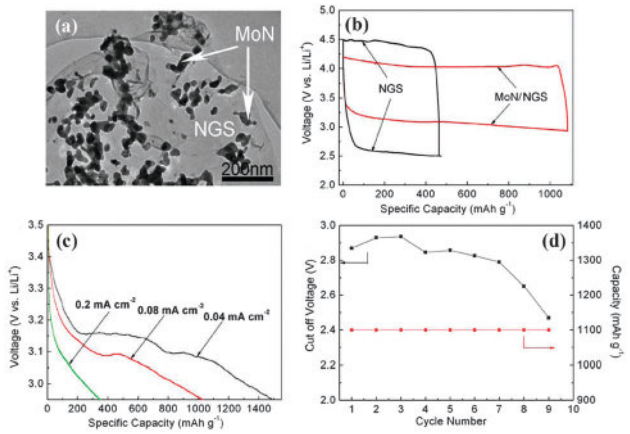

Fig. 29 (a) TEM images of MoN–NGS. (b) Discharge–charge curves of MoN–NGS and NGS at the current density of 0.08 mA cm^{-2}. (c) Discharge curves of MoN–NGS at different current densities. (d) Cycle performance of MoN–NGS cathode based Li–O_2 batteries with restricting the capacity to 1100 mA h g^{-1} at a current density of 0.08 mA cm^{-2} (red) and the cut off voltage of discharge, correspondingly (black). Reprinted with permission from ref. 342, copyright 2011, Royal Society of Chemistry.

delivering considerable specific capacity and alleviating polarization. To date, the application of transition metal nitrides for nonaqueous Li–air battery air electrodes is still quite limited and needs further studies to design a highly efficient electrocatalyst for nonaqueous Li–air batteries.

3.6 Conductive polymers

In addition to the macrocycle compounds, organic conductive polymers such as polypyrrole (PPy), polyaniline (PANI), polythiophen (PTh), poly(bis-2,6-diaminopyridinesulfoxide) (PDPS) and poly(3-methyl)thiophen (PMeT), characteristically display mixed metal and polymer like properties and are also attractive materials in oxygen electrocatalysis.[345–357] These polymers usually have either nitrogen or sulfur contained in their inherent structure. For example, a type of intrinsically conductive polymer, poly(3,4-ethylenedioxythiophene) (PEDOT), was found to have surprisingly high activity for oxygen reduction in alkaline medium and a Zn–air battery constructed based on this PEDOT air-electrode provided an open-circuit voltage of 1.44 V and exhibited a better performance than a Pt/Goretex air electrode under the same test conditions.[351] On the other hand, the incorporation of transition metal complexes into the conductive polymer matrices can improve the activity of carbon supported conductive polymer composites. For example, polypyrrole was firstly used as a matrix for entrapping cobalt to generate Co–N active sites for the ORR by Bashyam and Zelenay.[347] Without any optimization, the cobalt–polypyrrole composite catalyst enables high power densities and displays no signs of performance degradation for more than 100 hours. The observed ORR activity was attributed to the strong Co–PPy interactions, possibly forming Co–N catalytically active sites. Transition metal compounds are typically incorporated into the two kinds of polymers: PANI or PPy polymers (forming M–N_x configuration), or incorporated into PTh or PMeT polymer composites (forming M–S_x configuration).[284]

Wen's group firstly applied PPy with a tubular morphology as the support and catalyst for the cathode of nonaqueous Li–O_2 cells.[358] The extensive electrochemical examinations showed that the tubular PPy supported air electrode exhibited a higher reversible capacity, round-trip efficiency, and significantly better cycle stability and rate capability than the conventional carbon (acetylene carbon black, AB) supported cathodes. As shown in Fig. 30d, at the current density of 0.1 mA cm^{-2}, the discharge voltage of the tubular PPy composite is consistently higher than that of the granular PPy supported cell by about 100 mV and AB by about 300 mV, while its charge voltage is substantially lower than that of granular PPy by 100 mV and AB by 600 mV. At the same time, the Li–O_2 cells with tubular PPy supported electrodes present significantly better cycle stability than AB at each current density (Fig. 30e). The excellent performance of the tubular PPy based cell can be attributed to the possible ORR and OER electrocatalytic activities of the PPy and the improved oxygen diffusion kinetics owing to the hydrophilic property and the special tubular structure with hollow channels of PPy. This work indicated that the conducting polymer with hydrophilic property could be good candidates as supports and catalysts

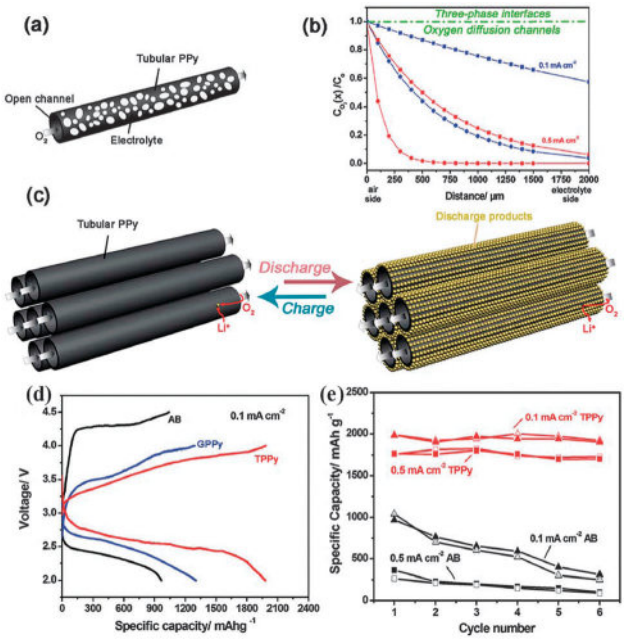

Fig. 30 (a) Schematic representations of the organic electrolyte and oxygen distributions on hydrophilic PPy nanotubes. (b) Oxygen gradient across the flooded porous cathode. (c) The schematic discharge–charge process. (d) First discharge–charge curves of the acetylene carbon black (AB), granular PPy and tubular PPy supported Li–O_2 cells at 0.1 mA cm^{-2} in oxygen. (e) Discharge–charge capacities *versus* cycle numbers at current densities of 0.1 and 0.5 mA cm^{-2}. Specific capacities are based on per gram of the supports. Reprinted with permission from ref. 358, copyright 2012, Royal Society of Chemistry.

for the reversible air electrodes of nonaqueous Li–air batteries, opening a new way for the development of high-performance Li–air batteries. Recently, Lu *et al.* synthesized water dispersed conducting PANI nanofibers doped with phosphate ester and investigated their potential application in Li–air batteries.[359] The experimental result showed that this low cost and easily produced material could catalyze the discharge reaction independently, and after an initial degradation from 3260 to 2320 mA h g_{PANI}^{-1} during the first three cycles at a current density of 0.05 mA cm^{-2}, its discharge capacity kept relatively stable over the next 27 cycles with only a 4% loss, which may provide a new choice for high-capacity rechargeable Li–air batteries.

3.7 Noble metal, alloy, and oxides

Noble metal platinum (Pt) is the most effective catalyst to facilitate ORR reactions because of its known high stability and superior electrocatalytic activity.[360–364] As a result, Pt is often chosen as a benchmark material in current studies of alternative catalysts. However, the scarcity and cost of Pt make it necessary to maximize the activity of a Pt-based catalyst by engineering its morphology and composition. During the last few decades, a number of strategies have been proposed for improving the performance of Pt-based catalysts. For example, tuning the size and morphology to achieve a small/dispersive size, high surface areas and desired highly active facets has been proven as an efficient route to improve the ORR properties on a mass basis.[365–370] Another most viable strategy to simultaneously enhance the performance and lower the cost is alloying or modifying Pt with other appropriate noble metals or early transition metals that are less expensive. Through adjusting the electronic structure and increasing the active facets, these bimetallic catalysts ($Pt_3Ni(111)$, Pt–Pd, and Pt–Au) have shown great improvements in activity and stability.[371–376] Most initial studies on hybrid Li–O_2 cells also utilized Pt as the electrocatalyst as a model catalyst for the ORR.[377–379] The effect of Li^+ ions on the ORR was investigated in an acidic electrolyte on a Pt catalyst and it was found that the Li^+ in sulfuric acid electrolytes does not strongly adsorb on or interact with the active surface of the Pt catalyst, but it decreases the diffusion rate of O_2 in the electrolyte solution due to its affinity for oxygen. Accordingly, the intrinsic kinetic activities were found to decrease with the increase of Li ion concentration, but level off when the Li ion concentration is larger than 1.0 M.

The ORR in alkaline media is more facile than in acid media, making the use of less expensive catalyst materials in place of platinum possible. Cheaper precious metals such as palladium, gold, silver and their alloys have been the subject of many investigations because of their modest activity and relatively higher abundance. For example, Pd in alkaline solutions showed particularly high activity, suggesting it may offer a potential replacement for Pt.[380] The relatively inexpensive and abundant Ag is another excellent candidate to replace Pt for ORRs in alkaline solutions. Silver has the highest electrical conductivity of any element and is approximately 100 times less expensive than platinum. Moreover, silver is one of the most active catalysts for the ORR, even competitive to Pt in high concentration alkaline media. Several research groups have investigated the effects of pH values, particle size, metal loading and impurity poisoning on silver catalysts for ORRs in alkaline media. From the results of Blizanac, it was observed that the ORR on a Ag(111) single crystal surface in 0.1 M KOH proceeds through the 4e reaction pathway with a very small amount of peroxide formation over the entire potential range, while that in 0.1 M $HClO_4$ occurs as a 2e, a mixed 2e and 4e, and a 4e reduction process sequentially from low to high overpotentials.[381] Lima *et al.* found a 2.3e ORR on 20 wt% Ag/C with relatively large 47.7 nm silver particle size, while the result from Demarconnay *et al.* showed a 3.6e ORR on 20 wt% Ag/C with a particle size close to 15 nm.[382,383] For the influence of metal loading on the Ag/C catalyst activity, Varcoe *et al.* and Guo *et al.* found the performance of Ag/C electrodes with 60 wt% metal loading to be as good as that on 20 wt% Pt/C electrodes.[384,385] Recently, a bimetallic Ag–Co alloy and Ag–Au Janus nanoparticles have also been demonstrated to possess good electrocatalytic functions in alkaline cathodes. Thus, silver-based catalysts are promising cathode materials in alkaline electrolytes with a good balance between cost and performance.

The applications of noble metals in nonaqueous Li–air batteries have been investigated systematically by Shao-Horn's group.[59,64,386–388] In the early study, they observed that Au/C had the highest discharge activity in nonaqueous electrolyte, while Pt/C exhibited an extraordinarily high charging activity.

In order to exert both advantages, they combined Au and Pt onto the surfaces of individual PtAu nanoparticles and examined the ORR and OER activity of such particles supported on carbon in Li–O_2 cells. Interestingly, a highly active bifunctional electrocatalyst was observed on the PtAu/C catalyst, giving rise to the high round-trip efficiency of rechargeable Li–O_2 batteries.[387] Although this work was carried out in a PC/DME electrolyte, which may cause parasitic reactions, the design principle of placing select atoms (such as Pt and Au) with different functions on nanoparticle surfaces is a promising strategy to develop highly active bifunctional catalysts for Li–air batteries. Later, the same group further investigated the catalytic activity trends of the ORR for four polycrystalline surfaces of noble metals (Pd, Pt, Ru and Au) in a more stable electrolyte (0.1 M $LiClO_4$ 1,2-dimethoxyethane) *via* rotating disk electrode measurements.[388] It was found that the nonaqueous Li^+-ORR activity of these surfaces primarily correlates to the oxygen adsorption energy, forming a ''volcano-type'' trend, shown in Fig. 31a. More importantly, the activity trend found on the polycrystalline surfaces was in good agreement with the trend in the discharge voltage of Li–O_2 cells catalyzed by nanoparticle catalysts (Fig. 31b). Such a volcano-type ORR activity trend on these surfaces is consistent with the mechanism proposed previously.[59] In nonaqueous electrolytes, the first electron reduction usually proceeds by the formation of a superoxide species such as O_2^- and LiO_2. Similarly to the ORR process of noble metals in aqueous electrolytes, the binding energy of the oxygen to the catalytic surface determines the reaction pathways. On surfaces with weak bindings with oxygen, such as Au, LiO_2 may disproportionate or undergo a second electron reduction to form Li_2O_2. In contrast, on surfaces with an increasing binding energy with oxygen such as Pt and Pd, the kinetics of the second electron reduction is enhanced to form $Li_2O + O_{adsorbed}$ instead of Li_2O_2, and then $O_{adsorbed}$ subsequently undergoes an additional two-electron reduction to form Li_2O. However, if further increasing the binding energy of oxygen on surfaces such as Ru, the adsorbed oxygen species may bind very strongly on the surface to hamper the subsequent electron transfer, leading to reduced ORR activity.[388]

The operation of a rechargeable Li–O_2 battery depends critically on the repeated and highly reversible formation–decomposition of lithium peroxide (Li_2O_2) at the cathode upon cycling. Recently, Bruce's group has made great progress in reversible and high-rate Li–O_2 batteries.[389] By applying porous gold as a cathode and dimethyl sulfoxide as the electrolyte, the Li–O_2 cell can sustain reversible cycling, retaining 95% of its capacity after 100 cycles and having >99% purity of Li_2O_2 formation at the cathode, even on the 100th cycle, and its complete oxidation on charge (Fig. 32). The charge-to-mass ratio on discharge and charge is $2e^-/O_2$, confirming that the reaction is completely Li_2O_2 formation–decomposition. In particular, porous gold electrodes are effective at promoting the decomposition of Li_2O_2, with all the Li_2O_2 being decomposed below 4 V and ~50% decomposed below 3.3 V, at a rate approximately one order of magnitude higher than on carbon. The excellent performance of the gold electrode can be ascribed to

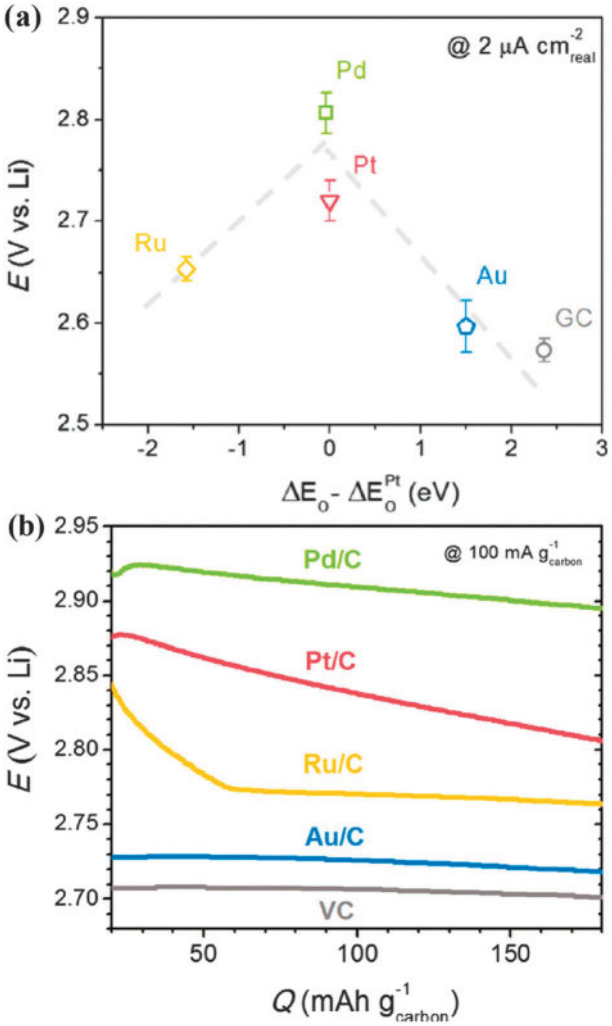

Fig. 31 (a) Nonaqueous Li^+-ORR potentials at 2 μA cm^{-2} real as a function of calculated oxygen adsorption energy, ΔE_O (per oxygen atom relative to an atom in the gas phase), relative to that of Pt. The oxygen adsorption energy on GC is estimated from the oxygen adsorption energy on graphite. Error bars represent standard deviations of at least three independent measurements. (b) Initial discharge profiles of Li–O_2 cells of Pd/C, Pt/C, Ru/C, Au/C, and VC at 100 mA g^{-1} carbon. Reprinted with permission from ref. 388. Copyright 2012, American Chemical Society.

the synergistic effect of the catalytic action, high conductivity, high stability and rigid porous structure of the gold foil. Although the cost of Au is still a problem, a real Li–O_2 cathode reaction is firstly realized by overwhelmingly dominating Li_2O_2 formation on discharge, its complete oxidation on charge and sustainability on cycling.

More recently, Jung *et al.* evaluated the electrocatalytic activity of ruthenium-based nanomaterials loaded on reduced graphene oxide for promoting the OER in nonaqueous Li–O_2 cells using a $LiCF_3SO_3$–TEGDME solution as the electrolyte.[390] The results showed that hydrated ruthenium oxide supported on graphene (RuO_2·0.64H_2O–rGO) outperformed those based on metal ruthenium also supported on graphene (Ru–rGO) by displaying a superior catalytic activity, remarkably reducing charge potentials to ~3.7 V even at high current density of

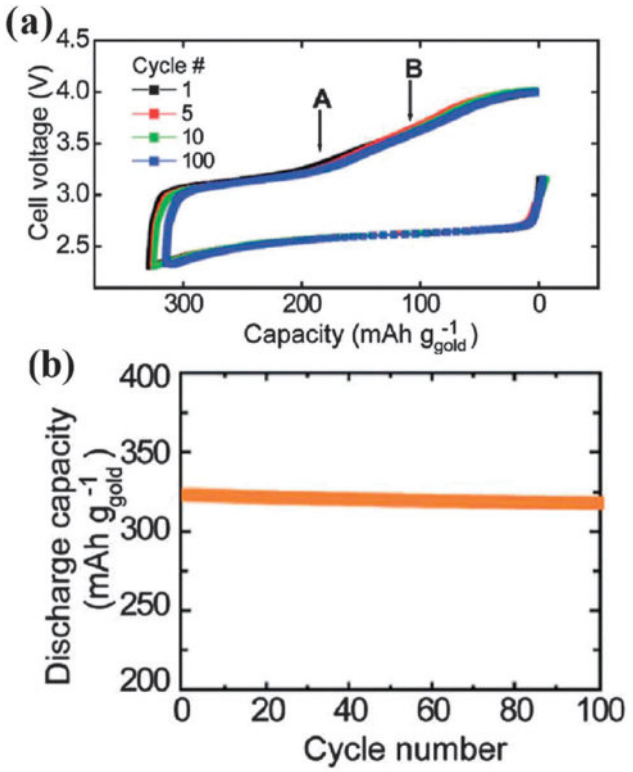

Fig. 32 Charge–discharge curves (a) and cycling profile (b) for a Li–O_2 cell with a 0.1 M $LiClO_4$–DMSO electrolyte and a nanoporous gold cathode, at a current density of 500 mA g^{-1} (based on the mass of Au). Reproduced with permission from ref. 389, copyright 2012, American Association for the Advancement of Science.

500 mA g^{-1} and high capacity of 5000 mA h g^{-1}. Li–air cells employing $RuO_2{\cdot}0.64H_2O$–rGO cathodes maintained stable cycling performances for over 30 cycles. The higher activity of the oxide may be due to the weaker oxygen bonding compared to chemisorbed oxygen on the metal. Moreover, the density of $RuO_2{\cdot}H_2O$ is smaller than that of Ru, which can also provide more active surface sites at the same loading. This work further demonstrated the key role of proper engineering of the catalyst materials and nanostructures.[391,392]

4 Challenges from aqueous to nonaqueous systems

In the early studies of metal–air batteries, researchers focused on aqueous Zn–air batteries due to their low cost and easy operability. Nowadays, with the constantly increasing energy demand, nonaqueous Li–air batteries have attracted worldwide attention due to their advantages of energy density and rechargeability over aqueous Zn–air batteries. Interestingly, from the above discussion, oxygen catalysts for aqueous systems also show promising performances for nonaqueous systems despite the different reaction mechanisms. The similarity between both systems provides great opportunities for the development of nonaqueous Li–air batteries, and important progress has been achieved. However, nonaqueous Li–air batteries are still in their infancy and there are several challenges beyond the choice of electrolyte, cathode and anode for oxygen electrocatalysts.

Carbonate-based organic electrolytes such as propylene carbonate (PC) have been widely used in Li–air batteries because carbonate mixtures are the dominating electrolyte solvents in LIBs.[393,394] However, Mizuno *et al.* found that the discharge products of Li–O_2 cells using PC-based electrolytes were mainly lithium carbonates, instead of the desired Li_2O_2.[78] Later, Bruce's group further confirmed this result and reported that an alkyl carbonate electrolyte decomposed into $C_3H_6(OCO_2Li)_2$, Li_2CO_3, HCO_2Li, CH_3CO_2Li, CO_2, and H_2O at the cathode during discharge and charging involved the oxidation of $C_3H_6(OCO_2Li)_2$, Li_2CO_3, HCO_2Li, CH_3CO_2Li accompanied by CO_2 and H_2O evolution.[79] The different pathways for discharge and charge results in the large voltage gap in Li–O_2 cells. Since then, alternative solvents have been investigated both experimentally and theoretically. Ether solvents were found to have relatively higher stabilities than PC. Li_2O_2 could be observed as the main discharge product in dimethoxyethane (DME) based Li–air cells by McCloskey.[66] Sun and Scrosati *et al.* also demonstrated that the Li–air battery was capable of operating for 100 cycles with a capacity of 1000 mA h g_{carbon}^{-1} by applying a tetra(ethylene)-glycol dimethyl based electrolyte (TEGDME–1 M $LiCF_3SO_3$).[395] However, the results from Bruce and coworkers showed that the amount of Li_2O_2 in the discharge products gradually decreased during cycling for the ether electrolyte and at the fifth discharge, no Li_2O_2 was observed but other lithium compounds were observed in the discharge products.[80] Furthermore, the electrolyte degradation appeared to increase rapidly with cycling. Using a similar route, the same group investigated amide based electrolytes, such as dimethylformamide (DMF), and observed the similar phenomenon of increasing electrolyte decomposition on cycling, as shown in Fig. 33.[396] Recently, the same group demonstrated a promising electrolyte of 0.1 M $LiClO_4$ in dimethylsulfoxide (DMSO) and realized over 100 cycles with little decay, as discussed above. Unfortunately, such an electrolyte is only efficient on a gold electrode and if carbon materials exist, the decomposition reactions are also serious.[389] So the development of novel electrolytes with high electrochemical stability is an urgent task for nonaqueous Li–air batteries. More recently, Zhou and Zhang replaced liquid electrolytes with a solid Li-ion conductor to circumvent the decomposition problem of liquid electrolytes, which may provide an alternative approach.[397] In the electrolyte, the lithium salt concentration is also an influencing factor for battery performance.[398] The varying of the molar ratios of lithium salt and solvent can modify their solvate structures from solvent separated ion pairs (SSIP) to contact ion pairs (CIP).[31] With the electrolyte of bis(trifluoromethylsulfonyl)amide (LiTFSA) and tetraglyme (G4), it was found that the Li–O_2 cell, with a molar ration of LiTFSA : G4 = 1 : 5 shows the best cycling stability over the evaluated molar ratios of 1 : 1, 1 : 3, and 1 : 7.[399] The dependence of the cycling performance of the Li–O_2 batteries on the concentrations will be helpful for exploiting the stable electrolyte systems.

Besides the electrolyte, the stability of the cathode material is also an important issue in the application of Li–air batteries.

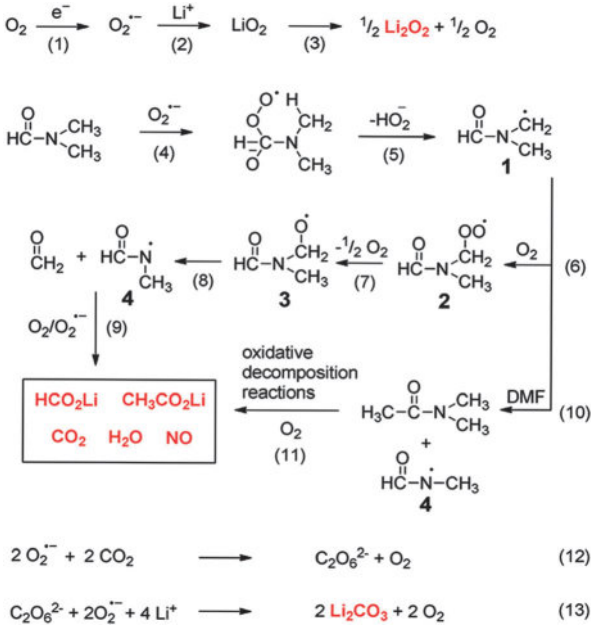

Fig. 33 Proposed mechanism for reactions occurring during discharge for the dimethylformamide electrolyte. Reprinted with permission from ref. 396. Copyright 2012, American Chemical Society.

Most of the published results are obtained with carbon or carbon based cathodes. However, similar to carbon corrosion in fuel cells, carbon materials also undergo corrosion challenges at the high operation potentials, especially for the charging process and high oxygen circumstances in Li–air batteries. Several recent works have examined the stability of a carbon cathode in nonaqueous Li–O_2 cells.[400,401] Typically, Bruce's group demonstrated that carbon is relatively stable below 3.5 V (*vs.* Li/Li^+) on discharge or charge, but is unstable on charging above 3.5 V in the presence of Li_2O_2, undergoing oxidative decompostion to form Li_2CO_3 (Fig. 34).[402] Moreover, carbon also promoted electrolyte decomposition during discharge and charge in a Li–O_2 cell, giving rise to Li_2CO_3 and Li carboxylates (based on DMSO and tetraglyme electrolytes). Unfortunately, the formed Li_2CO_3 could not be oxidized completely on charging and it accumulated on cycling, leading to electrode passivation and capacity fading. It was also found that hydrophobic carbon is more stable and less able to promote electrolyte decomposition than its hydrophilic counterpart. At the same time, if the charging of Li_2O_2 could be carried out below 3.5 V, carbon may be a suitable electrode. From the results, it should be emphasized that the stable cycling of Li_2O_2 at the cathode in a Li–O_2 cell depends on the synergy between the electrode and the electrolyte rather than each in isolation. To avoid the degradation of carbon, the development of highly efficient catalysts that decrease the overpotential is necessary.

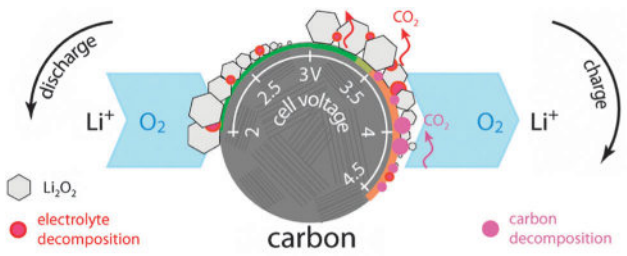

Fig. 34 Illustration of the decomposition process of carbon electrodes during discharge and charge in nonaqueous Li–air batteries. Reprinted with permission from ref. 402. Copyright 2013, American Chemical Society.

Another challenge for the application of Li–air batteries is the reactivity of the lithium metal anode. Even after decades of extensive research, the development of rechargeable batteries with a lithium metal anode is still hindered by two important problems.[27] The first is the growth of lithium dendrites during cycling, leading to the internal short-circuit of the batteries and thus severe safety issues.[403] The second is the low charge–discharge efficiency, which comes from several aspects, for example, the continuous growth of a solid electrolyte interface (SEI) layer and the formation of irreversible "dead lithium".[404,405] Many efforts have been made to improve the lithium anode performance in LIBs but few efforts for rechargeable Li–air batteries. Lithium metal anodes present new and more challenging problems in rechargeable Li–air batteries. Recently, Walker *et al.* applied electrolyte additive lithium nitrate ($LiNO_3$) to stabilize the SEI of a Li anode with the solvent of *N*,*N*-dimethylacetamide (DMA).[406] A Li–O_2 cell containing this electrolyte composition was shown to cycle for more than 2000 h (>80 cycles) at a current density of 0.1 mA cm^{-2} with a consistent charging profile, good capacity retention, and O_2 detected as the primary gaseous product formed during charging. For the safety of the highly reactive lithium metal anode, Scrosati *et al.* replaced it with a lithiated silicon–carbon anode.[407] The results demonstrated that the basic reversibility of the electrochemical process of the battery can be promisingly cycled with a rather high specific capacity. From the research of LIBs, it was found that the proper electrolyte (including solvents, salts, and additives) with good lithium anode compatibility shows a great positive effect because it changes the SEI film more directly and more significantly. Therefore, finding an ideal electrolyte is also important for the protection of the lithium metal anode in Li–air batteries. In summary, the development of highly efficient oxygen catalysts needs to face the challenges brought about from the electrolyte, cathode and anode.

5 Conclusion and outlook

Metal–air batteries are predicted to be the next generation battery technology because their high specific energy has the potential to meet the ever-increasing demands of electrical energy storage for many emerging applications, such as electric vehicles and smart grids. To realize the potential, it is vital to find highly active catalysts with good stability for oxygen reduction and oxygen evolution in metal–air batteries. This review has highlighted recent progress in electrochemistry and in the materials chemistry of oxygen catalysts for metal–air

batteries. The electrochemical reaction pathways of the ORR and OER have been discussed in both aqueous and non-aqueous electrolytes. Seven categories of catalytic materials have shown very promising catalytic activity and stability, including metal oxides, carbonaceous materials, metal oxide–nanocarbon hybrid materials, metal–nitrogen complexes, transition metal nitrides, conductive polymers and precious metals. Among them, metal oxides are the most widely studied as non-precious catalysts in aqueous Zn–air and nonaqueous Li–air batteries. In particular, single oxide such as MnO_x has been intensely investigated for oxygen catalysts in both batteries. For carbonaceous materials, proper doping is proved to an efficient way of tailoring the catalytic activity; the morphology and pore size are important as well. Metal oxide–nanocarbon strong coupled hybrid materials are a new and rising sort of oxygen catalytic material and exhibit very promising catalytic activity. The metal–nitrogen complexes are an important alternative catalyst for the ORR and the optimization of raw materials and reaction conditions will produce high performance catalysts. Transition metal nitrides and conductive polymers have been studied relatively less but are useful complimentarities. Precious metals and alloys generally possess virtues of both high activity and favorable stability but disadvantages of cost and scarcity. From the review, it is clearly observed that one catalyst can work in both aqueous and nonaqueous electrolytes with different mechanisms. With regards to energy density, nonaqueous Li–air batteries present potential advantages over aqueous Zn–air batteries. With the increasing interest in nonaqueous Li–air batteries, nonaqueous oxygen catalysis will be a research focus for metal–air batteries. Although most of the previous electrocatalysts were originally developed for aqueous systems, such as fuel cells and Zn–air batteries, they could provide guidance for the design and development of oxygen catalysts for Li–air batteries due to the similarity between both systems. However, several challenges also exist for aqueous to nonaqueous systems, which are discussed in the latter sections of this review in an attempt to sum up the research advances and efforts, great potentials and huge challenges that coexist in this field.

In contrast to fuel cell applications, where only the properties for oxygen reduction are important, the catalytic behavior for oxygen evolution is one of the major challenges in rechargeable metal–air batteries, especially in Li–air batteries because of the electrochemical decomposition of the solid lithium peroxide product, which involves large anodic polarization even at a moderate current density at very high discharge capacities. Lowering the overpotential during discharge and charge is of prime importance in order to avoid carbon corrosion and to diminish electrolyte oxidation. The development of bifunctional catalysts will be a future research direction to simultaneously improve the ORR and OER activities. Bifunctional catalysts have been studied for the application of secondary zinc–air batteries in aqueous media, but little has been done on Li–O_2 cells. Research on bifunctional oxygen catalysts has mainly focused on mixed-metal oxides of the spinel, perovskite, and pyrochlore structures in alkaline solution. The combination of theoretical and experimental studies afforded by recent techniques has improved the understanding of their function, allowing new findings and breakthroughs to be made. Non-precious bifunctional electrocatalysts are urgently required for Li–air batteries to promote the formation–decomposition of Li_2O_2 exclusively, and to suppress the formation of other lithium compounds. By varying the physicochemical parameters of the catalysts such as composition, valence state, phase, structure, defects, morphology, size, surface area, conductivity, and so on, the tuning of the intrinsic catalytic activity and the increase in the density of the active sites can be achieved by using different synthesis technologies. On the other hand, nanostructured carbonaceous materials modified with doping or metal–nitrogen complexes are promising abundant and cheap catalysts applicable to oxygen catalysis and deserve further research and improvement.

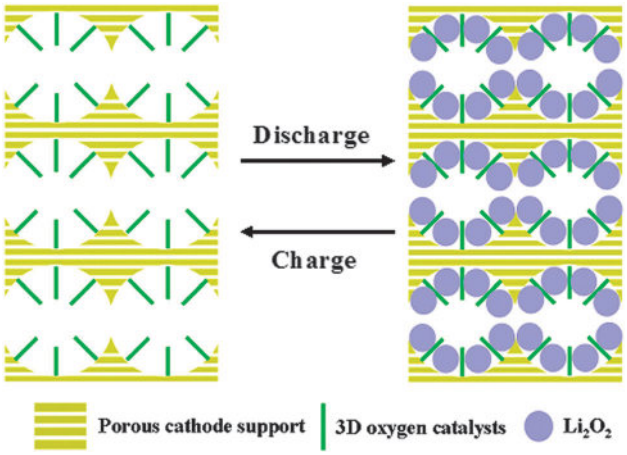

Fig. 35 Ideal structure model of the air cathode for rechargeable non-aqueous Li–air batteries.

The rational design of the electrode structure is also important for the exertion of catalysts and the improvement of the energy conversion efficiency. The electrochemical reactions in metal–air batteries involve the diffusion of oxygen and the precipitation of discharged products. The porous structure and the catalyst distribution in the air electrode require careful optimization to realize the rapid transportation of reactants. Recently, the free-standing type or integrative air electrodes have been put forward by us and others.[117,193,194,408] A mold of the ideal cathode structure is illustrated in Fig. 35. It has several features: firstly, the air cathode has a hierarchically porous structure including macropores, mesopores and micropores from the cathode support, which facilitates the O_2 diffusion, electrolyte wetting, and mass transport of all reactants; secondly, nanostructured catalysts (free-standing nanowires or nanosheets) are *in situ* uniformly grown on a porous support, which would realize the three-dimensional catalytic network; the obvious advantage of combining the above features is the avoidance of serious aggregation and the increased utilization of the active matter; finally, such novel electrodes as a whole are directly synthesized with or without collectors and are free of the conventional complex preparation processes of cathodes, which could be great benefit to large scale fabrication. As a typical example, very recently, we have successfully *in situ* synthesized

a free-standing honeycomb-like Pd-modified hollow spherical carbon electrode in carbon paper. It was found that the novel functional O_2 cathode exhibits the capability of tailoring the critical deposition behavior and morphology of the discharge product, which leads to superior battery performance with a high rate (5900 mA h g^{-1} at a current density of 1.5 A g^{-1}) and long cycling (100 cycles) for a nonaqueous Li–O_2 battery. Furthermore, our research also reveals that the rational design of the structure and composition could alleviate electrolyte decomposition compared with the conventional carbon cathode.[409] This work opens a new way to develop highly-efficient oxygen electrocatalysts and multi-functional air cathodes for Li–O_2 batteries.

The fundamental understanding of the oxygen reaction mechanisms during discharge and charge in different electrolytes, especially in nonaqueous electrolytes, for Li–air batteries is a prerequisite for the development of highly efficient, high-rate and long-life batteries. Various techniques should be used to explore *in situ* to directly probe the electrochemical reactions and gain further insights into the reaction mechanism, so as to help identify effective strategies for developing stable and reversible oxygen electrodes.[30,410–413] For example, using an *in situ* surface enhanced Raman spectroscopy (SERS) technique can gain significant insights into the reaction intermediates and products of the Li–O_2 redox chemistry,[59] and using *in situ* FTIR can analyze the decomposition process of the electrolyte.[75,76] *In situ* quantitative differential electrochemical mass spectrometry (DEMS) has been proved to be a very powerful tool for identifying the presence or absence of side-reactions in Li–air batteries. The quantitative evaluation of gas consumption and evolution provides critical data essential for proper analysis of the basic chemistry and, in particular, in the rechargeability of the batteries.[66,67] *In situ* XRD was developed recently to provide a simple and straightforward analytical method for simultaneously attaining chemical and quantified information on Li_2O_2 (discharge product) and byproducts.[414] With the chemical identification of the discharge product, the real-time acquisition of the Li_2O_2 XRD pattern allowed us to estimate the increasing and decreasing Li_2O_2 peak-area change, which revealed the rates of formation and decomposition of solid-state Li_2O_2 during discharge and recharge, respectively. Another useful technology is *in situ* ambient pressure X-ray photoelectron spectroscopy (APXPS), which was developed to directly visualize the formation and disappearance of Li–O_2 reaction products as a function of applied battery potential by utilizing the special all solid-state cell design, which provides numerous opportunities to gain mechanistic insights into air-based electrochemical reactions for efficient energy storage.[415] More recently, *in situ* TEM techniques have been applied to study the electrochemical oxidation of Li_2O_2 and considerable insights have been gained into the origin of the kinetic limitations that hinder the charging in Li–O_2 cells. Interestingly, it was found that the oxidation of electrochemically formed Li_2O_2 particles, supported on carbon nanotubes, occurs preferentially at the carbon/Li_2O_2 interface, suggesting that electron transport in Li_2O_2 ultimately limits the oxidation kinetics at high rates or overpotentials.[416] *In situ* techniques provide a powerful approach for exploring the fundamental nanoscale processes, which impact the cell-level performance. This will provide an improved understanding of the mechanisms of the ORR and OER in the metal–air batteries.

Acknowledgements

This work was financially supported by the 100 Talents Programme of The Chinese Academy of Sciences, the National Program on Key Basic Research Project of China (973 Program, Grant No. 2012CB215500), the National Natural Science Foundation of China (Grant No. 20921002, 21101147 and 21203176), and the Foundation for Innovative Research Groups of the National Natural Science Foundation of China (Grant No. 20921002).

Notes and references

1 M. Armand and J. M. Tarascon, *Nature*, 2008, **451**, 652.
2 P. G. Bruce, S. A. Freunberger, L. J. Hardwick and J. M. Tarascon, *Nat. Mater.*, 2012, **11**, 19.
3 P. G. Bruce, B. Scrosati and J. M. Tarascon, *Angew. Chem., Int. Ed.*, 2008, **47**, 2930.
4 R. Black, B. Adams and L. F. Nazar, *Adv. Energy Mater.*, 2012, **2**, 801.
5 Y. Y. Liang, Y. G. Li, H. L. Wang and H. J. Dai, *J. Am. Chem. Soc.*, 2013, **135**, 2013.
6 S. Park, Y. Y. Shao, J. Liu and Y. Wang, *Energy Environ. Sci.*, 2012, **5**, 9331.
7 X. P. Gao and H. X. Yang, *Energy Environ. Sci.*, 2010, **3**, 174.
8 J. J. Wang, Y. L. Li and X. L. Sun, *Nano Energy*, 2013, **2**, 443.
9 F. T. Wagner, B. Lakshmanan and M. F. Mathias, *J. Phys. Chem. Lett.*, 2010, **1**, 2204.
10 B. Scrosati and J. Garche, *J. Power Sources*, 2010, **195**, 2419.
11 J. Wu, H. W. Park, A. Yu, D. Higgins and Z. W. Chen, *J. Phys. Chem. C*, 2012, **116**, 9427.
12 F. Cheng and J. Chen, *Chem. Soc. Rev.*, 2012, **41**, 2172.
13 J. S. Lee, S. T. Kim, R. Cao, N. S. Choi, M. Liu, K. T. Lee and J. Cho, *Adv. Energy Mater.*, 2011, **1**, 34.
14 E. Deiss, F. Holzer and O. Haas, *Electrochim. Acta*, 2002, **47**, 3995.
15 J. Goldstein, I. Brown and B. Koretz, *J. Power Sources*, 1999, **80**, 171.
16 X. G. Zhang, *J. Power Sources*, 2006, **163**, 591.
17 G. Girishkumar, B. McCloskey, A. C. Luntz, S. Swanson and W. Wilcke, *J. Phys. Chem. Lett.*, 2010, **1**, 2193.
18 K. M. Abraham and Z. Jiang, *J. Electrochem. Soc.*, 1996, **143**, 1.
19 I. Kowalczk, J. Read and M. Salomon, *Pure Appl. Chem.*, 2007, **79**, 851.
20 S. J. Visco, B. D. Katz, Y. S. Nimon and L. C. D. Jonghe, *US Pat.*, 7282295, 2007.
21 S. J. Visco and Y. S. Nimon, *US Pat.*, 7645543, 2010.
22 S. Hasegawa, N. Imanishi, T. Zhang, J. Xie, A. Hirano, Y. Takeda and O. Yamamoto, *J. Power Sources*, 2009, **189**, 371.

23 T. Zhang, N. Imanishi, Y. Shimonishi, A. Hirano, Y. Takeda, O. Yamamoto and N. Sammes, *Chem. Commun.*, 2010, **46**, 1661.
24 Y. G. Wang and H. S. Zhou, *Chem. Commun.*, 2010, **46**, 6305.
25 A. Kraytsberg and Y. Ein-Eli, *Nano Energy*, 2013, **2**, 468.
26 Y. Y. Shao, S. Park, J. Xiao, J. G. Zhang, Y. Wang and J. Liu, *ACS Catal.*, 2012, **2**, 844.
27 Y. Y. Shao, F. Ding, J. Xiao, J. Zhang, W. Xu, S. Park, J. G. Zhang, Y. Wang and J. Liu, *Adv. Funct. Mater.*, 2013, **23**, 987.
28 M. Park, H. Sun, H. Lee, J. Lee and J. Cho, *Adv. Energy Mater.*, 2012, **2**, 780.
29 R. G. Cao, J. S. Lee, M. L. Liu and J. Cho, *Adv. Energy Mater.*, 2012, **2**, 816.
30 Y. C. Lu, B. M. Gallant, D. G. Kwabi, J. R. Harding, R. R. Mitchell, M. S. Whittingham and Y. Shao-Horn, *Energy Environ. Sci.*, 2013, **6**, 750.
31 F. J. Li, T. Zhang and H. S. Zhou, *Energy Environ. Sci.*, 2013, **6**, 1125.
32 V. Giordani, S. A. Freunberger, P. G. Bruce, J. M. Tarascon and D. Larcher, *Electrochem. Solid-State Lett.*, 2010, **13**, A180.
33 M. Casas-Cabanas, G. Binotto, D. Larcher, A. Lecup, V. Giordani and J. M. Tarascon, *Chem. Mater.*, 2009, **21**, 1939.
34 J. S. Spendelow and A. Wieckowshi, *Phys. Chem. Chem. Phys.*, 2007, **9**, 2654.
35 P. A. Christensen, A. Hamnett and D. Linares-Moya, *Phys. Chem. Chem. Phys.*, 2011, **13**, 5206.
36 W. Vielstich, A. Lamm and H. A. Gasteiger, *Handbook of Fuel Cells – Fundamentals, Technology and Applications*, Wiley, Chichester, 2003.
37 L. Jorisen, *J. Power Sources*, 2006, **155**, 23.
38 C. F. Zinola, A. J. Arvia, G. L. Estiu and E. A. Castro, *J. Phys. Chem.*, 1994, **98**, 7566.
39 J. Suntivich, H. A. Gasteiger, N. Yabuuchi, H. Nakanishi, J. B. Goodenough and Y. Shao-Horn, *Nat. Chem.*, 2011, **3**, 546.
40 P. Zhang, X. F. Chen, J. S. Lian and Q. Jiang, *J. Phys. Chem. C*, 2012, **116**, 17572.
41 W. Gao, X. F. Chen, J. C. Li and Q. Jiang, *J. Phys. Chem. C*, 2010, **114**, 1148.
42 W. Liu, Y. H. Zhao, R. Q. Zhang, Y. Li, E. J. Lavernia and Q. Jiang, *ChemPhysChem*, 2009, **10**, 3295.
43 P. Rasiyah and A. C. C. Tseung, *J. Electrochem. Soc.*, 1984, **131**, 803.
44 F. R. McLarnon and E. J. Cairns, *J. Electrochem. Soc.*, 1991, **138**, 645.
45 R. Renuka, S. Ramamurthy and L. Srinivasan, *J. Power Sources*, 2000, **89**, 70.
46 I. Arise, Y. Fukunaka and F. R. McLarnon, *J. Electrochem. Soc.*, 2006, **153**, A69.
47 M. E. Peover and B. S. White, *Electrochim. Acta*, 1966, **11**, 1061.
48 D. Vasudevan and H. Wendt, *J. Electroanal. Chem.*, 1995, **392**, 69.
49 C. Shi and F. C. Anson, *J. Electroanal. Chem.*, 2000, **484**, 69.
50 M. M. Islam and T. Ohsaka, *J. Phys. Chem. C*, 2008, **112**, 1269.
51 X. J. Huang, E. I. Rogers, C. Hardacre and R. G. Compton, *J. Phys. Chem. B*, 2009, **113**, 8953.
52 J. Read, *J. Electrochem. Soc.*, 2002, **149**, A1190.
53 T. Ogasawara, A. Debart, M. Holzapfel, P. Novak and P. G. Bruce, *J. Am. Chem. Soc.*, 2006, **128**, 1390.
54 C. O. Laoire, S. Mukerjee, K. M. Abraham, E. J. Plichta and M. A. Hendrickson, *J. Phys. Chem. C*, 2009, **113**, 20127.
55 C. O. Laoire, S. Mukerjee, K. M. Abraham, E. J. Plichta and M. A. Hendrickson, *J. Phys. Chem. C*, 2010, **114**, 9178.
56 C. J. Allen, J. Hwang, R. Kautz, S. Mukerjee, E. J. Plichta, M. A. Hendrickson and K. M. Abraham, *J. Phys. Chem. C*, 2012, **116**, 20755.
57 P. Hartmann, C. L. Bender, M. Vracar, A. K. Dürr, A. Garsuch, J. Janek and P. Adelhelm, *Nat. Mater.*, 2013, **12**, 228.
58 X. D. Ren and Y. Y. Wu, *J. Am. Chem. Soc.*, 2013, **135**, 2923.
59 Y. C. Lu, H. A. Gasteiger, E. Crumlin, R. McGuire and Y. Shao-Horn, *J. Electrochem. Soc.*, 2010, **157**, A1016.
60 D. T. Sawyer, G. Chlericato, C. T. Angelis, E. J. Nanni and T. Tsuchiya, *Anal. Chem.*, 1982, **54**, 1720.
61 D. T. Sawyer and J. L. Roberts, *J. Electroanal. Chem.*, 1966, **12**, 90.
62 Z. Q. Peng, S. A. Freunberger, L. J. Hardwick, Y. H. Chen, V. Giordani, F. Barde, P. Novak, D. Graham, J. M. Tarascon and P. G. Bruce, *Angew. Chem., Int. Ed.*, 2011, **50**, 6351.
63 S. Zhang and J. Read, *J. Power Sources*, 2011, **196**, 2867.
64 Y. C. Lu, H. A. Gasteiger, M. C. Parent, V. Chiloyan and Y. Shao-Horn, *Electrochem. Solid-State Lett.*, 2010, **13**, A69.
65 Y. C. Lu and Y. Shao-Horn, *J. Phys. Chem. Lett.*, 2013, **4**, 93.
66 B. D. McCloskey, D. S. Bethune, R. M. Shelby, G. Girishkumar and A. C. Luntz, *J. Phys. Chem. Lett.*, 2011, **2**, 1161.
67 B. D. McCloskey, R. Scheffler, A. Speidel, D. S. Bethune, R. M. Shelby and A. C. Luntz, *J. Am. Chem. Soc.*, 2011, **133**, 18038.
68 J. H. Lee, R. Black, G. Popov, E. Pomerantseva, F. Nan, G. A. Botton and L. F. Nazar, *Energy Environ. Sci.*, 2012, **5**, 9558.
69 S. H. Oh and L. F. Nazar, *Adv. Energy Mater.*, 2012, **2**, 903.
70 J. R. Harding, Y. C. Lu, Y. Tsukada and Y. Shao-Horn, *Phys. Chem. Chem. Phys.*, 2012, **14**, 10540.
71 B. D. McCloskey, A. Speidel, R. Scheffler, D. C. Miller, V. Viswanathan, J. S. Hummelshøj, J. K. Nørskov and A. C. Luntz, *J. Phys. Chem. Lett.*, 2012, **3**, 997.
72 B. D. McCloskey, D. S. Bethune, R. M. Shelby, T. Mori, R. Scheffler, A. Speidel, M. Sherwood and A. C. Luntz, *J. Phys. Chem. Lett.*, 2012, **3**, 3043.
73 K. C. Lau, L. A. Curtiss and J. Greeley, *J. Phys. Chem. C*, 2011, **115**, 23625.
74 X. H. Yang and Y. Y. Xia, *J. Solid State Electrochem.*, 2010, **14**, 109.
75 S. S. Zhang, D. Foster and J. Read, *J. Power Sources*, 2010, **195**, 1235.
76 C. O. Laoire, S. Mukerjee, E. J. Plichta, M. A. Hendrickson and K. M. Abraham, *J. Electrochem. Soc.*, 2011, **158**, A302.

77 V. Neburchilov, H. J. Wang, J. J. Martin and W. Qu, *J. Power Sources*, 2010, **195**, 1271.
78 F. Mizuno, S. Nakanishi, Y. Kotani, S. Yokoishi and H. Iba, *Electrochemistry*, 2010, **78**, 403.
79 S. A. Freunberger, Y. Chen, Z. Peng, J. M. Griffin, L. J. Hardwick, F. Bardé, P. Novák and P. G. Bruce, *J. Am. Chem. Soc.*, 2011, **133**, 8040.
80 S. A. Freunberger, Y. Chen, N. E. Drewett, L. J. Hardwick, F. Bardé and P. G. Bruce, *Angew. Chem., Int. Ed.*, 2011, **50**, 8609.
81 V. S. Bryantsev, V. Giordani, W. Walker, M. Blanco, S. Zecevic, K. Sasaki, J. Uddin, D. Addison and G. V. Chase, *J. Phys. Chem. A*, 2011, **115**, 12399.
82 R. Black, J. H. Lee, B. Adams, C. A. Mims and L. F. Nazar, *Angew. Chem., Int. Ed.*, 2013, **52**, 392.
83 P. Zółtowski, D. M. Dražic and L. Vorkapic, *J. Appl. Electrochem.*, 1973, **3**, 271.
84 L. Q. Mao, T. Sotomura, K. Nakatsu, N. Koshiba, D. Zhang and T. Ohsaka, *J. Electrochem. Soc.*, 2002, **149**, A504.
85 L. Q. Mao, D. Zhang, T. Sotomura, K. Nakatsu, N. Koshiba and T. Ohsaka, *Electrochim. Acta*, 2003, **48**, 1015.
86 F. Cheng, J. Shen, W. Ji, Z. Tao and J. Chen, *ACS Appl. Mater. Interfaces*, 2009, **1**, 460.
87 F. Cheng, Y. Su, J. Liang, Z. Tao and J. Chen, *Chem. Mater.*, 2010, **22**, 898.
88 Y. Gorlin, C. J. Chung, D. Nordlund, B. M. Clemens and T. F. Jaramillo, *ACS Catal.*, 2012, **2**, 2687.
89 K. L. Pickrahn, S. W. Park, Y. Gorlin, H. B. R. Lee, T. F. Jaramillo and S. F. Bent, *Adv. Energy Mater.*, 2012, **2**, 1269.
90 D. A. Tompsett, S. C. Parker, P. G. Bruce and M. S. Islam, *Chem. Mater.*, 2013, **25**, 536.
91 F. Cheng, T. Zhang, Y. Zhang, J. Du, X. Han and J. Chen, *Angew. Chem., Int. Ed.*, 2013, **52**, 2474.
92 P. Bezdicka, T. Grygar, B. Klápšte and J. Vondrák, *Electrochim. Acta*, 1999, **45**, 913.
93 B. Klápšte, J. Vondrák and J. Velická, *Electrochim. Acta*, 2002, **47**, 2365.
94 I. Roche, E. Chaînet, M. Chatenet and J. Vondrák, *J. Phys. Chem. C*, 2007, **111**, 1434.
95 I. Roche and K. Scott, *J. Appl. Electrochem.*, 2008, **39**, 197.
96 Y. Gorlin and T. F. Jaramillo, *J. Am. Chem. Soc.*, 2010, **132**, 13612.
97 Y. Gorlin, B. Lassalle-Kaiser, J. D. Benck, S. Gul, S. M. Webb, V. K. Yachandra, J. Yano and T. F. Jaramillo, *J. Am. Chem. Soc.*, 2013, **135**, 8525.
98 M. Hamdani, R. N. Singh and P. Chartier, *Int. J. Electrochem. Sci.*, 2010, **5**, 556.
99 A. J. Esswein, M. J. McMurdo, P. N. Ross, A. T. Bell and T. D. Tilley, *J. Phys. Chem. C*, 2009, **113**, 15068.
100 *Comprehensive Chemical Kinetics*, ed. R. G. Compton, Elsevier, 1987.
101 A. Restovic, E. Rios, S. Barbato, J. Ortiz and J. L. Gautier, *J. Electroanal. Chem.*, 2002, **522**, 141.
102 J. B. Xu, P. Gao and T. S. Zhao, *Energy Environ. Sci.*, 2012, **5**, 5333.
103 A. Debart, A. J. Paterson, J. L. Bao and P. G. Bruce, *Angew. Chem., Int. Ed.*, 2008, **47**, 4521.
104 A. K. Thapa, K. Saimen and T. Ishihara, *Electrochem. Solid-State Lett.*, 2010, **13**, A165.
105 Y. G. Wang and H. S. Zhou, *J. Power Sources*, 2010, **195**, 358.
106 H. Cheng and K. Scott, *J. Power Sources*, 2010, **195**, 1370.
107 A. K. Thapa, Y. Hidaka, H. Hagiwara, S. Ida and T. Ishihara, *J. Electrochem. Soc.*, 2011, **158**, A1483.
108 G. Q. Zhang, J. P. Zheng, R. Liang, C. Zhang, B. Wang, M. Au, M. Hendrickson and E. J. Plichta, *J. Electrochem. Soc.*, 2011, **158**, A822.
109 E. M. Benbow, S. P. Kelly, L. Zhao, J. W. Reutenauer and S. L. Suib, *J. Phys. Chem. C*, 2011, **115**, 22009.
110 T. T. Truong, Y. Z. Liu, Y. Ren, L. Trahey and Y. G. Sun, *ACS Nano*, 2012, **6**, 8067.
111 L. L. Zhang, X. B. Zhang, Z. L. Wang, J. J. Xu, D. Xu and L. M. Wang, *Chem. Commun.*, 2012, **48**, 7598.
112 O. Oloniyo, S. Kumar and K. Scott, *J. Electron. Mater.*, 2012, **41**, 921.
113 S. Ida, A. K. Thapa, Y. Hidaka, Y. Okamoto, M. Matsuka, H. Hagiwara and T. Ishihara, *J. Power Sources*, 2012, **203**, 159.
114 J. K. Ngala, S. Alia, A. Dobley, V. M. B. Crisostomo and S. L. Suib, *Chem. Mater.*, 2007, **19**, 229.
115 L. Trahey, N. K. Karan, M. K. Y. Chan, J. Lu, Y. Ren, J. Greeley, M. Balasubramanian, A. K. Burrell, L. A. Curtiss and M. M. Thackeray, *Adv. Energy Mater.*, 2013, **3**, 75.
116 A. Debart, J. L. Bao, G. Armstrong and P. G. Bruce, *J. Power Sources*, 2007, **174**, 1177.
117 Y. M. Cui, Z. Y. Wen and Y. Liu, *Energy Environ. Sci.*, 2011, **4**, 4727.
118 T. Ishihara, A. K. Thapa, Y. Hidaka and S. Ida, *Electrochemistry*, 2012, **80**, 731.
119 Y. Cui, Z. Wen, S. Sun, Y. Lu and J. Jin, *Solid State Ionics*, 2012, **225**, 598.
120 E. Rios, J. L. Gautier, G. Poillerat and P. Chartier, *Electrochim. Acta*, 1998, **44**, 1491.
121 J. Ponce, J. L. Rehspringer, G. Poillerat and J. L. Gautier, *Electrochim. Acta*, 2001, **46**, 3373.
122 B. Cui, H. Lin, J. B. Li, X. Li, J. Yang and J. Tao, *Adv. Funct. Mater.*, 2008, **18**, 1440.
123 V. Nikolova, P. Iliev, K. Petrov, T. Vitanov, E. Zhecheva, R. Stoyanova, I. Valov and D. Stoychev, *J. Power Sources*, 2008, **185**, 727.
124 Y. G. Li, P. Hasin and Y. Y. Wu, *Adv. Mater.*, 2010, **22**, 1926.
125 B. G. Lu, D. X. Cao, P. Wang, G. L. Wang and Y. Y. Gao, *Int. J. Hydrogen Energy*, 2011, **36**, 72.
126 F. Y. Cheng, J. Shen, B. Peng, Y. D. Pan, Z. L. Tao and J. Chen, *Nat. Chem.*, 2010, **3**, 79.
127 J. Landon, E. Demeter, N. Inoglu, C. Keturakis, I. E. Wachs, R. Vasic, A. I. Frenkel and J. R. Kitchin, *ACS Catal.*, 2012, **2**, 1793.
128 J. Du, Y. D. Pan, T. R. Zhang, X. P. Han, F. Y. Cheng and J. Chen, *J. Mater. Chem.*, 2012, **22**, 15812.
129 D. U. Lee, B. J. Kim and Z. W. Chen, *J. Mater. Chem. A*, 2013, **1**, 4754.
130 J. L. Gautier, J. F. Marco, M. Gracia, J. R. Gancedo, V. G. Guadarrama, H. N. Cong and P. Chartier, *Electrochim. Acta*, 2002, **48**, 119.

131 H. N. Cong, V. G. Guadarrama, J. L. Gautier and P. Chartier, *Electrochim. Acta*, 2003, **48**, 2389.
132 R. N. Singh, B. Lal and M. Malviya, *Electrochim. Acta*, 2004, **49**, 4605.
133 L. X. Zhang, S. L. Zhang, K. J. Zhang, G. J. Xu, X. He, S. M. Dong, Z. H. Liu, C. S. Huang, L. Gu and G. L. Cui, *Chem. Commun.*, 2013, **49**, 3540.
134 H. M. Zhang, Y. Shimizu, Y. Teraoka, N. Miura and N. Yamazoe, *J. Catal.*, 1990, **121**, 432.
135 H. Tanaka and M. Misono, *Curr. Opin. Solid State Mater. Sci.*, 2001, **5**, 381.
136 L. Swette, N. Kackley and S. A. McCatty, *J. Power Sources*, 1991, **36**, 323.
137 A. M. Kannan, A. K. Shukla and S. Sathyanarayana, *J. Power Sources*, 1989, **25**, 141.
138 L. Swette and N. Kackley, *J. Power Sources*, 1990, **29**, 423.
139 J. Sunarso, A. A. J. Torriero, W. Zhou, P. C. Howlett and M. Forsyth, *J. Phys. Chem. C*, 2012, **116**, 5827.
140 Y. Shimizu, K. Uemura, H. Matsuda, N. Miura and N. Yamazoe, *J. Electrochem. Soc.*, 1990, **137**, 3430.
141 Y. Shimizu, H. Matsuda, N. Miura and N. Yamazoe, *Chem. Lett.*, 1992, 1033.
142 C. K. Lee, K. A. Striebel, F. R. Mclarnon and E. J. Cairns, *J. Electrochem. Soc.*, 1997, **144**, 3801.
143 S. Muller, F. Holzer and O. Haas, *J. Appl. Electrochem.*, 1998, **28**, 895.
144 N. L. Wu, W. R. Liu and S. J. Su, *Electrochim. Acta*, 2003, **48**, 1567.
145 N. A. Merino, B. P. Barbero, P. Eloy and L. E. Cadus, *Appl. Surf. Sci.*, 2006, **253**, 1489.
146 A. Kahoul, A. Hammouche, G. Poillerat and R. W. De Doncker, *Catal. Today*, 2004, **89**, 287.
147 S. Malkhandi, B. Yang, A. K. Manohar, A. Manivannan, G. K. Surya Prakash and S. R. Narayanan, *J. Phys. Chem. Lett.*, 2012, **3**, 967.
148 Y. M. Chang, P. W. Wu, C. Y. Wu, Y. F. Hsieh and J. Y. Chen, *Electrochem. Solid-State Lett.*, 2008, **11**, B47.
149 Y. M. Chang, Y. C. Hsieh, P. W. Wu, C. H. Lai and T. Y. Chang, *Mater. Lett.*, 2008, **62**, 4220.
150 Y. M. Chang, P. W. Wu, C. Y. Wu and Y. C. Hsieh, *J. Power Sources*, 2009, **189**, 1003.
151 Y. M. Chang, Y. F. Chang, P. W. Wu, C. Y. Wu and P. Lin, *J. Electrochem. Soc.*, 2010, **157**, B900.
152 X. X. Li, W. Qu, J. J. Zhang and H. J. Wang, *J. Electrochem. Soc.*, 2011, **158**, A597.
153 S. X. Zhuang, K. L. Huang, C. H. Huang, H. X. Huang, S. Q. Liu and M. Fan, *J. Power Sources*, 2011, **196**, 4019.
154 K. Miyazaki, K. Nishio, T. Abe, K. Suto, Y. Kotani, S. Naknishi and Z. Ogumi, *Electrochemistry*, 2012, **80**, 728.
155 M. Komo, A. Hagiwara, S. Taminato, M. Hirayama and R. Kanno, *Electrochemistry*, 2012, **80**, 834.
156 H. Ohkuma, I. Uechi, N. Imanishi, A. Hirano, Y. Takeda and O. Yamamoto, *J. Power Sources*, 2013, **223**, 319.
157 S. Velraj and J. H. Zhu, *J. Power Sources*, 2013, **227**, 48.
158 W. Yang, J. Salim, S. Li, C. W. Sun, L. Q. Chen, J. B. Goodenough and Y. Kim, *J. Mater. Chem.*, 2012, **22**, 18902.
159 X. P. Han, T. R. Zhang, J. Du, F. Y. Cheng and J. Chen, *Chem. Sci.*, 2013, **4**, 368.
160 Y. Wang and H. P. Cheng, *J. Phys. Chem. C*, 2013, **117**, 2106.
161 W. G. Hardin, D. A. Slanac, X. Q. Wang, S. Dai, K. P. Johnston and K. J. Stevenson, *J. Phys. Chem. Lett.*, 2013, **4**, 1254.
162 Y. Chen, W. C. Jung, Z. H. Cai, J. J. Kim, H. L. Tuller and B. Yildiz, *Energy Environ. Sci.*, 2012, **5**, 7979.
163 M. Yuasa, H. Imamura, M. Nishida, T. Kida and K. Shimanoe, *Electrochem. Commun.*, 2012, **24**, 50.
164 J. Suntivich, K. J. May, H. A. Gasteiger, J. B. Goodenough and Y. Shao-Horn, *Science*, 2011, **334**, 1383.
165 Y. Li, J. G. Cheng, J. Song, J. A. Alonso, M. T. Fernandez-Díaz and J. B. Goodenough, *Chem. Mater.*, 2012, **24**, 4114.
166 M. Cheriti and A. Kahoul, *Mater. Res. Bull.*, 2012, **47**, 135.
167 T. Takeguchi, T. Yamanaka, H. Takahashi, H. Watanabe, T. Kuroki, H. Nakanishi, Y. Orikasa, Y. Uchimoto, H. Takano, N. Ohguri, M. Matsuda, T. Murota, K. Uosaki and W. Ueda, *J. Am. Chem. Soc.*, 2013, **135**, 11125.
168 Z. H. Fu, X. J. Lin, T. Huang and A. S. Yu, *J. Solid State Electrochem.*, 2012, **16**, 1447.
169 K. N. Jung, J. I. Lee, W. B. Im, S. Yoon, K. H. Shin and J. W. Lee, *Chem. Commun.*, 2012, **48**, 9406.
170 Y. L. Zhao, L. Xu, L. Q. Mai, C. H. Han, Q. Y. An, X. Xu, X. Liu and Q. J. Zhang, *Proc. Natl. Acad. Sci. U. S. A.*, 2012, **109**, 19569.
171 J. J. Xu, D. Xu, Z. L. Wang, H. G. Wang, L. L. Zhang and X. B. Zhang, *Angew. Chem., Int. Ed.*, 2013, **52**, 3887.
172 H. S. Horowitz, J. M. Longo and H. H. Horowitz, *J. Electrochem. Soc.*, 1983, **130**, 1851.
173 J. B. Goodenough, R. Manoharan and M. Paranthaman, *J. Am. Chem. Soc.*, 1990, **112**, 2076.
174 J. Prakash, D. A. Tryk, W. Aldred and E. B. Yeager, *J. Appl. Electrochem.*, 1999, **29**, 1463.
175 T. Akazawa, Y. Inaguma, T. Katsumata, K. Hiraki and T. Takahashi, *J. Cryst. Growth*, 2004, **271**, 445.
176 S. H. Oh, R. Black, E. Pomerantseva, J. H. Lee and L. F. Nazar, *Nat. Chem.*, 2012, **4**, 1004.
177 S. H. Oh and L. F. Nazar, *Adv. Energy Mater.*, 2012, **2**, 903.
178 M. Mirzaeian and P. J. Hall, *Electrochim. Acta*, 2009, **54**, 7444.
179 X. H. Yang, P. He and Y. Y. Xia, *Electrochem. Commun.*, 2009, **11**, 1127.
180 M. Mirzaeian and P. J. Hall, *J. Power Sources*, 2010, **195**, 6817.
181 C. Tran, X. Q. Yang and D. Y. Qu, *J. Power Sources*, 2010, **195**, 2057.
182 G. O. Shitta-Bey, M. Mirzaeian and P. J. Hall, *J. Electrochem. Soc.*, 2012, **159**, A315.
183 C. Tran, J. Kafle, X. Q. Yang and D. Y. Qu, *Carbon*, 2011, **49**, 1266.
184 X. Huang, Z. Y. Zeng, Z. X. Fan, J. Q. Liu and H. Zhang, *Adv. Mater.*, 2012, **24**, 5979.
185 X. Huang, X. Y. Qi, F. Boey and H. Zhang, *Chem. Soc. Rev.*, 2012, **41**, 666.

186 S. Nardecchia, D. Carriazo, M. L. Ferrer, M. C. Gutiérrez and F. D. Monte, *Chem. Soc. Rev.*, 2013, **42**, 794.
187 E. Yoo and H. S. Zhou, *ACS Nano*, 2011, **5**, 3020.
188 Y. L. Li, J. J. Wang, X. F. Li, D. F. Geng, R. Y. Li and X. L. Sun, *Chem. Commun.*, 2011, **47**, 9438.
189 B. Sun, B. Wang, D. W. Su, L. D. Xiao, H. Ahn and G. X. Wang, *Carbon*, 2012, **50**, 727.
190 J. Xiao, D. H. Mei, X. L. Li, W. Xu, D. Y. Wang, G. L. Graff, W. D. Bennett, Z. M. Nie, L. V. Saraf, I. A. Aksay, J. Liu and J. G. Zhang, *Nano Lett.*, 2011, **11**, 5071.
191 V. Etacheri, D. Sharon, A. Garsuch, M. Afri, A. A. Frimer and D. Aurbach, *J. Mater. Chem. A*, 2013, **1**, 5021.
192 X. J. Lin, L. Zhou, T. Huang and A. S. Yu, *J. Mater. Chem. A*, 2013, **1**, 1239.
193 Z. L. Wang, D. Xu, J. J. Xu, L. L. Zhang and X. B. Zhang, *Adv. Funct. Mater.*, 2012, **22**, 3699.
194 R. R. Mitchell, B. M. Gallant, C. V. Thompson and Y. Shao-Horn, *Energy Environ. Sci.*, 2011, **4**, 2952.
195 H. D. Lim, K. Y. Park, H. Song, E. Y. Jang, H. Gwon, J. Kim, Y. H. Kim, M. D. Lima, R. O. Robles, X. Lepró, R. H. Baughman and K. Kang, *Adv. Mater.*, 2013, **25**, 1348.
196 Y. G. Wang and H. S. Zhou, *Energy Environ. Sci.*, 2011, **4**, 1704.
197 R. A. Sidik and A. B. Anderson, *J. Phys. Chem. B*, 2006, **110**, 1787.
198 G. Liu, X. G. Li, P. Ganesan and B. N. Popov, *Appl. Catal., B*, 2009, **93**, 156.
199 Y. F. Tang, B. L. Allen, D. R. Kauffman and A. Star, *J. Am. Chem. Soc.*, 2009, **131**, 13200.
200 S. Kundu, T. C. Nagaiah, W. Xia, Y. M. Wang, S. V. Dommele, J. H. Bitter, M. Santa, G. Grundmeier, M. Bron, W. Schuhmann and M. Muhler, *J. Phys. Chem. C*, 2009, **113**, 14302.
201 K. P. Gong, F. Du, Z. H. Xia, M. Durstock and L. M. Dai, *Science*, 2009, **323**, 760.
202 P. Zhang, J. S. Lian and Q. Jiang, *Phys. Chem. Chem. Phys.*, 2012, **14**, 11715.
203 L. T. Qu, Y. Liu, J. B. Baek and L. M. Dai, *ACS Nano*, 2010, **4**, 1321.
204 R. L. Liu, D. Q. Wu, X. L. Feng and K. Mullen, *Angew. Chem., Int. Ed.*, 2010, **49**, 2565.
205 W. Xiong, F. Du, Y. Liu, A. Perez, Jr., M. Supp, T. S. Ramakrishnan, L. M. Dai and L. Jiang, *J. Am. Chem. Soc.*, 2010, **132**, 15839.
206 Y. Y. Shao, S. Zhang, M. H. Engelhard, G. S. Li, G. C. Shao, Y. Wang, J. Liu, I. A. Aksayc and Y. H. Lin, *J. Mater. Chem.*, 2010, **20**, 7491.
207 S. B. Yang, X. L. Feng, X. C. Wang and K. Mullen, *Angew. Chem., Int. Ed.*, 2011, **50**, 5339.
208 S. Shanmugam and T. Osaka, *Chem. Commun.*, 2011, **47**, 4463.
209 D. S. Geng, Y. Chen, Y. G. Chen, Y. L. Li, R. Y. Li, X. L. Sun, S. Y. Ye and S. Knights, *Energy Environ. Sci.*, 2011, **4**, 760.
210 H. Li, H. Liu, Z. Jong, W. Qu, D. S. Geng, X. L. Sun and H. J. Wang, *Int. J. Hydrogen Energy*, 2011, **36**, 2258.
211 Y. J. Qiu, J. Yua, T. N. Shi, X. S. Zhou, X. D. Bai and J. Y. Huang, *J. Power Sources*, 2011, **196**, 9862.
212 H. Kim, K. Lee, S. I. Woo and Y. Jung, *Phys. Chem. Chem. Phys.*, 2011, **13**, 17505.
213 T. Sharifi, G. Z. Hu, X. E. Jia and T. Wagberg, *ACS Nano*, 2012, **6**, 8904.
214 S. Chen, J. Y. Bi, Y. Zhao, L. J. Yang, C. Zhang, Y. W. Ma, Q. Wu, X. Z. Wang and Z. Hu, *Adv. Mater.*, 2012, **24**, 5593.
215 Y. Q. Sun, C. Li and G. Q. Shi, *J. Mater. Chem.*, 2012, **22**, 12810.
216 S. Ni, Z. Y. Li and J. L. Yang, *Nanoscale*, 2012, **4**, 1184.
217 P. Chen, T. Y. Xiao, Y. H. Qian, S. S. Li and S. H. Yu, *Adv. Mater.*, 2013, **25**, 3192.
218 D. Higgins, Z. Chen, D. U. Lee and Z. W. Chen, *J. Mater. Chem. A*, 2013, **1**, 2639.
219 S. M. Zhua, Z. Chen, B. Li, D. Higgins, H. J. Wang, H. Li and Z. W. Chen, *Electrochim. Acta*, 2011, **56**, 5080.
220 L. J. Yang, S. J. Jiang, Y. Zhao, L. Zhu, S. Chen, X. Z. Wang, Q. Wu, J. Ma, Y. W. Ma and Z. Hu, *Angew. Chem., Int. Ed.*, 2011, **50**, 7132.
221 D. S. Yang, D. Bhattacharjya, S. Inamdar, J. Park and J. S. Yu, *J. Am. Chem. Soc.*, 2012, **134**, 16127.
222 Z. Yang, Z. Yao, G. F. Li, G. Y. Fang, H. G. Nie, Z. Liu, X. M. Zhou, X. A. Chen and S. M. Huang, *ACS Nano*, 2012, **6**, 205.
223 S. Y. Wang, E. Iyyamperumal, A. Roy, Y.H. Xue, D. S. Yu and L. M. Dai, *Angew. Chem., Int. Ed.*, 2011, **50**, 11756.
224 S. Y. Wang, L. P. Zhang, Z. H. Xia, A. Roy, D. W. Chang, J. B. Baek and L. M. Dai, *Angew. Chem., Int. Ed.*, 2012, **51**, 4209.
225 E. Iyyamperumal, S. Y. Wang and L. M. Dai, *ACS Nano*, 2012, **6**, 5259.
226 D. S. Yu, Y. H. Xue and L. M. Dai, *J. Phys. Chem. Lett.*, 2012, **3**, 2863.
227 J. Liang, Y. Jiao, M. Jaroniec and S. Z. Qiao, *Angew. Chem., Int. Ed.*, 2012, **51**, 11496.
228 R. Silva, D. Voiry, M. Chhowalla and T. Asefa, *J. Am. Chem. Soc.*, 2013, **135**, 7823.
229 C. H. Choi, S. H. Park and S. I. Woo, *ACS Nano*, 2012, **6**, 7084.
230 Y. Zhao, L. J. Yang, S. Chen, X. Z. Wang, Y. W. Ma, Q. Wu, Y. F. Jiang, W. J. Qian and Z. Hu, *J. Am. Chem. Soc.*, 2013, **135**, 1201.
231 Y. Zheng, Y. Jiao, L. Ge, M. Jaroniec and S. Z. Qiao, *Angew. Chem., Int. Ed.*, 2013, **52**, 3110.
232 W. Liu, Y. H. Zhao, Y. Li, Q. Jiang and E. J. Lavernia, *J. Phys. Chem. C*, 2009, **113**, 2028.
233 Z. M. Ao, J. Yang, S. Li and Q. Jiang, *Chem. Phys. Lett.*, 2008, **461**, 276.
234 Z. M. Ao, Q. Jiang, R. Q. Zhang, T. T. Tan and S. Li, *J. Appl. Phys.*, 2009, **105**, 074307.
235 Z. W. Zhang, W. T. Zheng and Q. Jiang, *Int. J. Hydrogen Energy*, 2012, **37**, 5090.
236 E. H. Song, Z. Wen and Q. Jiang, *J. Phys. Chem. C*, 2011, **115**, 3678.
237 P. Kichambare, J. Kumar, S. Rodrigues and B. Kumar, *J. Power Sources*, 2011, **196**, 3310.
238 Y. L. Li, J. J. Wang, X. F. Li, J. Liu, D. S. Geng, J. L. Yang, R. Y. Li and X. L. Sun, *Electrochem. Commun.*, 2011, **13**, 668.

239 Y. l. Li, J. J. Wang, X. F. Li, D. S. Geng, M. N. Banis, R. Y. Li and X. L. Sun, *Electrochem. Commun.*, 2012, **18**, 12.
240 Y. L. Li, J. J. Wang, X. F. Li, D. S. Geng, M. N. Banis, Y. J. Tang, D. N. Wang, R. Y. Li, T. K. Sham and X. L. Sun, *J. Mater. Chem.*, 2012, **22**, 20170.
241 H. L. Wang and H. J. Dai, *Chem. Soc. Rev.*, 2013, **42**, 3088.
242 Y. M. Tan, C. F. Xu, G. X. Chen, X. L. Fang, N. F. Zheng and Q. J. Xie, *Adv. Funct. Mater.*, 2012, **22**, 4584.
243 D. U. Lee, B. J. Kim and Z. W. Chen, *J. Mater. Chem. A*, 2013, **1**, 4754.
244 S. Guo, S. Zhang, L. Wu and S. Sun, *Angew. Chem., Int. Ed.*, 2012, **51**, 11770.
245 J. S. Lee, G. S. Park, H. I. Lee, S. T. Kim, R. G. Cao, M. L. Liu and J. Cho, *Nano Lett.*, 2011, **11**, 5362.
246 J. S. Lee, T. Lee, H. K. Song, J. Cho and B. S. Kim, *Energy Environ. Sci.*, 2011, **4**, 4148.
247 H. L. Wang, Y. Y. Liang, Y. G. Li and H. J. Dai, *Angew. Chem., Int. Ed.*, 2011, **50**, 10969.
248 Y. G. Li, H. L. Wang, L. M. Xie, Y. Y. Liang, G. S. Hong and H. J. Dai, *J. Am. Chem. Soc.*, 2011, **133**, 7296.
249 Y. Y. Liang, Y. G. Li, H. L. Wang, J. G. Zhou, J. Wang, T. Regier and H. J. Dai, *Nat. Mater.*, 2011, **10**, 780.
250 Y. Y. Liang, H. L. Wang, P. Diao, W. Chang, G. S. Hong, Y. G. Li, M. Gong, L. M. Xie, J. G. Zhou, J. Wang, T. Z. Regier, F. Wei and H. J. Dai, *J. Am. Chem. Soc.*, 2012, **134**, 15849.
251 Y. Y. Liang, H. L. Wang, J. G. Zhou, Y. G. Li, J. Wang, T. Regier and H. J. Dai, *J. Am. Chem. Soc.*, 2012, **134**, 3517.
252 J. Feng, Y. Y. Liang, H. L. Wang, Y. G. Li, B. Zhang, J. G. Zhou, J. Wang, T. Regier and H. J. Dai, *Nano Res.*, 2012, **5**, 718.
253 Z. S. Wu, S. B. Yang, Y. Sun, K. Parvez, X. L. Feng and K. Mullen, *J. Am. Chem. Soc.*, 2012, **134**, 9082.
254 Z. Chen, A. P. Yu, D. Higgins, H. Li, H. J. Wang and Z. W. Chen, *Nano Lett.*, 2012, **12**, 1946.
255 H. L. Wang, Y. Yang, Y. Y. Liang, G. Y. Zheng, Y. G. Li, Y. Cui and H. J. Dai, *Energy Environ. Sci.*, 2012, **5**, 7931.
256 Y. Cao, Z. K. Wei, J. He, J. Zang, Q. Zhang, M. S. Zheng and Q. F. Dong, *Energy Environ. Sci.*, 2012, **5**, 9765.
257 J. X. Li, N. Wang, Y. Zhao, Y. H. Ding and L. H. Guan, *Electrochem. Commun.*, 2011, **13**, 698.
258 A. K. Thapa and T. Ishihara, *J. Power Sources*, 2011, **196**, 7016.
259 L. Wang, X. Zhao, Y. H. Lu, M. W. Xu, D. W. Zhang, R. S. Ruoff, K. J. Stevenson and J. B. Goodenough, *J. Electrochem. Soc.*, 2011, **158**, A1379.
260 K. N. Jung, J. I. Lee, S. Yoon, S. H. Yeon, W. Y. Chang, K. H. Shina and J. W. Lee, *J. Mater. Chem.*, 2012, **22**, 21845.
261 W. Y. Zhang, Y. Zeng, C. Xu, H. T. Tan, W. L. Liu, J. X. Zhu, N. Xiao, H. H. Hng, J. Ma, H. E. Hoster, R. Yazami and Q. Y. Yan, *RSC Adv.*, 2012, **2**, 8508.
262 C. N. Chervin, J. W. Long, N. L. Brandell, J. M. Wallace, N. W. Kucko and D. R. Rolison, *J. Power Sources*, 2012, **207**, 191.
263 H. W. Park, D. U. Lee, L. F. Nazar and Z. W. Chen, *J. Electrochem. Soc.*, 2013, **160**, A344.
264 Y. Yu, B. Zhang, Y. B. He, Z. D. Huang, S. W. Oh and J. K. Kim, *J. Mater. Chem. A*, 2013, **1**, 1163.
265 Y. Qin, J. Lu, P. Du, Z. H. Chen, Y. Ren, T. P. Wu, J. T. Miller, J. G. Wen, D. J. Miller, Z. C. Zhang and K. Amine, *Energy Environ. Sci.*, 2013, **6**, 519.
266 B. Sun, H. Liu, P. Munroe, H. Ahn and G. X. Wang, *Nano Res.*, 2012, **5**, 460.
267 T. H. Yoon and Y. J. Park, *Nanoscale Res. Lett.*, 2012, **7**, 28.
268 R. Jasinski, *Nature*, 1964, **201**, 1212.
269 F. Beck, *J. Appl. Electrochem.*, 1977, **7**, 239.
270 C. N. Shi and F. C. Anson, *Inorg. Chem.*, 1990, **29**, 4298.
271 B. Steiger and F. C. Anson, *Inorg. Chem.*, 1997, **36**, 4138.
272 E. Song, C. N. Shi and F. C. Anson, *Langmuir*, 1998, **14**, 4315.
273 G. I. Cardenas-Jiron, *J. Phys. Chem. A*, 2002, **106**, 3202.
274 K. M. Kadish, L. Fremond, Z. P. Ou, J. G. Shao, C. N. Shi, F. C. Anson, F. Burdet, C. P. Gros, J. M. Barbe and R. Guilard, *J. Am. Chem. Soc.*, 2005, **127**, 5625.
275 J. Chen, W. M. Zhang, D. Officer, G. F. Swiegers and G. G. Wallace, *Chem. Commun.*, 2007, 3353.
276 Z. Shi and J. J. Zhang, *J. Phys. Chem. C*, 2007, **111**, 7084.
277 R. Baker, D. P. Wilkinson and J. J. Zhang, *Electrochim. Acta*, 2008, **53**, 6906.
278 R. R. Chen, H. X. Li, D. Chu and G. F. Wang, *J. Phys. Chem. C*, 2009, **113**, 20689.
279 W. M. Li, A. P. Yu, D. C. Higgins, B. G. Llanos and Z. W. Chen, *J. Am. Chem. Soc.*, 2010, **132**, 17056.
280 R. G. Cao, R. Thapa, H. Kim, X. D. Xu, M. G. Kim, Q. Li, N. Park, M. L. Liu and J. Cho, *Nat. Commun.*, 2013, **4**, 2076.
281 C. Z. Zhang, R. Hao, H. Yin, F. Liu and Y. L. Hou, *Nanoscale*, 2012, **4**, 7326.
282 G. F. Dong, M. H. Huang and L. H. Guan, *Phys. Chem. Chem. Phys.*, 2012, **14**, 2557.
283 H. J. Tang, H. J. Yin, J. Y. Wang, N. L. Yang, D. Wang and Z. Y. Tang, *Angew. Chem., Int. Ed.*, 2013, **52**, 1.
284 Z. W. Chen, D. Higgins, A. P. Yu, L. Zhang and J. J. Zhang, *Energy Environ. Sci.*, 2011, **4**, 3167.
285 D. A. Scherson, S. L. Gupta, C. Fierro, E. B. Yeager, M. E. Kordesch, J. Eldridge, R. W. Hoffman and J. Blue, *Electrochim. Acta*, 1983, **28**, 1205.
286 D. Villers, X. J. Dard and J. P. Dodelet, *J. Electrochem. Soc.*, 2004, **151**, A1507.
287 C. Medard, M. Lefevre, J. P. Dodelet, F. Jaouen and G. Lindbergh, *Electrochim. Acta*, 2006, **51**, 3202.
288 F. Jaouen, F. Charreteur and J. P. Dodelet, *J. Electrochem. Soc.*, 2006, **153**, A689.
289 H. Tributsch, U. I. Koslowski and I. Dorbandt, *Electrochim. Acta*, 2008, **53**, 2198.
290 Z. H. Wen, S. Q. Ci, F. Zhang, X. L. Feng, S. M. Cui, S. Mao, S. L. Luo, Z. He and J. H. Chen, *Adv. Mater.*, 2012, **24**, 1399.
291 H. T. Chung, J. H. Won and P. Zelenay, *Nat. Commun.*, 2013, **4**, 1922.
292 D. H. Deng, L. Yu, X. Q. Chen, G. X. Wang, L. Jin, X. L. Pan, J. Deng, G. Q. Sun and X. H. Bao, *Angew. Chem., Int. Ed.*, 2013, **52**, 371.
293 E. H. Song, Z. Wen and Q. Jiang, *J. Phys. Chem. C*, 2011, **115**, 3678.

294 E. H. Song, J. M. Yan, J. S. Lian and Q. Jiang, *J. Phys. Chem. C*, 2012, **116**, 20342.
295 Q. G. Jiang, Z. M. Ao and Q. Jiang, *Phys. Chem. Chem. Phys.*, 2013, **15**, 10859.
296 W. Liu, Y. H. Zhao, J. Nguyen, Y. Li, Q. Jiang and E. J. Lavernia, *Carbon*, 2009, **47**, 3452.
297 Y. G. Li, W. Zhou, H. L. Wang, L. M. Xie, Y. Y. Liang, F. Wei, J. C. Idrobo, S. J. Pennycook and H. J. Dai, *Nat. Nanotechnol.*, 2012, **7**, 394.
298 X. X. Yuan, X. Zeng, H. J. Zhang, Z. F. Ma and C. Y. Wang, *J. Am. Chem. Soc.*, 2010, **132**, 1754.
299 M. Lefèvre, E. Proietti, F. Jaouen and J. P. Dodelet, *Science*, 2009, **324**, 71.
300 Z. Chen, J. Y. Choi, H. J. Wang, H. Li and Z. W. Chen, *J. Power Sources*, 2011, **196**, 3673.
301 K. Parvez, S. B. Yang, Y. Hernandez, A. Winter, A. Turchanin, X. L. Feng and K. Mullen, *ACS Nano*, 2012, **6**, 9541.
302 H. C. Huang, I. Shown, S. T. Chang, H. C. Hsu, H. Y. Du, M. C. Kuo, K. T. Wong, S. F. Wang, C. H. Wang, L. C. Chen and K. H. Chen, *Adv. Funct. Mater.*, 2012, **22**, 3500.
303 J. L. Qiao, L. Xua, L. Ding, L. Zhang, R. Baker, X. F. Dai and J. J. Zhang, *Appl. Catal., B*, 2012, **125**, 197.
304 X. F. Dai, J. L. Qiao, X. J. Zhou, J. J. Shi, P. Xu, L. Zhang and J. J. Zhang, *Int. J. Electrochem. Sci.*, 2013, **8**, 3160.
305 M. Yuasa, A. Yamaguchi, H. Itsuki, K. Tanaka, M. Yamamoto and K. Oyaizu, *Chem. Mater.*, 2005, **17**, 4278.
306 G. Wu, Z. W. Chen, K. Artyushkova, F. H. Garzon and P. Zelenay, *ECS Trans.*, 2008, **16**, 159.
307 J. M. Ziegelbauer, T. S. Olson, S. Pylypenko, F. Alamgir, C. Jaye, P. Atanassov and S. Mukerjee, *J. Phys. Chem. C*, 2008, **112**, 8839.
308 G. Wu, K. Artyushkova, M. Ferrandon, J. Kropf, D. Myers and P. Zelenay, *ECS Trans.*, 2009, **25**, 1299.
309 K. Lee, L. Zhang, H. Lui, R. Hui, Z. Shi and J. J. Zhang, *Electrochim. Acta*, 2009, **54**, 4704.
310 H. S. Liu, Z. Shi, J. L. Zhang, L. Zhang and J. J. Zhang, *J. Mater. Chem.*, 2009, **19**, 468.
311 X. X. Yuan, X. Zeng, H. J. Zhang, Z. F. Ma and C. Y. Wang, *J. Am. Chem. Soc.*, 2010, **132**, 1754.
312 G. Wu, K. L. More, C. M. Johnston and P. Zelenay, *Science*, 2011, **332**, 433.
313 Y. Zhao, K. Watanabe and K. Hashimoto, *J. Am. Chem. Soc.*, 2012, **134**, 19528.
314 J. Wu, H. W. Park, A. P. Yu, D. Higgins and Z. W. Chen, *J. Phys. Chem. C*, 2012, **116**, 9427.
315 J. S. Lee, G. S. Park, S. T. Kim, M. L. Liu and J. Cho, *Angew. Chem., Int. Ed.*, 2013, **52**, 1026.
316 S. W. Yuan, J. L. Shui, L. Grabstanowicz, C. Chen, S. Commet, B. Reprogle, T. Xu, L. P. Yu and D. J. Liu, *Angew. Chem., Int. Ed.*, 2013, **52**, 8349.
317 L. Wang, J. Yin, L. Zhao, C. G. Tian, P. Yu, J. Q. Wang and H. G. Fu, *Chem. Commun.*, 2013, **49**, 3022.
318 J. K. Dombrovskis, H. Y. Jeong, K. Fossum, O. Terasaki and A. E. C. Palmqvist, *Chem. Mater.*, 2013, **25**, 856.
319 E. Proietti, F. Jaouen, M. Lefevre, N. Larouche, J. Tian, J. Herranz and J. P. Dodelet, *Nat. Commun.*, 2011, **2**, 416.
320 D. Zhao, J. L. Shui, C. Chen, X. Q. Chen, B. M. Reprogle, D. P. Wang and D. J. Liu, *Chem. Sci.*, 2012, **3**, 3200.
321 P. P. Su, H. Xiao, J. Zhao, Y. Yao, Z. G. Shao, C. Li and Q. H. Yang, *Chem. Sci.*, 2013, **4**, 2941.
322 J. Tian, A. Morozan, M. T. Sougrati, M. Lefevre, R. Chenitz, J. P. Dodelet, D. Jones and F. Jaouen, *Angew. Chem., Int. Ed.*, 2013, **52**, 6867.
323 A. L. Bouwkamp-Wijnoltz, W. Visscher, J. A. R. van Veen, E. Boellaard, A. M. van der Kraan and S. C. Tang, *J. Phys. Chem. B*, 2002, **106**, 12993.
324 Y. Nabae, S. Moriya, K. Matsubayashi, S. M. Lyth, M. Malon, L. B. Wu, N. M. Islam, Y. Koshigoe, S. Kuroki, M. A. Kakimoto, S. Miyata and J. Ozaki, *Carbon*, 2010, **48**, 2613.
325 W. M. Li, J. Wu, D. C. Higgins, J. Y. Choi and Z. W. Chen, *ACS Catal.*, 2012, **2**, 2761.
326 W. Gao, J. E. Mueller, Q. Jiang and T. Jacob, *Angew. Chem., Int. Ed.*, 2012, **51**, 9448.
327 S. S. Zhang, X. M. Ren and J. Read, *Electrochim. Acta*, 2011, **56**, 4544.
328 X. M. Ren, S. S. Zhang, D. T. Tran and J. Read, *J. Mater. Chem.*, 2011, **21**, 10118.
329 J. L. Shui, N. K. Karan, M. Balasubramanian, S. Y. Li and D. J. Liu, *J. Am. Chem. Soc.*, 2012, **134**, 16654.
330 G. Wu, N. H. Mack, W. Gao, S. G. Ma, R. Q. Zhong, J. T. Han, J. K. Baldwin and P. Zelenay, *ACS Nano*, 2012, **6**, 9764.
331 F. Mazza and S. Trassatti, *J. Electrochem. Soc.*, 1963, **110**, 847.
332 H. X. Zhong, H. M. Zhang, G. Liu, Y. M. Liang, J. W. Hu and B. L. Yi, *Electrochem. Commun.*, 2006, **8**, 707.
333 A. Takagaki, Y. Takahashi, F. X. Yin, K. Takanabe, J. Kubota and K. Domen, *J. Electrochem. Soc.*, 2009, **156**, B811.
334 F. X. Yin, K. Takanabe, J. Kubota and K. Domen, *J. Electrochem. Soc.*, 2010, **157**, B240.
335 T. Ando, S. Izhar, H. Tominaga and M. Nagai, *Electrochim. Acta*, 2010, **55**, 2614.
336 J. Qi, L. H. Jiang, Q. Jiang, S. L. Wang and G. Q. Sun, *J. Phys. Chem. C*, 2010, **114**, 18159.
337 H. B. Wu and W. Chen, *J. Am. Chem. Soc.*, 2011, **133**, 15236.
338 J. Chen, K. Takanabe, R. Ohnishi, D. L. Lu, S. Okada, H. Hatasawa, H. Morioka, M. Antonietti, J. Kubotaa and K. Domen, *Chem. Commun.*, 2010, **46**, 7492.
339 P. He, Y. G. Wang and H. S. Zhou, *Chem. Commun.*, 2011, **47**, 10701.
340 Y. R. Wang, R. Ohnishi, E. Yoo, P. He, J. Kubota, K. Domen and H. S. Zhou, *J. Mater. Chem.*, 2012, **22**, 15549.
341 F. J. Li, R. Ohnishi, Y. Yamada, J. Kubota, K. Domen, A. Yamada and H. S. Zhou, *Chem. Commun.*, 2013, **49**, 1175.
342 S. M. Dong, X. Chen, K. J. Zhang, L. Gu, L. X. Zhang, X. H. Zhou, L. F. Li, Z. H. Liu, P. X. Han, H. X. Xu, J. H. Yao, C. J. Zhang, X. Y. Zhang, C. Q. Shang, G. L. Cui and L. Q. Chen, *Chem. Commun.*, 2011, **47**, 11291.
343 K. J. Zhang, L. X. Zhang, X. Chen, X. He, X. G. Wang, S. M. Dong, L. Gu, Z. H. Liu, C. S. Huang and G. L. Cui, *ACS Appl. Mater. Interfaces*, 2013, **5**, 3677.
344 K. J. Zhang, L. X. Zhang, X. Chen, X. He, X. G. Wang, S. M. Dong, P. X. Han, C. J. Zhang, S. Wang, L. Gu and G. L. Cui, *J. Phys. Chem. C*, 2013, **117**, 858.

345 M. Yuasa, A. Yamaguchi, H. Itsuki, K. Tanaka, M. Yamamoto and K. Oyaizu, *Chem. Mater.*, 2005, **17**, 4278.
346 V. G. Khomenko, V. Z. Barsukov and A. S. Katashinskii, *Electrochim. Acta*, 2005, **50**, 1675.
347 R. Bashyam and P. Zelenay, *Nature*, 2006, **443**, 63.
348 A. L. M. Reddy, N. Rajalakshmi and S. Ramaprabhu, *Carbon*, 2008, **46**, 2.
349 W. M. Zhang, J. Chen, P. Wagner, G. F. Swiegers and G. G. Wallace, *Electrochem. Commun.*, 2008, **10**, 519.
350 Q. Zhou, C. M. Li, J. Li and J. Lu, *J. Phys. Chem. C*, 2008, **112**, 18578.
351 B. Winther-Jensen, O. Winther-Jensen, M. Forsyth and D. R. MacFarlane, *Science*, 2008, **321**, 671.
352 K. Lee, L. Zhang, H. Lui, R. Hui, Z. Shi and J. J. Zhang, *Electrochim. Acta*, 2009, **54**, 4704.
353 R. Sulub, W. Martínez-Millán and M. A. Smit, *Int. J. Electrochem. Sci.*, 2009, **4**, 1015.
354 W. M. Millan, T. T. Thompson, L. G. Arriaga and M. A. Smit, *Int. J. Hydrogen Energy*, 2009, **34**, 694.
355 W. M. Millan and M. A. Smit, *J. Appl. Polym. Sci.*, 2009, **112**, 2959.
356 S. Y. Wang, D. S. Yu, L. M. Dai, D. W. Chang and J. B. Baek, *ACS Nano*, 2011, **5**, 6202.
357 Y. Zhao, K. Watanabe and K. Hashimoto, *J. Mater. Chem.*, 2012, **22**, 12263.
358 Y. M. Cui, Z. Y. Wen, X. Liang, Y. Lu, J. Jin, M. F. Wu and X. W. Wu, *Energy Environ. Sci.*, 2012, **5**, 7893.
359 Q. Lu, Q. Zhao, H. M. Zhang, J. Li, X. H. Wang and F. S. Wang, *ACS Macro Lett.*, 2013, **2**, 92.
360 Y. H. Bing, H. S. Liu, L. Zhang, D. Ghosh and J. J. Zhang, *Chem. Soc. Rev.*, 2010, **39**, 2184.
361 Z. Y. Zhou, N. Tian, J. T. Li, I. Broadwell and S. G. Sun, *Chem. Soc. Rev.*, 2011, **40**, 4167.
362 N. Tian, Z. Y. Zhou, S. G. Sun, Y. Ding and Z. L. Wang, *Science*, 2007, **316**, 732.
363 S. Guo, S. Zhang and S. Sun, *Angew. Chem., Int. Ed.*, 2013, **52**, 8526, DOI: 10.1002/anie.201207186.
364 C. L. Tang, X. Huang and H. Zhang, *Mater. Today*, 2013, **16**, 29.
365 J. Zhang, K. Sasaki, E. Sutter and R. R. Adzic, *Science*, 2007, **315**, 220.
366 Q. S. Chen, Z. Y. Zhou, F. J. Vidal-Iglesias, J. Solla-Gullon, J. M. Feliu and S. G. Sun, *J. Am. Chem. Soc.*, 2011, **133**, 12930.
367 B. Y. Xia, W. T. Ng, H. B. Wu, X. Wang and X. W. Lou, *Angew. Chem., Int. Ed.*, 2012, **51**, 7213.
368 J. He, P. Zhang, J. L. Gong and Z. H. Nie, *Chem. Commun.*, 2012, **48**, 7344.
369 J. He, Z. J. Wei, L. Wang, Z. Tomova, T. Babu, C. Y. Wang, X. J. Han, J. T. Fourkas and Z. H. Nie, *Angew. Chem., Int. Ed.*, 2013, **52**, 2463.
370 X. Huang, Z. Y. Zeng, S. Y. Bao, M. F. Wang, X. Y. Qi, Z. X. Fan and H. Zhang, *Nat. Commun.*, 2013, **4**, 1444.
371 V. R. Stamenkovic, B. Fowler, B. S. Mun, G. F. Wang, P. N. Ross, C. A. Lucas and N. M. Markovic, *Science*, 2007, **315**, 493.
372 B. Lim, M. J. Jiang, P. H. C. Camargo, E. C. Cho, J. Tao, X. M. Lu, Y. M. Zhu and Y. M. Xia, *Science*, 2009, **324**, 1302.
373 J. Kim, Y. Lee and S. Sun, *J. Am. Chem. Soc.*, 2010, **132**, 4996.
374 P. P. Fang, S. Duan, X. D. Lin, J. R. Anema, J. F. Li, O. Buriez, Y. Ding, F. R. Fan, D. Y. Wu, B. Ren, Z. L. Wang, C. Amatore and Z. Q. Tian, *Chem. Sci.*, 2011, **2**, 531.
375 S. Guo and S. Sun, *J. Am. Chem. Soc.*, 2012, **134**, 2492.
376 S. Zhang, S. Guo, H. Zhu, D. Su and S. Sun, *J. Am. Chem. Soc.*, 2012, **134**, 5060.
377 S. Hasegawa, N. Imanishi, T. Zhang, J. Xie, A. Hirano, Y. Takeda and O. Yamamoto, *J. Power Sources*, 2009, **189**, 371.
378 T. Zhang, N. Imanishi, Y. Shimonishi, A. Hirano, Y. Takeda, O. Yamamoto and N. Sammes, *Chem. Commun.*, 2010, **46**, 1661.
379 H. Liu and Y. C. Xing, *Electrochem. Commun.*, 2011, **13**, 646.
380 M. H. Shao, T. Yu, J. H. Odell, M. S. Jin and Y. N. Xia, *Chem. Commun.*, 2011, **47**, 6566.
381 B. B. Blizanac, P. N. Ross and N. M. Markovic, *Electrochim. Acta*, 2007, **52**, 2264.
382 F. H. B. Lima, C. D. Sanches and E. A. Ticianelli, *J. Electrochem. Soc.*, 2005, **152**, A1466.
383 L. Demarconnay, C. Coutanceau and J. M. Leger, *Electrochim. Acta*, 2004, **49**, 4513.
384 J. R. Varcoe, R. C. T. Slade, G. L. Wright and Y. L. Chen, *J. Phys. Chem. B*, 2006, **110**, 21041.
385 J. S. Guo, A. Hsu, D. Chu and R. G. Chen, *J. Phys. Chem. C*, 2010, **114**, 4324.
386 Y. C. Lu, D. G. Kwabi, K. P. C. Yao, J. R. Harding, J. G. Zhou, L. Zuin and Y. Shao-Horn, *Energy Environ. Sci.*, 2011, **4**, 2999.
387 Y. C. Lu, Z. C. Xu, H. A. Gasteiger, S. Chen, K. Hamad-Schifferli and Y. Shao-Horn, *J. Am. Chem. Soc.*, 2010, **132**, 12170.
388 Y. C. Lu, H. A. Gasteiger and Y. Shao-Horn, *J. Am. Chem. Soc.*, 2011, **133**, 19048.
389 Z. Q. Peng, S. A. Freunberger, Y. H. Chen and P. G. Bruce, *Science*, 2012, **337**, 563.
390 H. G. Jung, Y. S. Jeong, J. B. Park, Y. K. Sun, B. Scrosati and Y. J. Lee, *ACS Nano*, 2013, **7**, 3532.
391 X. Huang, Z. Y. Zeng and H. Zhang, *Chem. Soc. Rev.*, 2013, **42**, 1934.
392 Y. P. Du, Z. Y. Yin, J. X. Zhu, X. Huang, X. J. Wu, Z. Y. Zeng, Q. Y. Yan and H. Zhang, *Nat. Commun.*, 2012, **3**, 1177.
393 L. Zhao, Y. S. Hu, H. Li, Z. X. Wang and L. Q. Chen, *Adv. Mater.*, 2011, **23**, 1385.
394 X. Lu, L. Zhao, X. Q. He, R. J. Xiao, L. Gu, Y. S. Hu, H. Li, Z. X. Wang, X. F. Duan, L. Q. Chen, J. Maier and Y. Ikuhara, *Adv. Mater.*, 2012, **24**, 3233.
395 H. Jung, J. Hassoun, J. Park, Y. Sun and B. Scrosati, *Nat. Chem.*, 2012, **4**, 579.
396 Y. H. Chen, S. A. Freunberger, Z. Q. Peng, F. Bardé and P. G. Bruce, *J. Am. Chem. Soc.*, 2012, **134**, 7952.
397 T. Zhang and H. S. Zhou, *Nat. Commun.*, 2013, **4**, 1817.
398 L. M. Suo, Y. S. Hu, H. Li, M. Armand and L. Q. Chen, *Nat. Commun.*, 2013, **4**, 1481.

399 F. Li, T. Zhang, Y. Yamada, A. Yamada and H. Zhou, *Adv. Energy Mater.*, 2013, **3**, 532.
400 W. Xu, J. Hu, M. H. Engelhard, S. A. Towne, J. S. Hardy, J. Xiao, J. Feng, M. Y. Hu, J. Zhang, F. Ding, M. E. Gross and J. G. Zhang, *J. Power Sources*, 2012, **215**, 240.
401 B. M. Gallant, R. R. Mitchell, D. G. Kwabi, J. Zhou, L. Zuin, C. V. Thompson and Y. Shao-Horn, *J. Phys. Chem. C*, 2012, **116**, 20800.
402 M. M. O. Thotiyl, S. A. Freunberger, Z. Q. Peng and P. G. Bruce, *J. Am. Chem. Soc.*, 2013, **135**, 494.
403 D. Aurbach, E. Zinigrad, Y. Cohen and H. Teller, *Solid State Ionics*, 2002, **148**, 405.
404 J. Yamaki, S. Tobishima, K. Hayashi, K. Saito, Y. Nemoto and M. Arakawa, *J. Power Sources*, 1998, **74**, 219.
405 D. Aurbach, I. Weissman, A. Zaban and O. Chusid, *Electrochim. Acta*, 1994, **39**, 51.
406 W. Walker, V. Giordani, J. Uddin, V. S. Bryantsev, G. V. Chase and D. Addison, *J. Am. Chem. Soc.*, 2013, **135**, 2076.
407 J. Hassoun, H. G. Jung, D. J. Lee, J. B. Park, K. Amine, Y. K. Sun and B. Scrosati, *Nano Lett.*, 2012, **12**, 5775.
408 Z. L. Wang, D. Xu, H. G. Wang, Z. Wu and X. B. Zhang, *ACS Nano*, 2013, **7**, 2422.
409 J. J. Xu, Z. L. Wang, D. Xu, L. L. Zhang and X. B. Zhang, *Nat. Commun.*, 2013, **4**, 2438.
410 J. T. Li, Z. Y. Zhou, I. Broadwell and S. G. Sun, *Acc. Chem. Res.*, 2012, **45**, 485.
411 Z. Liu, S. Y. Ding, Z. B. Chen, X. Wang, J. H. Tian, J. R. Anema, X. S. Zhou, D. Y. Wu, B. W. Mao, X. Xu, B. Ren and Z. Q. Tian, *Nat. Commun.*, 2011, **2**, 305.
412 S. Duan, X. Xu, Y. Luo and Z. Q. Tian, *Chem. Commun.*, 2011, **47**, 11438.
413 Y. F. Huang, H. P. Zhu, G. K. Liu, D. Y. Wu, B. Ren and Z. Q. Tian, *J. Am. Chem. Soc.*, 2010, **132**, 9244.
414 H. Lim, E. Yilmaz and H. R. Byon, *J. Phys. Chem. Lett.*, 2012, **3**, 3210.
415 Y. C. Lu, E. J. Crumlin, G. M. Veith, J. R. Harding, E. Mutoro, L. Baggetto, N. J. Dudney, Z. Liu and Y. Shao-Horn, *Sci. Rep.*, 2012, **2**, 715.
416 L. Zhong, R. R. Mitchell, Y. Liu, B. M. Gallant, C. V. Thompson, J. Y. Huang, S. X. Mao and Y. Shao-Horn, *Nano Lett.*, 2013, **13**, 2209.

